

# Variational Quantitative Phase-field Modeling and Simulation of Non-isothermal Sintering Process

Zur Erlangung des akademischen Grades Doktor-Ingenieur (Dr.-Ing.)  
Genehmigte Dissertation im Fachbereich Material- und Geowissenschaften von Timileyin  
David Oyedeji aus Ibadan, Nigeria  
Tag der Einreichung: 14.05.2024, Tag der Prüfung: 11.07.2024

1. Gutachten: Prof. Bai-Xiang Xu  
2. Gutachten: Prof. Herbert Egger  
Darmstadt, Technische Universität Darmstadt



TECHNISCHE  
UNIVERSITÄT  
DARMSTADT

MECHANICS of  
FUNCTIONAL  
MATERIALS



Materials and Earth Sciences  
Department

Mechanics of Functional  
Materials

Variational Quantitative Phase-field Modeling and Simulation of Non-isothermal Sintering Process

Accepted doctoral thesis in the department of Materials and Earth Sciences  
by Timileyin David Oyedeji

Date of submission: 14.05.2024

Date of thesis defense: 11.07.2024

Darmstadt, Technische Universität Darmstadt

Bitte zitieren Sie dieses Dokument als:

URN: urn:nbn:de:tuda-tuprints-281703

URL: <https://tuprints.ulb.tu-darmstadt.de/28170>

Jahr der Veröffentlichung auf TUprints: 2024

Dieses Dokument wird bereitgestellt von tuprints,  
E-Publishing-Service der TU Darmstadt  
<https://tuprints.ulb.tu-darmstadt.de>  
[tuprints@ulb.tu-darmstadt.de](mailto:tuprints@ulb.tu-darmstadt.de)

Die Veröffentlichung steht unter folgender Creative Commons Lizenz:

Namensnennung 4.0 International

<https://creativecommons.org/licenses/by/4.0/>

This work is licensed under a Creative Commons License:

Attribution 4.0 International

<https://creativecommons.org/licenses/by/4.0/>

"There is no better teacher than adversity. Every defeat, every heartbreak, every loss, contains its own seed, its own lesson on how to improve your performance the next time" - Malcolm X.



---

## Erklärungen laut Promotionsordnung

### § 8 Abs. 1 lit. d PromO

Ich versichere hiermit, dass zu einem vorherigen Zeitpunkt noch keine Promotion versucht wurde. In diesem Fall sind nähere Angaben über Zeitpunkt, Hochschule, Dissertationsthema und Ergebnis dieses Versuchs mitzuteilen.

### § 9 Abs. 1 PromO

Ich versichere hiermit, dass die vorliegende Dissertation – abgesehen von den in ihr ausdrücklich genannten Hilfen – selbstständig verfasst wurde und dass die „Grundsätze zur Sicherung guter wissenschaftlicher Praxis an der Technischen Universität Darmstadt“ und die „Leitlinien zum Umgang mit digitalen Forschungsdaten an der TU Darmstadt“ in den jeweils aktuellen Versionen bei der Verfassung der Dissertation beachtet wurden.

### § 9 Abs. 2 PromO

Die Arbeit hat bisher noch nicht zu Prüfungszwecken gedient.

Darmstadt, 14.05.2024

---

Timileyin David Oyedeki

---



---

# Acknowledgements

---

This dissertation would not have been possible without the invaluable support and guidance I received throughout my doctoral journey. As a Yoruba proverb says, "*Ọpẹ olóore, àdádátán ni*", which translates to "*One can never thank enough those who do one good.*" With this in mind, I would first and foremost like to express my deepest gratitude to Prof. Bai-Xiang Xu for granting me the incredible opportunity to pursue research within her group. I am eternally grateful for her continual trust, insightful guidance, inspiring discussions, and constructive feedback that have greatly impacted my personal and professional development.

I would also like to express my sincere gratitude to Prof. Hebbert Egger and Dr. Aaron Brunk for their intense and continual insightful discussions throughout my doctoral study. Their deep expertise and willingness to share their knowledge have significantly broadened my understanding of various research topics.

I would like to thank Prof. Karsten Durst and Prof. Karsten Albe for their willingness to serve as referees for this dissertation. Their time and efforts in reviewing and evaluating this work are highly appreciated.

This research was made possible by financial support from the Deutsche Forschungsgemeinschaft (DFG), which I am grateful for. I would also like to acknowledge the NHR4CES Resource Allocation Board for granting valuable computing time, which facilitated my research. Additionally, I would like to appreciate the access to the Lichtenberg High-Performance Computer (HPC) and the technical support from the HHLR, TU Darmstadt.

A special thanks goes to my colleague and friend, Dr. Yangyiwei Yang. His dedicated support, both scientific and technical, has been unparalleled throughout my academic journey at TU Darmstadt. I am incredibly grateful for his constant encouragement and willingness to help whenever needed. I also want to convey my sincere appreciation to Somnath Bharech and Patrick Kühn for their support and helpful discussions during both the research and writing phases of this thesis. I am sincerely grateful guys.

---

I would like to express my appreciation to Mrs. Maren Arnold for various administrative support, assistance, and guidance. I would also like to acknowledge the entire Mechanics of Functional Materials Group, both current and former members, for upholding an exciting research atmosphere. A special thanks go to Prof. Min Yi, Dr. Yang Bai, Dr. Peter Stein, Dr. Dominik Ohmer, Dr. Xiandong Zhou, Dr. Christoph Reimuth, Dr. Yao Liu, Dr. Kai Wang, Dr. Xiang-Long Peng, Dr. Shahed Rezaei, Hui, Unai, Abdullah, Sebastian, Xiangfeng, Mozhdah, Tiansheng, Wanxin, Jiajun, Nick, Jean, Bondi, Sri, Eren, Clement.

At this point, I would like to express my sincere gratitude to everyone who has played a role in my academic journey. I am particularly grateful to Prof. Ismaila Idowu Ahmed, Engr. Taiwo Yahaya, Prof. Jamiu Kolawole Odusote, and Prof. Olaoluwa Senayon.

My deepest gratitude extends to my friends, both near and far, who have supported me in countless ways. I appreciate Tunde, Tomiwa, Jide, Kunle, Biola and his family (Laura and Jade). Thank you very much guys for your support and the wonderful times that we have shared. I would also like to express my sincere appreciation to Pastor Kelvin Omoruyi and the entire Christ Embassy Darmstadt church. Your faith and sense of community have been a great source of strength.

This doctoral journey wouldn't have been possible without the continual support of some exceptional people in my life. To my parents, Michael Kayode Oyedeji and Eunice Oredola Oyedeji, my deepest gratitude goes for your endless love, prayers, and encouragement. Everything I have achieved is a testament to the foundation you built for me. I also extend my heartfelt thanks to my siblings, Tolu, Tope, and Tomi, for their constant support throughout this journey.

The greatest thanks must go to the sweetest part of my life, my wife, Tayo Opeyemi Abolarin. Your patience, support, and understanding throughout my doctoral work have been nothing short of extraordinary. You have been my biggest cheerleader. I could not have done this without you. And to my precious daughter, Oluwatamilore Joanna, your constant coos and babbles have been a source of unending joy and a reminder of what truly matters.

Finally, I offer my deepest gratitude to God for granting me the strength, knowledge, and perseverance to complete this research and write this thesis. Without His blessings and mercies, none of this would have been possible.



---

## Abstract

---

Sintering, an important technique in the production of ceramics and metals has seen the emergence of novel methods (e.g., selective laser sintering) offering higher heating rates and flexibility in creating complex-shape components. However, achieving the desired material properties and underlying microstructure using these techniques is challenging due to the interplay of several mechanisms and complex non-isothermal factors. Phase-field modeling, a powerful tool in investigating microstructure evolution in sintering, has quantitative validity limitations when coupled with diffusive processes (e.g., mass and heat transfer). As one of the diffuse-interface approaches, abnormal interface effects may originate at the interfaces during simulations. On the other hand, models formulated to be quantitative, do not necessarily exhibit a thermodynamics variational nature. While variational quantitative models exist for liquid-solid interfaces, similar models are absent for sintering interfaces.

This study introduces a variational quantitative phase-field model formulated for the non-isothermal sintering process. The model, developed based on Onsager relations and variational principles is formulated to eliminate abnormal interface effects while ensuring thermodynamic consistency. Cross-coupling terms between the conserved kinetics (i.e., mass and thermal transfer) and the non-conserved one (grain growth), which are typically neglected in conventional models, are considered. These terms are shown via asymptotic analysis to be instrumental in ensuring the elimination of interface effects. In addition, it was obtained that the cross-coupling terms do not modify the thermodynamic equilibrium conditions. Furthermore, anisotropic interpolation of the kinetic mobilities is employed to ensure the model's quantitative validity.

Numerical simulations validate the importance of cross-coupling terms and anisotropic interpolation for accurate quantitative simulations. While the proposed model introduces these terms, necessitating a more complex numerical implementation, it offers a significant advantage. The model allows the usage of larger interface widths during simulations while maintaining quantitative accuracy. This enables the use of coarser meshes, leading to a better improvement in computational efficiency. Thermal-microstructural

---

evolution results are also presented and compared between proposed and existing models. Furthermore, 3D simulations of yttria-stabilized zirconia micro-particles sintering demonstrate the model's ability to capture microstructure, density, and temperature profile evolution. The proposed modeling and simulation framework in this study provides a powerful tool for quantitative simulations of non-isothermal sintering and related processes.

---

# Zusammenfassung

---

Im Bereich des Sinterns, eines bedeutenden Technik bei der Produktion von Keramik und Metallen wurde Zeuge vom Erscheinen neuartiger Technologien (z.B. Selektives Lastersintern), welche höhere Heizraten und Flexibilität in der Produktion komplexer Geometrien bietet. Allerdings ist das Erreichen der angestrebten Mikrostruktur und Materialeigenschaften eine Herausforderung an sich, dem liegt ein Zwischenspiel verschiedener Mechanismen und komplexer nicht-isothermer Faktoren zugrunde. Das Phasenfeldmodell, ein leistungstarkes Mittel zur Untersuchung der Evolution der Mikrostruktur, weist quantitative Gültigkeitsbeschränkungen auf, wenn sie mit diffusiven Prozessen (z.B. Massen- und Wärmetransport) gekoppelt wird. Da es sich um einen diffusiven-Grenzflächen Ansatz handelt, können während der Simulation selber abnormale Effkte von ebendiesen Grenzflächen ausgehen. Andererseits mangelt konventionellen quantitativen Modellen die zugrundeliegende Thermodynamik und Variationsrechnung. Zwar existieren quantitative Modelle basierend auf der Variationsrechnung für flüssig-fest Grenzflächen, im Bereich des Sinterns sind diese aber derzeit nicht verfügbar.

In dieser Arbeit wird ein variatives quantitatives Phasenfeldmodell (unsure about the translation of variational model) für nicht-isotherme Sinterprozesse formuliert. Das entwickelte Modell, basierend auf den Onsager Beziehungen und Prinzipien der Variationsrechnung, wurde formuliert um abnormale Grenzflächeneffekte zu eliminieren und gleichzeitig thermodynamische Konsistenz zu wahren. Die Kopplungsterme zwischen der Kinetik konservierter Grössen (z.B. Masse- und Wärmetransfer) und der Kinetik der nicht-konservierten Grösse (Kornwachstum), welche typischerweise vernachlässigt werden, werden hier mit einbezogen. Via asymptotischer Analyse wird gezeigt, wie instrumentell diese Terme sind um die Eliminierung von Grenzflächeneffekten sicherzustellen und gleichzeitig eine Änderung der Gleichgewichtsbedingungen zu verhindern. Weitergehend wird eine quantitative Validierung des Modells mittels anisotroper Interpolation der kinetischen Mobilitäten durchgeführt.

Numerische Simulationen belegen die Bedeutung der Kopplungsterme und anisotropischer Interpolation für quantitativ akkurate Simulationen. Während das vorgeschla-

---

gene Modell diese Begriffe einführt, was eine komplexere numerische Implementierung erfordert, bietet es einen erheblichen Vorteil. Das Modell ermöglicht die Verwendung grösserer Schnittstellenbreiten während der Simulationen bei gleichzeitiger Beibehaltung der quantitativen Genauigkeit. Dies ermöglicht die Verwendung gröberer Netze, was zu einer besseren Verbesserung der Recheneffizienz führt. Die Evolution der Mikrostruktur aufgrund thermischer Einflüsse dargestellt und ein Vergleich erfolgt zwischen etablierten und dem vorgestelltem Modell. Ausserdem wurden 3D Simulationen des Sinterns von YSZ Mikropartikeln durchgeführt, diese zeigen die Möglichkeiten des formulierten Modells die Entwicklung der Mikrostruktur, Dichte und des Temperaturprofils darzustellen. Das formulierte Modell und Simulation-Frameworks dieser Studie bietet ein leistungsstarkes Werkzeug für quantitative Simulationen für nicht-isothermes Sintern und verwandte Prozesse.

---

# Contents

---

<b>Acknowledgements</b>	<b>I</b>
<b>Abstract</b>	<b>III</b>
<b>List of Symbols</b>	<b>XI</b>
<b>1 Introduction</b>	<b>1</b>
1.1 Motivation . . . . .	1
1.2 Objectives and Outline . . . . .	6
<b>2 Sintering Mechanisms of Polycrystalline Materials</b>	<b>9</b>
2.1 Concepts of Sintering . . . . .	9
2.1.1 Categories of sintering . . . . .	10
2.1.2 Sintering mechanisms . . . . .	13
2.2 Geometric Models of Sintering . . . . .	18
2.2.1 Initial stage sintering . . . . .	19
2.2.2 Intermediate stage sintering . . . . .	22
2.2.3 Final stage sintering . . . . .	25
2.3 Unconventional Sintering . . . . .	26
2.3.1 Selective laser sintering . . . . .	27
2.3.2 Spark plasma sintering . . . . .	27
2.3.3 Flash sintering . . . . .	28
2.3.4 Microwave sintering . . . . .	28
<b>3 Fundamentals of Phase-field Modeling and Simulation</b>	<b>29</b>
3.1 Phase-field Theory . . . . .	29
3.1.1 Basic concept of phase-field . . . . .	30
3.1.2 Variational formulations . . . . .	32
3.1.3 Sharp and thin interface limits . . . . .	34
3.1.4 Interface-dependent effects . . . . .	37



3.1.5	Quantitative phase-field models . . . . .	41
3.2	Phase-field Simulation of Sintering . . . . .	44
3.2.1	Conventional model . . . . .	44
3.2.2	Grand-potential model . . . . .	45
3.2.3	Entropy-based non-isothermal model . . . . .	46
3.3	Finite-element Basics . . . . .	48
<b>4</b>	<b>Variational Quantitative Phase-field Model of Non-isothermal Sintering: Model Development and Asymptotic Analysis</b>	<b>53</b>
4.1	Model Formulations . . . . .	55
4.1.1	Entropy and free energy functionals . . . . .	55
4.1.2	Kinetic equations . . . . .	57
4.2	Thin-interface Asymptotics . . . . .	60
4.2.1	Sharp-interface description of non-isothermal sintering . . . . .	60
4.2.2	Thin-interface limit of model . . . . .	62
4.2.3	Anisotropic interpolations and eliminating potential jumps . . . . .	66
4.3	Analysis of Order Parameter Deviation . . . . .	71
4.3.1	General considerations . . . . .	72
4.3.2	Theoretical analysis . . . . .	73
<b>5</b>	<b>Variational Quantitative Phase-field Model of Non-isothermal Sintering: Numerical Implementation and Verification</b>	<b>77</b>
5.1	Finite-element Implementation . . . . .	77
5.2	Model Verification For an Elliptical Inclusion . . . . .	81
5.2.1	Mass antitrapping current . . . . .	82
5.2.2	Thermal antitrapping current . . . . .	83
5.3	Comparison With Existing Model . . . . .	84
5.3.1	Thermo-microstructural comparison . . . . .	85
5.3.2	Kinetics of the sintering neck and dihedral angle . . . . .	88
5.4	Importance of Anisotropic Interpolations . . . . .	90
5.4.1	Thermal conductivity interpolation . . . . .	90
5.4.2	Mass diffusivity interpolation . . . . .	94
5.5	Numerical Analysis of Order Parameter Deviation . . . . .	95
5.5.1	Planar and Circular Interfaces . . . . .	95
5.5.2	Elliptical Interface . . . . .	98
<b>6</b>	<b>Variational Quantitative Phase-field Simulations of Non-conventional Sintering</b>	<b>101</b>
6.1	General Simulation Set-up . . . . .	101



6.2 Isothermal Simulations . . . . .	103
6.2.1 Transient microstructure . . . . .	104
6.2.2 Segment-wise density distribution . . . . .	106
6.3 Non-isothermal Simulations . . . . .	109
6.3.1 Transient temperature profiles . . . . .	109
6.3.2 Segment-wise temperature distribution . . . . .	110
<b>7 Conclusion and Outlook</b>	<b>113</b>
7.1 Conclusion . . . . .	113
7.2 Outlook . . . . .	116
<b>Bibliography</b>	<b>117</b>
<b>List of Figures</b>	<b>127</b>
<b>List of Tables</b>	<b>133</b>
<b>Abbreviations</b>	<b>135</b>
<b>Curriculum Vitae</b>	<b>137</b>
<b>List of Publications</b>	<b>139</b>





---

## List of Symbols

---

Symbol	Description	Unit/Value
$S$	Entropy functional	$\text{JK}^{-1}$
$F$	Free energy functional	J
$e$	Internal energy density	$\text{Jm}^{-3}$
$s$	Entropy density	$\text{Jm}^{-3}\text{K}^{-1}$
$f$	Free energy density	$\text{Jm}^{-3}$
$\mu$	Chemical potential	J
$\sigma$	Entropy production	$\text{Jm}^{-3}\text{K}^{-1}$
$\rho$	Conserved order parameter representing solid/atmosphere regions	-
$\eta_i$	Non-conserved order parameters representing grain orientations	-
$h$	Interpolation function	-
$\kappa$	Diffusive interface gradient energy coefficients, e.g., $\kappa_\rho$ for solid-atmosphere interface, and $\kappa_\eta$ for grain boundary	$\text{Jm}^{-1}\text{K}^{-1}$
$\underline{C}, \underline{D}$	Free energy barrier heights parameters	$\text{Jm}^{-3}$
$c, c_r$	Volumetric specific heat	$\text{Jm}^{-3}\text{K}^{-1}$
$l$	Diffusive interface width	m

---

---

Symbol	Description	Unit/Value
$v$	Diffusive interface velocity	$\text{ms}^{-1}$
$L, \mathbf{L}$	Onsager kinetic parameter, and its tensorial form	-
$D$	Diffusivity	$\text{m}^2\text{s}^{-1}$
$k$	Thermal conductivity	$\text{Js}^{-1}\text{m}^{-1}\text{K}^{-1}$
$G_{\text{gb}}^{\text{eff}}$	Grain boundary mobility	$\text{m}^4\text{J}^{-1}\text{s}^{-1}$
$M_1, M_2$	Cross-coupling functions	-
$\mathbf{n}_{\text{sf}}$	Unit vector normal to the free surface	-
$\mathbf{N}, \mathbf{T}$	Normal and projection tensors	-
$\mathbf{J}_{\rho}$	Mass transfer flux	$\text{ms}^{-1}$
$\mathbf{J}_e$	Energy flux	$\text{Jm}^2\text{s}^{-1}$
$R_s$	Thermal resistance	$\text{KsJ}^{-1}$
$\delta\mu$	Chemical potential jump	$\text{Jm}^{-3}$
$\delta T$	Temperature jump	$\text{K}$
$\lambda$	Sintering neck	$\text{m}$
$\Phi$	Dihedral angle	$^{\circ}$
$\delta\rho$	Deviation of bulk values of $\rho$	-
$\mathcal{A}, \mathcal{B}, \mathcal{C}$	Kinetic coefficients for Onsager matrix (sharp interface)	-
$\gamma$	Interface energies	$\text{Jm}^{-2}$
$\Omega$	Simulation domain	$\text{m}^2$ or $\text{m}^3$
$\Gamma$	Boundary of simulation domain	$\text{m}$ or $\text{m}^2$

---



---

Symbol	Description	Unit/Value
$\mathcal{R}$	Ideal gas constant	$8.314 \text{ JK}^{-1} \text{ mol}^{-1}$
$\pi$	Pi	3.142
$V_m$	Molar Volume	$\text{m}^3 \text{ mol}^{-1}$
$T$	Temperature	K
$t$	Time	s
$\frac{\delta(\cdot)}{\delta x}$	Variational derivative on a function $x$	-
$\frac{d(\cdot)}{dx}$	Total derivative on a variable $x$	-
$\frac{\partial(\cdot)}{\partial x}$	Partial derivative on a variable $x$	-
$\nabla(\cdot)$	Gradient operator	-
$\nabla \cdot (\cdot)$	Divergence operator	-
$\nabla^2(\cdot)$	Laplace operator	-
$\otimes$	Dyadic product	-

---



---

# 1 Introduction

---

## 1.1 Motivation

Sintering is a widely used manufacturing technique and a key industrial process in science and technology [1, 2]. In its simplest form, it involves the compaction of a mass of powder particles into a dense structure [3, 4]. Thereby a solid structure with reduced surface area and enhanced density is created from a set of fine particles (illustrated in Fig. 1.1). Conventional sintering methods typically compact powder particles via the direct application of heat and pressure at a temperature relatively lower than the melting point of the powder material [4, 5]. In recent times, new sintering methods whereby the compaction of the powder particles is achieved using treatments other than direct heating have emerged. These techniques include laser-based, electric, and microwave sintering processes and are collectively termed "unconventional" sintering (Fig. 1.2) [1, 6]. Over the past years, unconventional sintering methods have been preferred over conventional ones as they offer higher heating rates, less sintering time, and better flexibility in the sense of controlling material properties [4, 7, 8].

Modern-day applications of sintering strive to produce products with intended properties like mechanical strength, toughness, heat resistance, wear behavior, etc [2, 4]. These properties are directly related to the microstructure features which are in turn determined by the sintering process itself. However, achieving the desired microstructure is challenging due to the complex interplay of various factors involved in sintering [1, 9]. These factors include chemical composition, size and shape of powders, atmosphere, pressure, and sintering time [3, 10, 11]. Due to the distinct heating mechanisms in unconventional sintering techniques, additional non-isothermal factors include heating/cooling rate and temperature inhomogeneity [6]. Therefore, it is essential to identify and understand the physical effects and interactions of these factors in the sense of bridging the process parameters, microstructure, and properties of sintered products. This helps to engineer high-performance materials with properties perfectly suited for applications of interest.

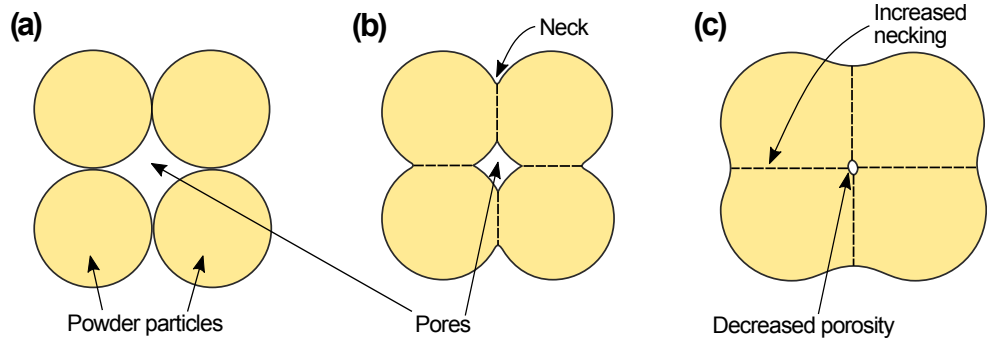


Figure 1.1: Schematic illustration of sintering (a) Packed powder particles before sintering; (b) Particles sinter together reducing their surface area; (c) As sintering progresses, the neck size is increased and pore size is reduced. Adapted from Ref. [12].

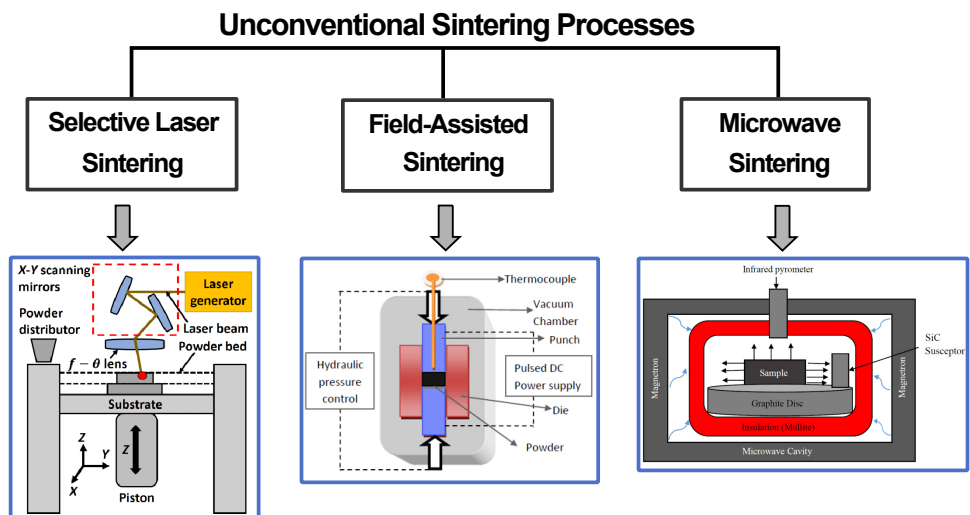


Figure 1.2: Schematic illustrations of unconventional sintering techniques including selective laser sintering, field-assisted sintering and microwave sintering [13, 14, 15].

---

The challenge of developing a framework for process-microstructure-property relations in sintering has been a topic of intense experimental investigations [16]. Currently, most practical approaches rely heavily on trial-and-error experiments, which are expensive and tend to be time-consuming [17, 18]. Furthermore, due to the complexity of the sintering process, it is almost impossible to obtain through experiments the distinct effects of the various physical processes and mechanisms that are obtained in sintering [9]. Consequently, this has led to and encouraged continual interest in the investigation of sintering via modeling and simulation [9, 17]. Unlike conventional trial-and-error methods, simulations offer a better understanding of the fundamental mechanisms governing sintering and their impact on the final microstructure and properties of sintered materials.

The first set of theoretical models describing the sintering process was developed in the 1940s. These include analytical models for the particle-pore evolution, the two-particle coalescence model [19, 20], and the dodeca-/tetrakaidecahedron grain model [21]. Moreover, various models treating the particles using simplified geometries, like spheres or cylinders were developed afterward [22, 23]. A comprehensive description and review of these models is given in Ref. [24]. Nevertheless, complex particle/pore geometry and entangled multi-physics during sintering go beyond the capacity of these models. This limitation necessitates the development of new approaches. In recent times, major advancements have been made in this regard with the development of sintering models that span atomic, microstructure, and macroscopic scales [17, 18, 25]. Also, due to the advent of advanced numerical tools and high-performance computers, simulations of realistic microstructures and large sintering systems have been made possible. A comprehensive overview of modeling and simulation of sintering across various scales can be found in Ref. [18].

Microstructure-scale sintering models stand out from other approaches as they allow simulation at the particle level [17]. This offers a direct investigation of how features like particle size, shape, and porosity influence the final microstructure and properties of sintered products [18]. Among these models, phase-field modeling has emerged as a powerful tool, attracting significant research interest. In the conventional variational phase-field theory, order parameters (OPs) are applied to represent the spatio-temporal distribution of microstructure, i.e. pores/atmosphere and grain orientations in the case of sintering (illustrated in Fig. 1.3). The thermodynamic potential of the microstructure can then be formulated by an energy functional dependent on the OPs, and the interface contribution through the corresponding gradient terms of OPs. From non-equilibrium thermodynamics, the evolution equations of the OPs can be derived based on the variational theory. This approach circumvents the necessity of interface tracking.

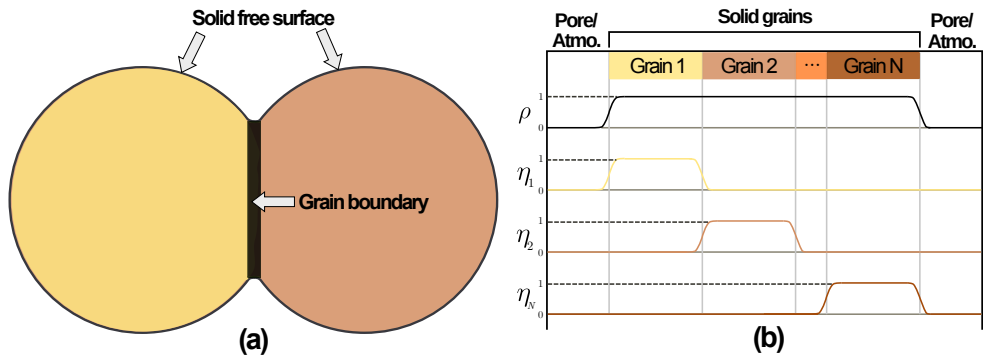


Figure 1.3: (a) Schematic of two-particle coalescence during sintering. The two major types of interfaces in sintering are indicated namely the free surface between pore/atmosphere and solid, and the grain boundary between adjacent crystal grains; (b) Illustration of the order parameters representing the distribution of the microstructure in sintering. OP  $\rho$  indicates the solid, while OPs  $\eta_i$  distinguish the solid grains.

In recent years, variational phase-field models for sintering have emerged, specifically considering isothermal scenarios. For instance, Kazaryan et al. [26] and Wang [27] proposed a line of phase-field model, which was used later for studying different systems [28, 29, 30, 31, 32, 33]. Furthermore, a phase-field sintering model adopting the grand potential concept was also developed [34, 35]. Simulating sintering under heterogeneous thermal environments requires coupling the phase-field sintering model with transient heat and/or chemical diffusion simulations. The phase-field approach allows such consideration through additive inclusion of the energy contributions by the related physical fields, such as temperature or chemical concentration. A recent work introduced a variational non-isothermal phase-field sintering model [36]. This model has been successfully applied to simulate various scenarios, including selective laser sintering on single and multi-layer powder beds [37], as well as sintering processes with a pre-defined high-temperature gradient [6].

On the other hand, one major issue of conventional variational phase-field models involving thermal/chemical diffusive processes is their applicability regarding quantitative modeling and simulation of applicable experimental scenarios. Ideally, for quantitative validity, phase-field models should be projected onto their associated sharp-interface models. Generally, conventional models can only be mapped onto their corresponding sharp-interface models in the limit of negligible interface width (*sharp-interface limit*) [38, 39]. In practice, using extremely small values of interface width for numerical simu-



---

lations is computationally expensive and often impractical. Thus, numerical simulations typically employ interface widths larger than their realistic values [39, 40]. However, this leads to *abnormal interface effects* ranging from the violation of conservation laws to the discontinuity of the chemical/thermal potentials at the interface (trapping effects) [41, 42]. These interface effects tend to become more pronounced with larger interface widths, faster interface movement, and larger asymmetry of diffusion property across the interface [43, 44].

To address these issues, Karma and Rappel [45, 46] introduced the *thin-interface limit* approach. In this approach, interface width is taken as finite, larger than the realistic value but also smaller than any physical length on the microstructural scale. Based on this approach, a quantitative phase-field model for the solidification of pure materials with equal diffusivities in the solid and liquid phases was developed [46]. Moreover, by introducing the so-called *antitrapping current* in the diffusion flux equation, Karma [47] presented a quantitative model for the case of isothermal solidification of alloys with negligible diffusivity in the solid phase. This term, scaling with interface velocity, corrects for the trapping effect at the interface. Furthermore, for the case with arbitrarily different diffusivities in neighboring phases, corresponding antitrapping terms have been proposed for both isothermal [48] and non-isothermal considerations [44].

While the antitrapping term enhances quantitative validity, the modification of variational phase-field models with this term implies that the variational nature of these models cannot be guaranteed. Thus, non-equilibrium thermodynamics is not satisfied. To address this limitation, there have been efforts to develop variational formulations of quantitative phase-field models. One such effort is the so-called *non-diagonal model* [49, 50, 51, 52]. In this model, variational formulation of quantitative phase-field models is developed by considering kinetic cross-coupling between the conserved diffusion fields and the nonconserved fields. This approach is based on phenomenological linear relations and Onsager's symmetry. Consequently, the diffusion equation of the model exhibits a cross-coupling term which can be likened to the *antitrapping current*. Another procedure for the variational formulation of quantitative phase-field models was proposed by Ohno et al. [38, 40]. This approach, called the *two-phase variational approach* enforces diffusion fields mixture laws as constraints in the thermodynamic potential. This gives rise to cross-coupling terms in the evolution equations which serve to eliminate interface effects.

Based on an extensive literature review, there is currently no quantitative phase-field model for the non-isothermal sintering process, regardless of its variational formulation. In most sintering systems, the free surface between the solid and pores exhibits significant asymmetry in diffusion properties (mass and thermal). This asymmetry implies

---

more pronounced *abnormal interface effects* in conventional phase-field simulations. Furthermore, a key challenge in the quantitative phase-field modeling of sintering lies in the representation of the free surface with a conserved field. This poses additional challenges compared to current quantitative non-isothermal solidification models that employ non-conserved fields. The development and applicability of a quantitative phase-field model for the non-isothermal sintering process derived in a variational manner is what this study aims to do.

## 1.2 Objectives and Outline

The overall aim of this study is to develop a variational quantitative phase-field model for the non-isothermal sintering process, verify its validity, and further examine the significance of the proposed model using numerical simulations. This study explores the several interface effects relevant to phase-field modeling and simulation of the non-isothermal sintering process. These effects include modification of mass and energy conservation laws, discontinuities of chemical/thermal potentials at the interface, and the deviation in bulk values of conserved OP across the free surface. The examination of these effects is essential as it facilitates the formulation of the quantitative model devoid of abnormal interface effects. In addition, validation of the proposed model in the sense of eliminating interface effects is essential. This involves numerical simulations incorporating both thermal and microstructural scenarios, and further highlighting the differences between conventional phase-field models of sintering and the proposed quantitative model.

Moreover, practical applications of the proposed model are needed. In particular, sintering simulations of yttria-stabilized zirconia (YSZ) micro-particles are considered. YSZ is selected as a model system as it provides phase stability during sintering. During the sintering of YSZ material, there is no solid-state phase transition at temperatures lower than the melting point [53, 54]. This allows sintering simulations without incorporating property changes due to phase transitions, simplifying the demonstration of the quantitative model.

The structure of the subsequent chapters in this work is given below:

**Chapter 2** This chapter focuses on the basic concepts of the sintering phenomenon in polycrystalline materials. It gives an introduction to core concepts like sintering categories, and the various mechanisms governing material transport during sintering. The subsequent section explores the detailed analytical descriptions of the sintering

---

phenomenon. This section presents geometrical models describing microstructural changes at the initial, intermediate, and final stages of sintering. Finally, this chapter gives an overview of several unconventional sintering techniques, including selective laser sintering, spark plasma sintering, flash sintering, and microwave sintering.

**Chapter 3** In this chapter, the fundamentals of phase-field modeling and simulation, and the application to the sintering process are presented. This chapter gives an introduction to the basic concepts of phase-field, and variational formulations in phase-field models. It summarizes the sharp and thin interface limits of phase-field models and the abnormal interface effects inherent to variational phase-field models. Moreover, a summary of quantitative phase-field modeling and simulation is given. This chapter then discusses the application of phase-field modeling to the sintering process. It introduces various models employed for the simulation of isothermal and non-isothermal sintering processes. In addition, a general background on a widely used numerical technique, the finite element method, is presented.

**Chapter 4** Within this chapter, a variational quantitative phase-field model suitable for the non-isothermal sintering process is derived based on the basic principles of non-equilibrium thermodynamics. The explicit formulations of the model including thermodynamic potentials, and the governing equations are presented. A sharp-interface description of the non-isothermal sintering process is also given. This is essential as it serves as the basis of an asymptotic analysis that links the parameters of the quantitative model to that of the sharp-interface model. This chapter also explores the importance of establishing this linkage and the significance of the proposed anisotropic interpolation scheme of diffusion mobilities. Lastly, it also gives a detailed theoretical analysis of the deviation of the conserved order parameter across free surfaces.

**Chapter 5** This chapter focuses on the numerical implementation and verification of the proposed model. It starts with the details of the finite element-based numerical implementation of the governing equations. Moreover, this chapter also demonstrates the verification of the model using diffusion-driven reshaping simulations. It discusses the potential of the model in the sense of eliminating interface effects via a comparison of the proposed model and existing models. This involves numerical simulations of two-particle coalescence, and a comparison of the thermo-microstructural evolutions and sintering kinetics. In addition, a numerical analysis of the deviation of the conserved order parameter across free surfaces is given in this chapter.

---

**Chapter 6** Following the verification of the proposed model, this chapter demonstrates practical applications of the model via 3D simulations of the sintering of YSZ micro-particles. Isothermal and non-isothermal scenarios are considered with particular emphasis on the investigation of microstructure evolution, density distribution, and temperature profile distribution. Moreover, this chapter examines the differences between simulations obtained using the proposed quantitative and conventional non-quantitative models.

**Chapter 7** The major conclusions and outlook of this study are summarized within this chapter. This includes descriptions of the various directions of future research based on the framework of the proposed model.

---

## 2 Sintering Mechanisms of Polycrystalline Materials

---

This chapter presents a general background on the sintering process introducing basic concepts of sintering, sintering mechanisms, and theoretical models as applicable to the sintering of polycrystalline materials. In Section 2.1, an introduction to the sintering process is presented. Subsections 2.1.1 and 2.1.2 describe the different categories of sintering and the various material transport mechanisms obtainable in the sintering process, respectively. Section 2.2 contains a detailed analytical description of sintering. The geometrical models for the initial, intermediate, and final stages of sintering are presented in this section. Finally, Section 2.3 introduces different unconventional sintering techniques with an emphasis on selective laser sintering, spark plasma sintering, flash sintering, and microwave sintering.

### 2.1 Concepts of Sintering

Sintering is a densification technique that utilizes thermal and/or pressure treatments to transform loose powder particles into bulk materials and components [10, 11, 55]. One of the oldest human technological processes, its origins can be traced to the field of pottery where bricks were formed by heating clay materials in an open pit fire. In ancient times, sintering was broadly applied to manufacture different forms of metallic jewelry and tools [8, 10]. In the modern era, sintering has become an important technique in the processing of different engineering products [11]. It has been vastly exploited in the field of powder metallurgy for fabricating bulk metallic components, in the ceramic industry for fabricating ceramic components with intricate shapes, and also for processing of polymers like polyamides [11, 17, 56]. The combination of high strength and toughness observed in sintered components have made them attractive for various technological systems [17]. Typical examples of sintered components include automotive transmission

---

gears, belt pulleys, electronic capacitors, shock absorber pistons, and watch cases [11, 17].

A critical objective in the employment of the sintering technique is to manufacture components with intended microstructure and properties. This is accomplished via modification of the different variables associated with the overall sintering process [10, 16]. Various variables can be adjusted to produce a microstructure with the desired grain size, sintered density, and distribution of grains and pores. Moreover, they can be broadly classified into two categories: *material variables and process variables*. Material variables include the *chemical composition of powder particles, powder size/shape, powder size distribution, degree of agglomeration, and concentration of impurities* [10]. These variables are intrinsic features of the unsintered powder particles and they mostly determine the compressibility and sinterability of the powder particles. Process variables are generally associated with the thermodynamics of the sintering process. These variables include *temperature, pressure, hold time, atmosphere, heating rate, and cooling rate* [10, 11].

In a typical sintering process, powder particles are bonded together with accompanying changes in the grain and pore structure [11]. The evolving microstructure is driven by a reduction in the interfacial- and surface energies of the consolidated particles [3, 10, 55]. The reduction in the interfacial energy occurs via two key mechanisms: densification and grain growth. As particles bond and densify, the overall interfacial energy between them reduces. Also, as they grow and increase in average size, the total interfacial area reduces [3, 10]. Furthermore, the bonding of particles reduces the overall surface energy by reducing the total surface area of the packed particles [55, 57]. However, in crystalline materials, this leads to an initial increase in the total grain boundary area as the original particle surfaces transform into grain boundaries. Subsequently, grain growth occurs, reducing the overall grain boundary area with a simultaneous reduction in the number of grains and pores [11, 55]. The complex interplay between the various sintering parameters, physical processes, and the resulting microstructure of sintered components has encouraged and led to intensive research that aims to understand these interactions and their resultant effects on the properties of sintered materials.

### **2.1.1 Categories of sintering**

Generally, sintering processes can be classified into three categories: solid-state sintering, liquid-phase sintering, and viscous-flow sintering. As illustrated in Fig. 2.1, the classification is majorly based on the composition of powder particles, sintering temperature, and also the extent to which a liquid phase is present during sintering [17, 58].

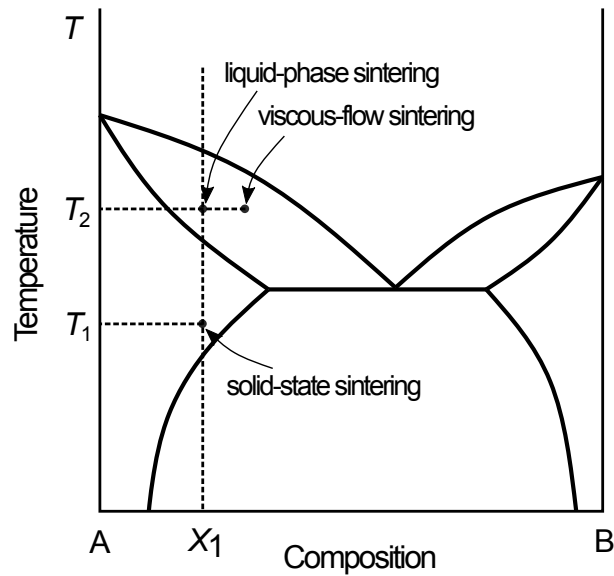


Figure 2.1: Illustration of the categories of sintering for particles with composition A-B [10].

### Solid-state sintering

The sintering of powder particles at a suitably high temperature below the melting point is called solid-state sintering [58, 59]. In this case, the particles sinter spontaneously in the solid state without the formation of a liquid phase [59]. As illustrated in Fig. 2.1, solid-state sintering occurs for A-B powder particles at a composition  $X_1$ , and temperature  $T_1$ . Densification is solely obtained through the reshaping of the particles which occurs via atomic diffusion in the solid state [10, 58]. This process is driven by a reduction in the interfacial energy which is achieved through a reduction of the solid-atmosphere interfaces and subsequent increase in grain boundary areas [3, 58]. Typically, the formation of the grain boundaries is accompanied by grain growth where individual particles coalesce with simultaneous migration of the grain boundaries [59]. General observations associated with solid-state sintering include a reduction in surface area and an increase in the strength of the consolidated particles [59]. As a technique, solid-state sintering has been employed for the fabrication of high-strength components such as alumina lamp envelopes and ceramic magnets [58].

---

Starting from packed powder particles, the evolution of the microstructure during solid-state sintering can be divided into three major stages [11, 59]. The initial stage is defined by the formation and growth of concave necks between neighboring particles and is typically governed by short-range atomic motion. Since individual particles have different crystal orientations relative to one another, grain boundaries are formed in the necks during this stage [11]. At the intermediate stage of solid-state sintering, the necks between the grains enlarge and also impinge on one another to create smooth pore regions. Thus, the grain boundary area is increased as neighboring neck regions overlap. Microstructure at this stage resembles a network of solid grains and channel-like pores [59]. As sintering continues, the channel-like pores transform into closed voids on the grain corners. Most of the densification and grain growth processes occur at this stage. While densification reduces the diameter of the pores, grain growth extends the length of the pores [11]. At the final stage of sintering, grain growth continues with the grain boundaries separating from the pores [59].

### **Liquid-phase sintering**

This category of sintering involves the presence of a liquid phase within the compacted powder particles during sintering [10]. As seen in Fig. 2.1, the composition  $X_1$  and temperature  $T_2$  for A-B powder particles are chosen such that some amount of liquid is formed during the sintering process [58]. While liquid-phase sintering generally starts with mixed solid powder particles, some parts remain solid while the other parts form liquid. A major advantage offered by this process stems from the fact that diffusion in liquid is way faster compared to solid-state diffusion [3, 11]. Thus, the liquid phase provides a faster diffusivity path for the transport of matter into the pores [3]. Though this leads to densification, the quantity of the liquid formed is typically insufficient to fill the pores by viscous flow [58]. To achieve full densification, it is necessary that the grains change shape sufficiently so the amount of the liquid phase can fill all the pore volume [16, 58]. In this case, the driving force for densification is the reduction of the interfacial energy via a reduction in the interface area between the liquid phase and the pores [58]. Most products sintered in industrial settings are usually processed via liquid-phase sintering as it allows the attainment of the full density of the powder compact [11]. Some engineering components like zinc oxide varistors make use of specific properties of the grain boundary that can be easily engineered using liquid-phase sintering [10]. Compared to solid-state sintering, it allows flexible engineering of microstructure and offers a reduction in processing cost.

The microstructure of a component sintered via liquid-phase sintering consists of solid grains with sintered necks bonded together. Starting with powder particles and pores,



---

early densification is obtained via solid-state sintering as the particles are first heated up. The liquid phase is formed at a particular temperature and it remains in existence as long as this temperature is held [11]. At this stage, rapid densification occurs. The powder particles are typically soluble in the liquid thereby they move quickly within it. Faster diffusion implies faster densification, grain growth, and grain reshaping [11, 58]. As the formed liquid spreads, solution-reprecipitation occurs whereby the liquid fills in the pores between the solid grains. Pores are typically characterized by high surface energy and thus are preferentially filled. Subsequently, the solid grains bond and the liquid phase within the pores solidifies on cooling. The final microstructure thus shows a fully densified sintered material with low porosity [3, 11].

### **Viscous-flow sintering**

While sharing similarities with liquid-phase sintering, it differs in the amount of liquid that is formed during the sintering process. As seen in Fig. 2.1, for A-B powder particles, a composition greater than  $X_1$  and a temperature  $T_2$  are chosen such that a considerable amount of liquid is formed during the sintering process [10, 58]. Since the volume fraction of the liquid phase is relatively high, full densification of the consolidated particles is facilitated by the viscous flow of the liquid in between the grains. Different from liquid-phase sintering, there is no need for the solid grains to change shape during densification [10]. Viscous-flow sintering as a technique was usually employed for the sintering of ceramics like porcelain in ancient times [58]. These ceramics contain a mixture of crystalline oxide grains and glassy particles [11]. The glassy particles are amorphous solids and can generally flow under applied forces. While at room temperature no such flow is observed due to high viscosities, the particles soften into viscous liquid at high sintering temperature. Due to differences in surface curvature, the formed liquid flows toward the necks of the solid grains enabling the densification of the particles via the formation of a viscous glass bond [11, 60]. An important advantage of the viscous-flow sintering process is that full density can be obtained for large particles compared to the typical liquid-phase sintering which employs smaller particles [11].

### **2.1.2 Sintering mechanisms**

Powder particles in sintering exhibit differences in surface curvature at various points on their free surfaces. These differences further lead to variations in vapor pressure, bulk pressure, and concentration of vacancies along grain surfaces [10]. These phenomena altogether act as the driving force for sintering inducing material transport via simultaneous contributions of different mechanisms. These mechanisms determine how

mass is transported in response to the driving force [11, 55]. As illustrated in Fig. 2.2, material transport mechanisms include *surface diffusion*, *volume diffusion*, *grain boundary diffusion*, *evaporation-condensation*, and *viscous flow*. For any given sintering process, the dominant mechanism during sintering for a given system depends on various factors such as particle size, neck radius, sintering temperature, and hold time [10, 57].

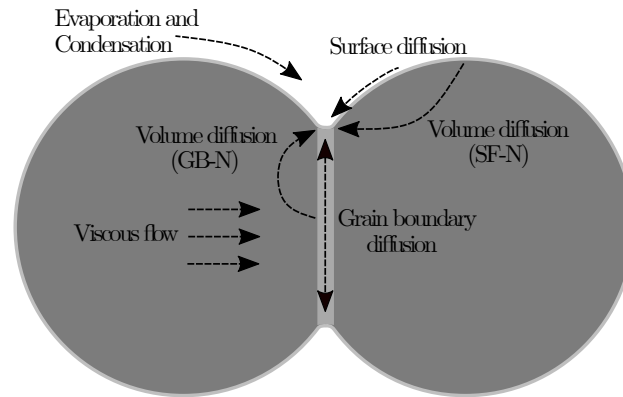


Figure 2.2: Schematic for multiple material transport mechanisms during sintering for two-particle coalescence. "GB-N" represents the volume diffusion path from the grain boundary to the neck region, while "SF-N" represents the volume diffusion path from the surface to the neck region.

Moreover, the transport mechanisms can be classified into two major types: bulk transport and surface transport [11]. While bulk transport mechanisms contribute to densification, surface transport mechanisms do not. This stems from the fact that material transport on the surface only redistributes mass to reduce the surface area and eliminate the curvature gradients [10, 11]. Thus, although neck size is increased, interparticle distances are not reduced. On the other hand, material transport mechanisms in the bulk transfer mass from inside the solid particles to the pore regions which leads to the reduction in interparticle distances [10, 11]. In the theoretical treatment of these mechanisms, the pores are assumed to be large areas of vacancies [3, 11]. Hence, theoretically, material transport mechanisms occur due to a difference in vacancy concentration [10].

### Surface diffusion

Sintering due to surface diffusion occurs via the movement of atoms along the surface

---

of the particles [10]. Surfaces of crystalline materials consist of defects such as surface vacancies, extra atoms, adsorbed atoms, kinks, and terraces [11]. Atomic motion occurs between these defects such as the movement of an atom from a terrace into a surface vacancy. This motion between the surface sites is called surface diffusion [10, 57]. Atomic motion along the surface typically starts with atoms breaking existing bonds on a part of the surface, from thereon atoms move along the surface and reattach at a preferable site. These sites are commonly referred to as the source and sink respectively [11, 57]. While atomic motion is generally random, atoms migrate from surfaces with higher curvature (convex) to those with lower curvature (concave) due to differences in defect concentrations [11]. This leads to a reduction in overall curvature. In sintering, surface diffusion only repositions the atoms along the surface and there is no considerable change in the distance between particles [3, 10, 11]. Thus, no macroscopic shrinkage is observed. However, surface diffusion plays a key role in neck formation between particles. Necks between particles act as sinks for atoms as they are particularly stressed. The subsequent deposition of atoms into the neck regions grows the bond between particles leading to the formation of grain boundaries [11].

Neck growth via surface diffusion is dependent on the volume of atoms that are transferred to the neck surface. This volume of atoms transferred depends on the diffusion area and diffusion flux and the flux itself is dependent on the gradient of curvature and surface diffusivity [10, 11]. Consideration of these factors can be used to estimate the dependency of the neck growth with time, temperature, and particle size.

During the sintering process of most materials, surface diffusion is typically the most dominant mechanism at the early stages [11, 57]. This dominance stems from its relatively low activation energy compared to other transport mechanisms. Hence, surface diffusion is initiated as the particles are heated up to the sintering temperature. Additionally, the high surface area of the powder particles at the early stage of sintering further amplifies its contribution. However, as the surface area reduces, surface diffusion becomes less dominant. Several materials show early-stage sintering dominated by surface diffusion, e.g. iron, nickel, copper, and many ceramics [11].

### **Volume diffusion**

Volume diffusion also termed lattice diffusion, involves the movement of atoms to point defects (vacancies or interstitial sites) via the bulk of the lattice [3, 11]. Independent of temperature, the volume of atoms and vacancies in crystalline materials is conserved [11]. If heat is applied like in sintering, it induces atomic motion whereby atoms on a regular lattice site exchange their position with a vacancy or interstitial site [3, 11]. Since pores are assumed to be large areas of vacancies, atomic motion via volume diffusion implies a

---

flow of atoms into the pores with a counter flow of vacancies into the surrounding solid particles [11]. When an atom moves from the bulk lattice onto the surface, it creates a vacancy. This vacancy can also move around through subsequent motions of atoms inside the bulk thus creating a constant exchange between the atoms and vacancies [11]. While the total number of atoms is conserved in this process, vacancies can be created and eliminated at preferable sites such as pores, grain boundaries, and surfaces [3, 11]. Material transport typically occurs from convex surfaces to concave surfaces due to curvature gradient [10, 11]. The concave surfaces tend to have a higher concentration of vacancies compared to the convex surfaces. Thus, during volume diffusion, there is mass flow from convex points of the solid surfaces to concave points such as the neck region [11].

In sintering, material transport through volume diffusion occurs along different paths as illustrated in Fig. 2.2. One path is from the surface of the solid particles via the particle bulk into the neck surface leading to the transfer of mass to the neck region. Since the material transport occurs from one part of the surface to another, it is not accompanied by densification or shrinkage [10, 11, 57]. Another path for volume diffusion is from the grain boundary to the neck region. The mechanism of volume diffusion in this case typically occurs after neck growth and the emergence of the grain boundary [11]. In this case, densification and shrinkage occur because mass is transported from the contact point of the grains into the neck surface. Thus, there is a reduction in interparticle distance as the sinter bond grows [10].

The rate at which volume diffusion occurs in sintering depends on three major factors which are temperature, composition of solid particles, and stress due to surface curvature or external pressure [11, 57]. The influence of temperature stems from the creation of vacancies and generation of atomic motion as temperature is increased to sintering temperature [57]. For materials with two or more atomic species particularly ionic solids, changes in composition can create vacancies influencing the rate of volume diffusion [11, 57]. Also, if the grain boundaries and/or surface of the solid are under compressive stresses while the neck surface is under tensile stresses, volume diffusion is induced to relax the stress [10, 11]. While volume diffusion is more effective at high temperatures, its contribution to the overall sintering process is minimal, especially for small particles with high surface area. However, for the sintering of several materials such as zirconia, yttrium oxide, and cerium oxide, volume diffusion tends to have a significant contribution [11].

### **Grain boundary diffusion**

In polycrystalline materials, grain boundaries are formed within the neck regions of

---

neighboring solid particles due to the mismatch of the lattice orientations [3, 11]. Due to the grain boundary nature as a defect, mass can be transported along it more rapidly compared to volume diffusion [3]. The activation energy for grain boundary diffusion is typically between that of surface diffusion and volume diffusion [11]. As illustrated in Fig. 2.2, sintering via grain boundary diffusion involves the removal of mass from the grain boundary into the neck surface. While the grain boundary region of crystalline materials is usually narrow, with a width of around 0.5 – 1 nm [3], mass transport along it contributes to densification [10, 11].

Furthermore, the mechanism of grain boundary diffusion depends on grain boundary area per unit volume. At the initial stage of sintering, surface diffusion is highly dominant. However, it reduces in importance as the surface area reduces and grain boundaries emerge [11]. The area of the grain boundary peaks at the intermediate stage of sintering increasing the role of grain boundary diffusion at this stage [57]. Also, the rate of grain boundary diffusion is dependent on grain size. Assuming a constant grain boundary width, the fraction of the area occupied by the grain boundary increases with decreasing grain size leading to increasing influence of grain boundary diffusion [3]. In addition, the grain boundary diffusion mechanism also depends on crystal orientation, temperature, and impurities [11].

#### **Evaporation-Condensation**

Evaporation and condensation represent a form of vapor transport during sintering whereby atoms are repositioned from the pore surfaces into the neck region [11]. In this type of mechanism which is illustrated in Fig. 2.2, atoms evaporate from the surface of the solid and condense in the neck region [10]. This results in the reduction of the total surface area with the simultaneous growth of the neck between neighboring solid particles [11]. Considering that atoms are only repositioned along the surface, there is no change in the interparticle distance hence no densification. Also, the impact of vapor transport on sintering is reduced as the surface area reduces [11].

The driving force for vapor transport in sintering is the differences in vapor pressure. In crystalline materials, evaporation occurs at the convex particle surfaces while condensation occurs at the concave necks due to the slightly reduced pressure [11]. If temperature is increased, vapor pressure increases leading to more mass flux towards the pores. For sintering controlled by evaporation-condensation, the kinetics of the neck growth can be obtained using the Langmuir gas adsorption equation [10].

Vapor transport as a mass transport mechanism is usually not very significant in sintering because of the low vapor pressure of most materials at the sintering temperature [11]. However, in the sintering of small quantities of high-vapor-pressure materials like

---

zirconia, vapor transport is observed [11]. Moreover, the type of sintering atmosphere also affects the significance of the vapor transport mechanism. For example, sintering of zirconia in air gives better densification compared to sintering in a hydrochloric-acid-doped atmosphere where the effect of vapor transport is limited [11].

### **Viscous flow**

The viscous flow mechanism usually occurs in sintering viscous materials like glass or polymers [10]. In this case, material transport to the neck region is driven by the capillary stress from the neck [11]. Hence, the solid particles densify via viscous flow as a response to the stress. Since viscous materials decrease in viscosity as the temperature increases, this leads to a more rapid flow of the material increasing the significance of the viscous flow mechanism. It also implies that the sintering rate increases with temperature. In addition, external stresses can further augment the extent of viscous flow, as they are correlated positively [11].

## **2.2 Geometric Models of Sintering**

For the analytical description of the sintering process, it is generally challenging to obtain a single model capable of describing sintering theoretically while also giving appropriate mass transport equations that can be solved analytically [3]. This is because of the drastic and continual geometry changes during the microstructure evolution of powder particles during sintering. Therefore, the analytical description of sintering involves the division of the entire process into three sequential stages: *the initial stage*, *the intermediate stage*, and *the final stage* [3, 10]. For each stage, a simple idealized geometry that is similar to the microstructure at that stage is assumed. Moreover, for each sintering mechanism, analytical equations for the sintering kinetics can be obtained based on mass transport equations [3].

The analytical models for sintering typically assume that the starting powder particles are uniformly packed, spherical, and of the same size [3]. This implies that a unit of the powder particles can be obtained and analyzed. Thereby the remaining part of the powder particles can be taken as a continuum that has the same macroscopic properties similar to the analyzed unit.

## 2.2.1 Initial stage sintering

The initial stage of sintering involves the formation and growth of the necks between particles via applicable mass transport mechanisms [3, 10]. Curvature considerably decreases during this stage, followed by neck growth and shrinkage [3]. The contribution of the initial stage to the total shrinkage of the compacted powder particles is typically about 2 – 3% [10]. Generally, the initial stage is assumed to last until the radius of the neck is about 0.4 – 0.5 of the particle radius [3].

### Model and geometrical parameters

The geometrical model for the initial stage of sintering is called the *two-sphere model* as it involves two equal-sized spherical particles in contact [3, 10]. As illustrated in Fig. 2.3, two different geometries are considered; one without shrinkage (Fig. 2.3a), and one with shrinkage (Fig. 2.3b). In Fig. 2.3a, the two-sphere model with no consideration of shrinkage shows that while neck size increases with sintering time, interparticle distance is constant. On the other hand, for the two-sphere model with shrinkage in Fig. 2.3b, the neck size increases with sintering time with accompanying interpenetration of the spherical particles [3].

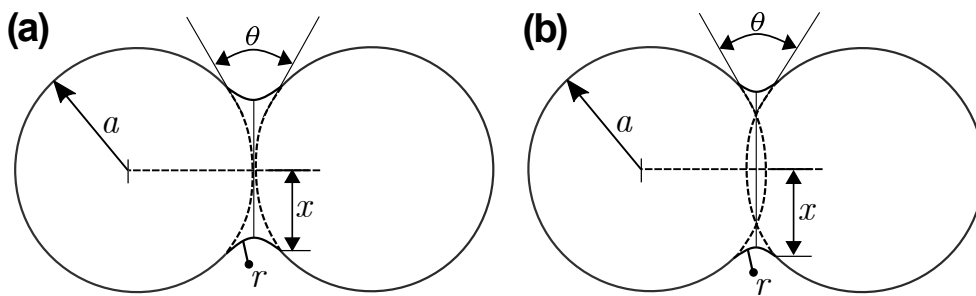


Figure 2.3: Two-sphere model for initial stage sintering. The geometries shown are for (a) without shrinkage and (b) with shrinkage. Geometric parameters include the radius of the solid particle  $a$ , the radius of the neck  $x$ , and the radius of neck curvature  $r$ .  $\theta$  is the dihedral angle.

The neck between the two spherical particles is taken to be circular. Thereby the main geometrical parameters of the model include the radius of the neck  $x$ , the radius of neck curvature  $r$ , the area of the neck  $A$ , and the neck volume  $V$ . Assuming a constant grain size during sintering and also taking a dihedral angle ( $\theta$  in Fig. 2.3) of  $180^\circ$  between the

particles, these parameters can be defined for geometry in Fig. 2.3a with no shrinkage as [10]

$$r \approx \frac{x^2}{2a}, \quad A \approx \frac{2\pi x^3}{a}, \quad V \approx \frac{\pi x^4}{2a}, \quad (2.1)$$

where  $a$  is the radius of the solid particle. For Fig. 2.3b where shrinkage is considered,

$$r \approx \frac{x^2}{4a}, \quad A \approx \frac{\pi x^3}{a}, \quad V \approx \frac{\pi x^4}{4a}. \quad (2.2)$$

Eqs. (2.1) and (2.2) show that the values of the parameters for geometry with shrinkage are half of those without shrinkage [3, 10]. It is also important to note that in realistic systems, the dihedral angle between the particles is less than  $180^\circ$  thereby the parameters above are formulated for idealized cases.

### Kinetic equations

Mass transport in sintering can be understood as the movement of atoms due to the gradient of vacancy concentration. Thus, the transport of mass can be analyzed theoretically using the flux of the atoms or the counter flux of vacancies [3]. Considering atomic movement, the atom flux  $\mathbf{J}_{\text{atom}}$  can be defined as

$$\begin{aligned} \mathbf{J}_{\text{atom}} &= -C_a \frac{D_a}{RT} \nabla \mu_a \\ &= -C_a \frac{D_a}{RT} \frac{\Delta P}{L} V_m, \end{aligned} \quad (2.3)$$

where  $C_a$  is the atom concentration per unit volume,  $D_a$  is the diffusion coefficient of the atom,  $\mu_a$  is the chemical potential of the atom,  $R$  is the gas constant, and  $T$  is temperature.  $\Delta P$  is the pressure difference,  $L$  is the diffusion distance, and  $V_m$  is the molar volume of the solid particles. On the other hand, for vacancy movement, the vacancy flux  $\mathbf{J}_{\text{vac.}}$  can be defined as

$$\mathbf{J}_{\text{vac.}} = -D_v \nabla C_v, \quad (2.4)$$

where  $D_v$  is the vacancy diffusion coefficient and  $\nabla C_v$  is the gradient of the vacancy concentration. Eqs. (2.3) and (2.4) show that the driving forces for the atomic and vacancy motion are differences in pressure ( $\Delta P$ ) and vacancy concentration ( $\nabla C_v$ ) respectively. In sintering, these driving forces are related to the differences in the surface curvature of the solid particles [10]. For the two-sphere model in Fig. 2.3,  $\Delta P$



can be obtained as

$$\begin{aligned}\Delta P = P_a - P_r &= \gamma_{sf} \left( \frac{2}{a} + \frac{1}{r} + \frac{1}{x} \right) \\ &\approx \frac{\gamma_{sf}}{r},\end{aligned}\quad (2.5)$$

where  $a \gg x \gg r$  and  $\gamma_{sf}$  is the surface energy. Furthermore,  $\nabla C_v$  is defined as

$$\nabla C_v \approx C_{v,\infty} \frac{V_m^v \gamma_{sf}}{RT r}, \quad (2.6)$$

where  $C_{v,\infty}$  is the equilibrium vacancy concentration for a flat stress-free surface [3], and  $V_m^v$  is the molar volume of vacancies. Substituting Eqs. (2.5) and (2.6) into (2.3) and (2.4) gives similar expression considering that  $D_a C_a = D_v C_v$ . However, the flux  $\mathbf{J}_{\text{atom}}$  which is driven by the chemical potential gradient of atoms is more generally accepted than  $\mathbf{J}_{\text{vac}}$  driven by vacancy concentration gradient [10].

To obtain the sintering kinetics for the two-sphere model at the initial stage of sintering, the neck size is taken to be much smaller than the grain size ( $x/a < 0.2$ ) [10]. Furthermore, the rate of change of the neck volume  $V$  is defined as

$$\frac{dV}{dt} = \mathbf{J}_{\text{atom}} A V_m, \quad (2.7)$$

and the shrinkage is defined as

$$\frac{\Delta l}{l} = \frac{r}{a}, \quad (2.8)$$

where  $l$  is original length [3, 10]. Depending on whether shrinkage is considered or not, Eq. (2.7) can be further formulated using the expressions in Eqs. (2.1) and (2.2). In addition,  $\mathbf{J}_{\text{atom}}$  can be further expressed depending on the mass transport mechanism. A summary of the kinetic equations for various mechanisms is given in Table 2.1 [10].

Here, I note the general assumptions and limitations of the two-sphere model described above. First, it is assumed that sintering occurs under a quasi-equilibrium state, therefore the diffusion gradient is steady, and the time taken to achieve this steady state is neglected [10]. Also, the extension of the model geometry to real powder particles is only valid for uniformly arranged spherical particles of similar size which is quite different from realistic systems [3]. Finally, the assumption of the  $180^\circ$  dihedral angle between the particles implies that the neck surface is circular which is a gross simplification compared to real powder particles [3].

Table 2.1: A summary of the kinetic equations for various mass transport mechanisms where  $D_{sf}$ ,  $D_v$ , and  $D_{gb}$  are the surface diffusion, volume diffusion, and grain boundary diffusion coefficients respectively.  $l_{sf}$  and  $l_{gb}$  are the diffusion thickness of surface and grain boundary diffusion respectively.  $M$  is the molar weight of the solid material and  $d = M/V_m$  is the solid density.  $p_\infty$  is vapor pressure.  $\eta$  is the viscosity of the material.  $t$  is time.  $^+$  is volume diffusion from grain boundary and  $^*$  is volume diffusion from surface.

Sintering mechanism	Neck growth	Shrinkage ( $\Delta l/l$ )
1. Surface diffusion	$x^7 = \frac{56D_{sf}l_{sf}\gamma_{sf}V_m a^3}{RT} t$	
2. Volume diffusion <sup>+</sup>	$x^4 = \frac{16D_v\gamma_{sf}V_m a}{RT} t$	$\left(\frac{D_v\gamma_{sf}V_m}{RT a^3}\right)^{1/2} t^{1/2}$
3. Volume diffusion <sup>*</sup>	$x^5 = \frac{20D_v\gamma_{sf}V_m a^2}{RT} t$	
4. Grain boundary diffusion	$x^6 = \frac{48D_{gb}l_{gb}\gamma_{gb}V_m a^2}{RT} t$	$\left(\frac{3D_{gb}l_{gb}\gamma_{gb}V_m}{4RT a^4}\right)^{1/3} t^{1/3}$
5. Evaporation-Condensation	$x^3 = \sqrt{\frac{18}{\pi}} \frac{p_\infty\gamma_{sf}}{d^2} \left(\frac{M}{RT}\right)^{3/2} at$	
6. Viscous flow	$x^2 = \frac{4\gamma_{sf}a}{\eta} t$	$\frac{3\gamma_{sf}}{8\eta a} t$

## 2.2.2 Intermediate stage sintering

After the formation and growth of necks between particles at the initial stage of sintering, smooth pore regions are formed as interconnected channels along 3-grain edges [10]. The intermediate stage of sintering begins when these pores reach their equilibrium shapes which is determined by the interfacial energies [3]. At this stage, significant densification of the consolidated particles occurs. Typically around 90 – 93% of the relative density is obtained at this stage [3, 10]. It is assumed that the densification occurs due to the pores further shrinking to reduce cross-sectional area [3].

### Model and geometrical parameters

The geometrical model for the intermediate stage of sintering as proposed by Coble [22] is illustrated in Fig. 2.4a [10]. In this model, the unit cell of the microstructure is taken as packed *tetrakaidecahedral* grains with an array of cylindrical pores along the grain edges [3, 10]. Moreover, it is assumed that the pores shrink equally in a radial direction [10]. The geometry in Fig. 2.4a is a tetrakaidecahedron with 36 edges, 24 corners, and 14 faces. The volume  $V_t$  can be defined as [3]

$$V_t = 8\sqrt{2}l_p^3, \quad (2.9)$$



where  $l_p$  is the edge length of the tetrakaidecahedron. Since each pore is shared by three tetrakaidecahedral grains, the volume of each pore is

$$V_p = \frac{1}{3}(36\pi r^2 l_p), \quad (2.10)$$

where  $r$  is the radius of the pore. The porosity of the tetrakaidecahedron  $P_c = V_p/V_l$  is defined as

$$P_c = \frac{3\pi}{2\sqrt{2}} \frac{r^2}{l_p^2}. \quad (2.11)$$

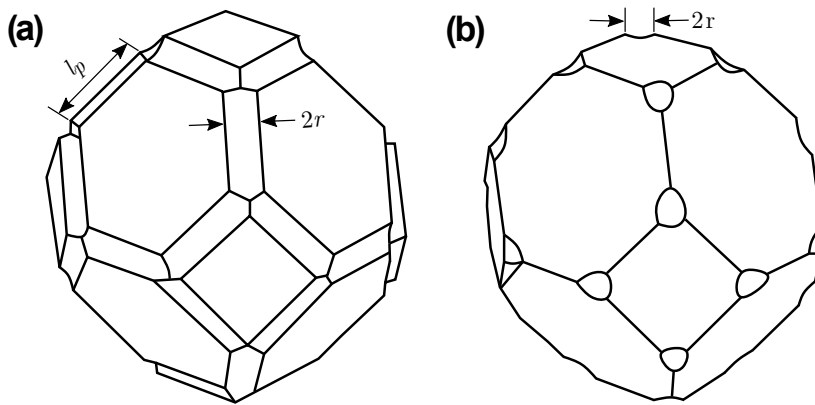


Figure 2.4: Geometrical models for (a) intermediate stage and (b) final stage sintering. Adapted from [10].

### Kinetic equations

The model assumes a uniform geometry for all the pores implying that the chemical potential is the same at all points on the pore surface [3]. Thus, mass transport mechanisms that involve the repositioning of atoms without densification are not applicable. Thereby only mass transport mechanisms with densification which are volume diffusion, and grain boundary diffusion are applicable [10].

Neglecting the shape effects at the corners of the tetrakaidecahedron, atomic flux towards the cylindrical pores can be likened to thermal flux in an electrically heated cylindrical

wire. The atomic flux per unit length  $\mathbf{J}_{\text{atom}}$  is given as [3, 10]

$$\mathbf{J}_{\text{atom}} = 4\pi \frac{D_a}{RT} \Delta P \quad (2.12)$$

$$= 4\pi \frac{D_a}{RT} \frac{\gamma_{\text{sf}}}{r}, \quad (2.13)$$

where Eq. (2.5) has been taken into account. Furthermore, sintering equations for volume diffusion and grain boundary diffusion are given below.

#### *Volume diffusion*

Assuming that pore shrinkage occurs at all 14 surfaces of the geometry in Fig. 2.4a, the rate of volume change of the pore can be defined as

$$\frac{dV_p}{dt} = -\frac{14}{2} 2r \mathbf{J}_{\text{atom}} V_m \quad (2.14)$$

$$= -14r 4\pi \frac{D_v}{RT} \frac{\gamma_{\text{sf}}}{r} V_m. \quad (2.15)$$

The rate of the porosity change can be expressed as

$$\frac{dP_c}{dt} = \frac{dV_p}{dt} / V_t = -\frac{d\rho}{dt}, \quad (2.16)$$

where  $\rho$  is the relative density which rate is obtained as

$$\frac{d\rho}{dt} = \frac{336D_v \gamma_{\text{sf}} V_m}{RTG^3}, \quad (2.17)$$

where  $G$  is the grain size defined as  $(\pi/6)G^3 = V_t$ . If  $G$  is taken as a constant i.e. grain size is constant during sintering, then obtaining relative density  $\rho$  is a simple integration of Eq. (2.17). However, this is not the case in realistic systems. In this case,  $G$  needs to be expressed in terms of the grain growth equation [10].

#### *Grain boundary diffusion*

Similar to that of volume diffusion, the rate of volume change of the pore can be obtained as [3, 10]

$$\frac{dV_p}{dt} = -\frac{14}{2} 4\pi \frac{D_{\text{gb}}}{RT} \frac{\gamma_{\text{sf}}}{r} l_{\text{gb}} V_m, \quad (2.18)$$

where  $l_{\text{gb}}$  is the diffusion thickness of grain boundary diffusion. Also, similar to the procedure for volume diffusion, the rate of density change is derived as

$$\frac{d\rho}{dt} = -\frac{854D_{\text{gb}} l_{\text{gb}} \gamma_{\text{sf}} V_m}{RTG^4} \left( \frac{1}{P_c} \right)^{1/2}. \quad (2.19)$$

While the geometrical model for the intermediate stage of sintering is idealized and hence is limited in terms of describing realistic sintering scenarios, it offers a simplification of the sintering complexity at this stage allowing reasonable evaluation of sintering kinetics [10].

### 2.2.3 Final stage sintering

The final stage of sintering begins after the disconnection of the pore channels and further isolation of the pores at the grain corners [3, 10]. At this stage, the pores are assumed to shrink further leading to their possible disappearance [3]. Final densification of the powder compact is achieved at this stage [10].

#### Model and geometrical parameters

The geometrical model for the final stage of sintering was also proposed by Coble [22] and it is illustrated in Fig. 2.4b [10]. The microstructure is taken as *tetrakaidecahedral* grains with equal-sized spherical pores at their corners. Since the tetrakaidecahedron has 24 corners and each pore is shared by four tetrakaidecahedral grains, the volume of each pore is [3]

$$V_p = \frac{24}{4} \frac{4}{3} \pi r^3, \quad (2.20)$$

where  $r$  is the radius of the pore. The porosity of the tetrakaidecahedron  $P_c = V_p/V_t$  is defined as

$$P_c = \frac{\pi}{\sqrt{2}} \frac{r^3}{l_p^3}. \quad (2.21)$$

#### Kinetic equations

In this model, the unit cell of the microstructure is taken as a spherical shell of solid material with a single pore at its center [3]. Thus atomic diffusion is defined in terms of concentric sphere diffusion of atoms from a distance  $b$  to the pore surface. The atomic flux  $\mathbf{J}_{\text{atom}}$  along the sphere surface is defined as

$$\mathbf{J}_{\text{atom}} = 4\pi \frac{D_a}{RT} \frac{\gamma_{\text{sf}}}{r} \frac{rb}{b-r}. \quad (2.22)$$

Similar to the geometric model for the intermediate stage, a uniform geometry for all the pores is assumed hence only mass transport mechanisms with densification, volume diffusion, and grain boundary diffusion are applicable [3]. While the original model

---

from Coble [22] gave derivations for only volume diffusion, Kang and Jung [61] derived the densification rate for both volume and grain boundary diffusion obtaining

$$\frac{d\rho}{dt} = \frac{441D_v\gamma_{sf}V_m}{RTG^3}(1-\rho)^{1/3}, \quad (2.23)$$

for volume diffusion and

$$\frac{d\rho}{dt} = \frac{735D_{gb}l_{gb}\gamma_{sf}V_m}{RTG^4}, \quad (2.24)$$

for grain boundary diffusion. The approximations and assumptions made in the geometric model for final stage sintering imply that Eqs. (2.23) and (2.24) are applicable for cases where porosity in the microstructure is  $< 2\%$ .

## 2.3 Unconventional Sintering

Based on the heating technique employed for sintering, it can be further classified into two major categories: *conventional* and *unconventional sintering*. Conventional sintering involves the consolidation of powder particles using traditional means such as temperature and pressure [62]. In order to enhance the properties and functionalities of sintered materials, many new techniques have been proposed and broadly applied in the industry [62]. In these techniques, the thermal bonding effect in the sintering process is introduced by treatments other than direct heating, such as laser scan, electrical current, and electromagnetic field [8, 17, 62, 63]. These techniques are collectively termed as "unconventional" sintering [1, 6]. Some examples of unconventional sintering techniques include *selective laser sintering*, *spark plasma sintering*, *flash sintering*, and *microwave sintering*. Due to the distinct heating mechanisms among unconventional sintering techniques, effects of non-isothermal factors on the properties of products, like heating/cooling rate and temperature inhomogeneity gain increasing attention alongside the conventional ones such as chemical composition as well as the size of powders, atmosphere, and pressure [10]. The major advantages of these unconventional sintering techniques over the conventional methods include flexibility in control of material microstructure and properties, the prospect of higher heating rates, high efficiency with shorter sintering time, and the ability to sinter complex/nearest-net-shape components [7, 8].

---

### 2.3.1 Selective laser sintering

Selective laser sintering (SLS) is one of the most widely used unconventional sintering techniques. It involves compacting powder particles into an already set size and shape via the application of laser beams either in continuous or pulse mode [64]. The sintering equipment emits a laser beam that moves over the loose powder particles. The laser generates heat engendering sinter bonds between the particles. Moreover, the consolidated particles take the desired shape and size [1]. After the first layer of the powder particles is scanned by the laser, a second layer is deposited on it and the process is repeated until the desired component is formed [64]. Since the scanning parameters of the laser beam can be adjusted, it implies that the heating rate as well as the shapes and size of sintered components can be varied [1].

SLS as a technique is predominantly employed for polymers such as wax and nylon [1]. Currently, there are about two SLS methods for the processing of metals and ceramics: direct method and indirect method. The direct method is simply the SLS technique as described earlier. On the other hand, the indirect method involves covering the metal or ceramic powder particles with a layer of polymer. As the laser beam scans the loose particles, it melts the polymer layer which joins the particles together. The processed component is further placed in an oven for subsequent sintering and the removal of the polymer [1].

### 2.3.2 Spark plasma sintering

Spark plasma sintering (SPS) is a type of field-assisted sintering technology (FAST) technique, and its sintering method is similar to the conventional hot pressing sintering technique. It employs the use of direct current combined with parallel application of mechanical pressure [1]. The method of heat generation in SPS involves passing an electrical current through the material for an electrically conductive material to generate Joule heating or by passing an electrical current to a sintering tool which then passes heat to the material via conduction in cases where the material to be sintered is not electrically conductive [65, 66]. Due to the low electrical conductivity of most materials sintered via SPS, low voltage is typically applied to generate sufficient current for the sintering process [1].

In the SPS method, a very high heating rate is normally observed leading to a reduction in sintering time and cost. Moreover, the simultaneous use of mechanical pressure ensures that higher densification is obtained in the sintering component while grain growth is limited [1].

---

### 2.3.3 Flash sintering

Flash sintering (FS) is another FAST approach with the presence of the so-called “flash event”. In this sintering process, material particles are simultaneously exposed to heat and electric fields in the range of 7.5V/cm and 1000V/cm [62]. The application of the electric field allows a flow of current inside the sintered component. The "flash event" observed across the powder particles in FS implies that the entire sintering process is fast. Also, sintering occurs at a temperature lower than conventional sintering temperature [1]. Compared to other techniques, the FS process largely suppresses grain growth. Therefore, functionalized materials with nano-structured powder particles can be sintered [1].

The major advantage of the FS process is the large reduction in sintering time and temperature [1]. Overall sintering process in FS is generally taken to be less than a minute [62]. The time and temperature needed for the densification of the particles are lesser when compared to other techniques.

### 2.3.4 Microwave sintering

Microwave sintering (MS) is a type of unconventional sintering method mostly used in the ceramic industry. It involves the application of heat to materials via exposure to microwave energy at a frequency between 300Mhz to 300Ghz [7]. The heat generation in the MS process is alluded to as the production of electromagnetic energy whereby the interaction of the microwave radiation with the material causes heating within the material [1]. The use of MS as a technique induces uniform heating in the material which increases the diffusion process, leading to higher heating and reduction of sintering time. Compared to the conventional sintering method of heating powder particles in ovens, MS allows better densification at a shorter time, higher sintering rates, lower sintering temperature, and structural homogeneity of the sintered components [1].



---

## 3 Fundamentals of Phase-field Modeling and Simulation

---

Within this chapter, the fundamentals of phase-field modeling and simulation and its application to the sintering process are presented. Section 3.1 gives an introduction to the phase-field theory wherein basic concepts and variational formulations of phase-field models are presented. Moreover, Section 3.1 contains discussions regarding sharp and thin interface limits of phase-field models, abnormal interface effects associated with phase-field models, as well as a summary of quantitative phase-field modeling and simulation. In Section 3.2, the application of phase-field modeling to the sintering process is presented. A review of the various models employed for the simulation of isothermal and non-isothermal sintering processes is given in this section. Lastly, the basics of the finite element method, a widely used numerical method in modeling and simulations are presented in Section 3.3.

### 3.1 Phase-field Theory

The microstructures of most engineering materials can generally be described as a convolution of different inhomogeneities mostly inherited during materials processing [67]. These microstructures may often consist of grains with different orientations, spatially dispersed phases that differ in crystal structure and/or chemical composition, domains with different magnetic/electrical polarization, and different forms of structural defects. The properties exhibited by materials heavily rely on the size, shape, and spatial distribution of the different features of the microstructure [67, 68]. Hence, it is highly imperative that a deep understanding of the mechanisms of microstructure formation and evolution is obtained. However, microstructure evolution is not a straightforward process as it involves the interaction of several complex phenomena. A microstructure can be seen as a thermodynamically unstable structure that evolves to reduce the total

---

free energy which may include local chemical free energy, interface energy, magnetic energy, elastic strain energy, electrostatic/magnetic energy, and applied external fields [67, 68]. The intricate and nonlinear feature of microstructure evolution has necessitated the use of theoretical and numerical tools for extensive understanding [39, 67].

In the conventional theoretical modeling of microstructure evolution, the interfacial regions between structural/compositional domains are taken to be infinitely sharp (see Fig. 3.1a) [67, 68]. The kinetics of microstructure evolution are then described by a set of differential equations defined in the domains alongside specific boundary conditions that govern the thermodynamics of the interface [39, 68]. A common example is the non-isothermal solidification of a pure material. In this case, heat diffusion equations can be defined for the individual phases. Moreover, two specific conditions are defined at the solid-liquid interface; an energy conservation condition where the flux of heat from one side of the interface is equivalent to the heat flux from the other side (Stefan condition), and an interfacial temperature equation that takes into account interface curvature (Gibbs-Thomson condition). The velocity of the interface which is coupled to these boundary conditions is defined such that the effect of latent heat release is taken into account [39, 43].

Models such as the one described above are generally referred to as *sharp-interface models*. There are different limitations as regards the usage of these models. One major limitation is that these models entail the explicit tracking of the positions of the migrating interface which is essential in order to apply the necessary interface conditions. While interface tracking might be achievable for one-dimensional (1D) systems, it becomes impracticable for complex three-dimensional (3D) microstructures [67]. Also, intricate interactions such as merging between interfaces with complex topologies are very difficult to accurately capture [39]. Thus, simulations based on sharp-interface models are mostly applicable to 1D systems or simplified microstructures [68]. In this regard, other theoretical methods such as *phase-field models* have found extensive usage as they circumvent most of the problems encountered with sharp-interface models. Though early applications of the phase-field method focused on solidification, it has increasingly become a popular tool in the modeling and simulation of a wide range of microstructure evolution processes [69].

### 3.1.1 Basic concept of phase-field

The phase-field method is principally based on the *diffusive-interface* description. The diffusive-interface approach can be dated back to van der Waals [70] who analyzed

liquid-vapor interactions using a continuous density function at the interface. Moreover, this approach was further advanced by Ginzburg and Landau [71] as well as Cahn and Hilliard [72, 73]. In the diffusive-interface approach, a set of field variables also called *order parameters* (OPs) are used to describe the domains and interfaces of a microstructure. These OPs are typically defined as continuous spatial-temporal functions. Inside the domain regions, the OPs have the same values as in the sharp-interface models, however, the interfaces in particular are described as relatively narrow regions where the OPs gradually vary between their values in the neighboring domains (see Fig. 3.1b). This implies that the positions of the interfaces are inherently given by the contour of the values of the OPs in the domains. Hence the temporal evolution of the OPs is a representation of the microstructure evolution over the whole system. Furthermore, the diffusive nature of the interfaces helps phase-field models circumvent the necessity of explicit interface tracking thereby making it possible to predict and simulate the microstructural evolution of complex morphologies [67, 68].

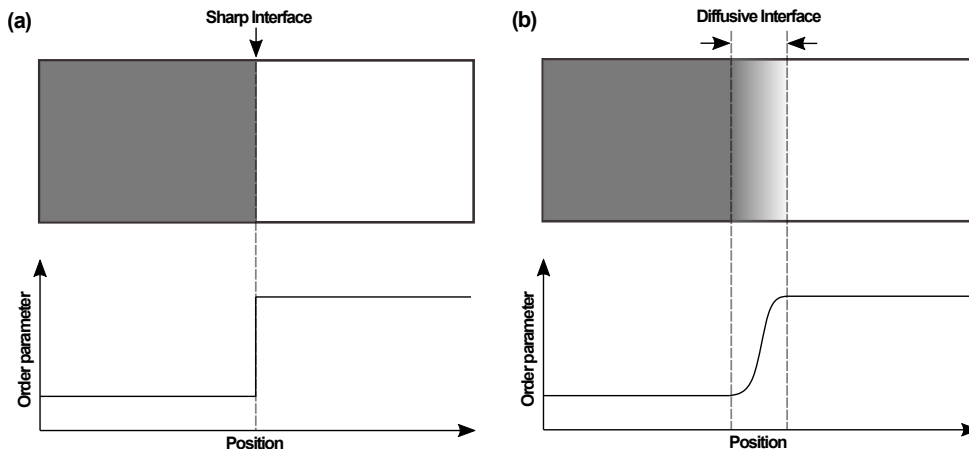


Figure 3.1: Schematics of (a) Sharp, and (b) Diffusive interfaces.

A typical order parameter  $\phi$  in a phase-field model can be understood as an average of a specific thermodynamic property or the average of a spatially varied local order parameter field  $\Phi(\mathbf{r})$  of a phase. The bulk order parameter  $\phi$  can be interpreted as the spatial average of the local field  $\Phi(\mathbf{r})$  over the whole phase/domain, that is,  $\phi = \langle \Phi(\mathbf{r}) \rangle$  [39]. Moreover, depending on the properties that OPs represent, they can be classified into two main categories: *conserved* and *non-conserved*. Order parameters related to

---

conserved quantities are called conserved OPs as the global integral of the OPs over space gives a constant value during microstructure evolution. A common example of a conserved OP is the total solute concentration in a closed system. On the other hand, non-conserved OPs are associated with non-conserved quantities whereby their global integral over space is not conserved. Common examples include magnetization, local crystal structure, and grain orientations [39, 68].

### 3.1.2 Variational formulations

#### Thermodynamics

Generally, phase-field models are linked to thermodynamics by a potential density like entropy and free energy which are defined in terms of the OPs and other associated field variables like temperature, strain, etc [39]. The dissipative minimization of the free energy (or maximization of the entropy) drives the dynamics of the OPs and other related fields. Due to the diffusive-interface description of phase-field models, the thermodynamics of both the bulk domains and interfaces in a microstructural system are considered [69]. Thus, for a system with spatially varied OP  $\phi(\mathbf{r})$ , the total free energy  $F$  would be formulated as a functional considering its dependency on  $\phi$  as well as on its gradient  $\nabla\phi$ . The formulation of the free energy  $F$  for the diffusive-interface description as introduced by Cahn and Hilliard [72] is

$$F(\phi, \nabla\phi) = \int_{\Omega} \left[ f_{\text{loc}}(\phi) + \frac{\kappa}{2} |\nabla\phi|^2 \right] d\Omega, \quad (3.1)$$

where  $f_{\text{loc}}$  is the local free energy density which is a function of the OP  $\phi$ . The local free energy  $f_{\text{loc}}$  constitutes one of the main components of phase-field models [67]. It is usually defined as a function of the OPs and it is formulated to reflect the possible equilibrium conditions of coexisting phases or bulk domains [68]. For a non-conserved OP,  $f_{\text{loc}}$  has minima at the values of the OP which represent the phases (example in Fig. 3.2a). In the case of a conserved OP,  $f_{\text{loc}}$  has a common tangent at the equilibrium values of the OP in the coexisting domains/phases (example in Fig. 3.2b). The gradient term  $(\kappa/2)|\nabla\phi|^2$  in Eq. (3.1) is only nonzero at the interface and it reflects the diffusive nature of the interfaces in phase-field models. The gradient energy coefficient  $\kappa$  can be directly related to the interface energy and width. Generally, gradient energy coefficients are defined as positive so that the gradient terms become thermodynamically unfavorable leading to interface migration [67, 68].

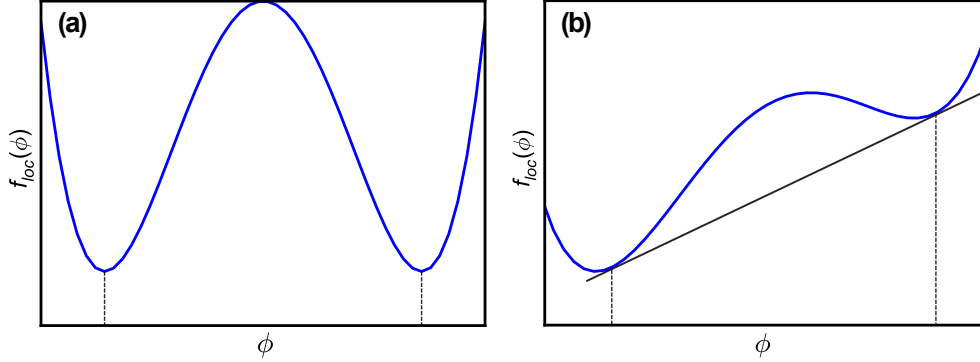


Figure 3.2: Free energy landscape  $f_{loc}(\phi)$  for (a) non-conserved OP where the minima of the free energy represent the equilibrium states (b) for a conserved OP where the equilibrium states are determined by co-tangent law.

### Kinetics

In the phase-field method, the temporal evolution of the OPs is a representation of the microstructure evolution and is characterized by a set of partial differential equations, which are solved numerically [68]. These equations are derived based on the principles of non-equilibrium thermodynamics where it is assumed that a microstructure undergoing evolution is driving towards a state of global thermodynamic equilibrium [39]. Accordingly, the driving forces of microstructure evolution are derived based on the defined thermodynamic potential density. Moreover, these driving forces or their fluxes are used to drive the kinetics of associated OPs. Generally, the kinetic equations of OPs in phase-field models are defined based on the type of associated OP: *conserved* and *non-conserved kinetic equations*.

#### (1) Conserved kinetic equation

The conserved kinetic equation governs the evolution of conserved OPs such as concentration and mass density. This type of equation generally takes the form of a flux-conserving equation [39]. For a system with a conserved order parameter  $\phi$ , the dynamics of the microstructure evolution is basically driven by the gradient of the chemical potential within or between the domains/phases. The local chemical potential in the system  $\mu$  can be obtained from the functional derivative of the total free energy [72] as

$$\mu = \frac{\delta F(\phi, \nabla \phi)}{\delta \phi} = \frac{\partial f_{loc}(\phi)}{\partial \phi} - \kappa \nabla^2 \phi. \quad (3.2)$$

Also, since  $\phi$  is conserved, it obeys the conservation equation

$$\frac{\partial \phi}{\partial t} = -\nabla \cdot \mathbf{J}, \quad (3.3)$$

where  $\mathbf{J}$  is flux. Moreover,  $\mathbf{J}$  can be defined based on linear kinetics, that is,

$$\mathbf{J} = -M\nabla\mu, \quad (3.4)$$

where  $M$  is a kinetic parameter typically diffusion mobility. Combining Eqs. (3.2) - (3.4) readily yields

$$\frac{\partial \phi}{\partial t} = \nabla \cdot M\nabla \frac{\delta F}{\delta \phi}. \quad (3.5)$$

Eq. (3.5) is the popular Cahn-Hilliard equation that implicitly ensures the conservation of OP  $\phi$  and has been widely employed to study various forms of diffusion and transport phenomena.

## (2) Non-conserved kinetic equation

The kinetics of nonconserved OPs like grain orientations and polarization are governed by the non-conserved kinetic equation. The equation is typically formulated to minimize the total free energy or maximize the total entropy as the case may be. The non-conserved OPs evolve following the free energy's steepest functional gradient which consequently pushes the OPs to the minimum of the free energy landscape [39]. Thus, for a system with a non-conserved OP  $\phi$ , the driving force for microstructure evolution can simply be defined as  $\delta F/\delta \phi$ . As there is no constraint on the conservation of  $\phi$ , its dynamic evolution can simply be defined similarly to Langevin dynamics, that is,

$$\frac{\partial \phi}{\partial t} = -L \frac{\delta F}{\delta \phi}, \quad (3.6)$$

where  $L$  is a kinetic parameter. Eq. (3.6) is the Ginzburg-Landau equation popularly referred to as the Allen-Cahn equation [68]. It describes the time evolution of non-conserved OPs and has been widely used to study different processes including solidification and solid-state phase transformation.

### 3.1.3 Sharp and thin interface limits

Although it can be inferred from the preceding discussions that the phase-field method has an extensive connection with the basic principles of thermodynamics and kinetics,

there are however different issues that have hindered the use of phase-field models for quantitative modeling and simulation of applicable experimental scenarios [39]. Due to the diffusive-interface description of phase-field models, an asymptotic mapping of the models onto associated sharp-interface models is needed in order to obtain quantitative simulations of microstructure evolution [39, 44]. The asymptotic mapping of a phase-field model onto the corresponding sharp-interface model is schematically illustrated in Fig. 3.3. In Fig. 3.3, the variations of a non-conserved OP  $\phi$  and a conserved OP  $u$  across a migrating interface are shown. The dashed lines illustrate the projections of the phase-field solutions of  $\phi$  and  $u$ . To map the phase-field model onto its corresponding sharp-interface model, the phase-field solutions of  $\phi$  and  $u$  have to be obtained such that their projections onto a hypothetical sharp interface are equivalent to the values that would be obtained if the sharp-interface model was used [39].

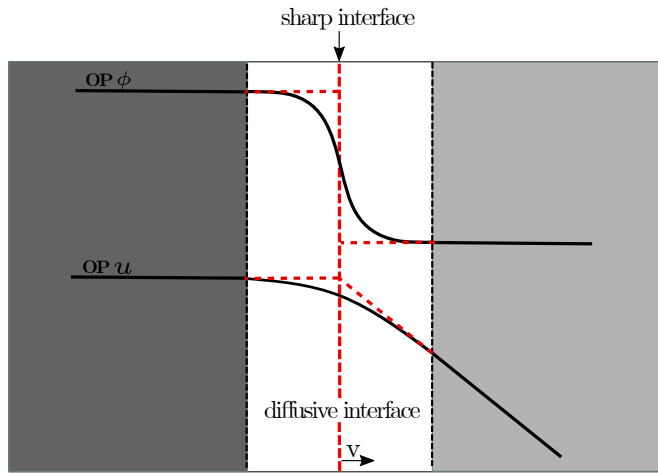


Figure 3.3: Schematic of the variations of OPs  $\phi$  and  $u$  across a diffusive interface. The asymptotic mapping of the phase-field solutions of  $\phi$  and  $u$  require their projections onto a hypothetical sharp interface as shown by the dashed lines.

The asymptotic analysis of extracting the equations of a sharp-interface model from a corresponding phase-field model involves the use of complex mathematical frameworks comprising perturbation analysis. Thereby the perturbative expansion of the solutions of the phase-field equations in the *outer* and *inner regions* (bulk phases and diffusive interface) are obtained in powers of a parameter  $\epsilon$  which is usually related to the

---

interface width and interface velocity. For example,  $\phi$  and  $u$  in Fig. 3.3 would be expanded as  $\phi = \phi_0 + \epsilon\phi_1 + \epsilon^2\phi_2 + \dots$  and  $u = u_0 + \epsilon u_1 + \epsilon^2 u_2 + \dots$ . The defined solutions are then substituted into the phase-field equations, and terms with similar order of  $\epsilon$  are grouped and solved order by order. Also, the solutions obtained in the outer and inner regions are matched using defined matching conditions [38, 39, 40].

One approach that has been used to obtain sharp-interface equations from an associated phase-field model is to consider a limit where the interface width  $l$  of the phase-field model is negligible and can be approximated to zero, i.e.  $l \rightarrow 0$ . This approach widely referred to as the *sharp-interface limit* has been employed to extract sharp-interface equations such as the Stefan and Gibbs-Thomson conditions from the conventional phase-field model of solidification [74, 75, 76]. However, the sharp-interface limit is unfeasible for numerical simulations as the mesh/grid resolution and time scale of the phase-field model are limited by the choice of the interface width [39]. For example, the values of interface width  $l$  are typically in the nanometer range for solid-liquid interfaces, hence a mesh size in the order of Angstrom is needed for numerical simulations. This implies an extremely huge computational cost for the numerical simulations of mesoscale solidification processes [40, 44].

Another approach for the mapping of phase-field models onto corresponding sharp-interface equations is the *thin-interface limit* method developed by Karma and Rappel [45, 46]. In this limit, interface width  $l$  is defined to be finite, larger than the realistic value but also smaller than any physical length on the microstructural scale. Thin interface asymptotic analysis considering the solidification of a pure substance showed that sharp-interface equations can be obtained from the phase-field model for a finite value of  $l$  [43]. Compared to the sharp-interface limit, the thin-interface limit allows quantitative numerical simulations of microstructure evolution for reasonable spatial-temporal scales [39].

The quantitative model developed by Karma and Rappel [45, 46] depends on the assumption of *symmetric diffusion*. It is assumed that the diffusivities in neighboring phases are identical. However, most microstructural processes involving transport phenomena such as heat, solute, or mass transport entail unequal diffusivities in neighboring phases. While extending the thin-interface limit to the case of *asymmetric diffusion*, Almgren [41] showed the existence of various interface effects that scale with interface velocity and the finite interface width. Since the interface width is typically chosen to be larger than the realistic value in numerical simulations, this implies that the interface effects are artificially magnified limiting the use of phase-field models with asymmetric diffusion for quantitative simulations. Explicit discussions on these interface effects and the several methods developed to eliminate them will be presented in subsequent sections.



---

### 3.1.4 Interface-dependent effects

As discussed before, there are different interface effects associated with the phase-field modeling of transport phenomena with asymmetric diffusion. There are two main categories of these effects as analyzed by Almgren [41]. First is the jump of chemical/thermal potentials at the interface which in turn modifies the values of these potentials at the interface. Another category includes the modification of the mass/energy conservation laws at the diffusive interface. Almgren [41] showed that the conservation law obtained from a phase-field model with asymmetric diffusion is modified with extra terms that are not present in the corresponding sharp-interface model.

#### Jump of potentials

The discontinuity of chemical potential and/or temperature across the interface in phase-field models with asymmetric diffusion is perhaps the most prominent interface effect as it is associated with solute and thermal trapping phenomena [42, 43]. The continuity of chemical potential/temperature at the interface is a major assumption in conventional sharp-interface models. For a phase-field model with asymmetric diffusion, jumps of potentials arise when there is diffusion through an interface with finite width and finite mobility [39]. As the mobility at the interface is interpolated based on the mobilities of neighboring phases, the interface maintains distinct potentials at opposing sides. This is more pronounced for cases with strong asymmetry of mobilities. Thus, it becomes difficult to obtain continuity of the potential at the interface. The distinction in potentials becomes more prominent if the interface is moving at a sufficiently fast speed or if the width is too large [39]. A schematic of the jump of potentials is given in Fig. 3.4a. An estimation of this jump was given in Ref. [42] as

$$u_1 - u_2 = A l v \left[ 1 - \frac{M_1}{M_2} \right], \quad (3.7)$$

where  $u_1$  and  $u_2$  are the values of the potentials of two neighboring phases at their sides of the interface.  $A$  is a parameter related to the bulk values of the potential.  $l$  is interface width and  $v$  is interface velocity.  $M_1$  and  $M_2$  are the mobilities of the two neighboring phases. Eq. (3.7) shows that the jump of the potential vanishes if the diffusion properties of the neighboring phases are equal. It also shows that the jump becomes more significant at relatively high interface velocity and width.

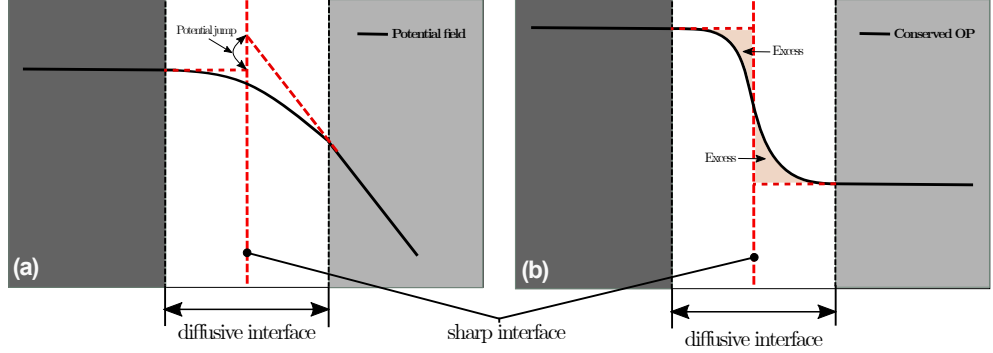


Figure 3.4: Schematics of (a) Jump of potentials across the interface in phase-field models with asymmetric diffusion, (b) Interface stretching effect showing the excess of conserved quantities along the arclength of the interface.

## Modification of conservation laws

### Interface stretching

The interface stretching effect at the interface appears as a modification of the conservation law of mass/energy in phase-field models with asymmetric diffusion. As obtained by Almgren [41], this modification appears in the conservation law as

$$v(u_1 - u_2) = -M_1 \nabla u|_1 + M_2 \nabla u|_2 + \underbrace{\Delta H k_{\text{int}} l}_{\text{Int. stretching}} v, \quad (3.8)$$

where  $u_1$  and  $u_2$  represent the bulk values of conserved quantities like concentration, mass, or internal energy in two neighboring phases.  $\nabla u|_1$  and  $\nabla u|_2$  are the spatial gradients of  $u$  at the corresponding sides of the interface.  $k_{\text{int}}$  is interface curvature. It can be noted that the interface stretching effect in Eq. (3.8) scales with interface velocity ( $v$ ) and width ( $l$ ).  $\Delta H$  in Eq. (3.8) arises if the arclength of one side of the diffusive interface is somewhat longer than the arclength on the other side. As illustrated in Fig. 3.4b, if the excess of the integral of  $u$  along the arclength of one side of the interface is not equivalent to the excess of the integral at the other side, it creates an extra source of  $u$  at the interface. In mathematical terms, if  $u$  is interpolated as  $u = u_1 h(\phi) + u_2 (1 - h(\phi))$  where  $h(\phi)$  is an interpolation function with  $h(\phi) = 1$  in phase 1 and  $h(\phi) = 0$  in phase 2, then  $\Delta H$  can be formulated as

$$\Delta H = \int_0^{+\infty} [u_1 - u(\phi(r))] dr - \int_{-\infty}^0 [u(\phi(r)) - u_2] dr. \quad (3.9)$$

It can simply be deduced from Eq. (3.9) that the elimination of  $\Delta H$  is linked to the careful consideration of the choice of interpolation function  $h(\phi)$ .

### Surface diffusion

The modification of the conservation law by surface diffusion effect arises because diffusion at the interface in phase-field models occurs not just across the interface (normal direction) but also along the interface (tangential direction) which is different from most conventional sharp-interface models where diffusion is only considered in one direction [39]. The implication of this effect can be explained by considering the schematics in Fig. 3.5 for two neighboring phases and also examining the fluxes at the normal and tangential directions independently.

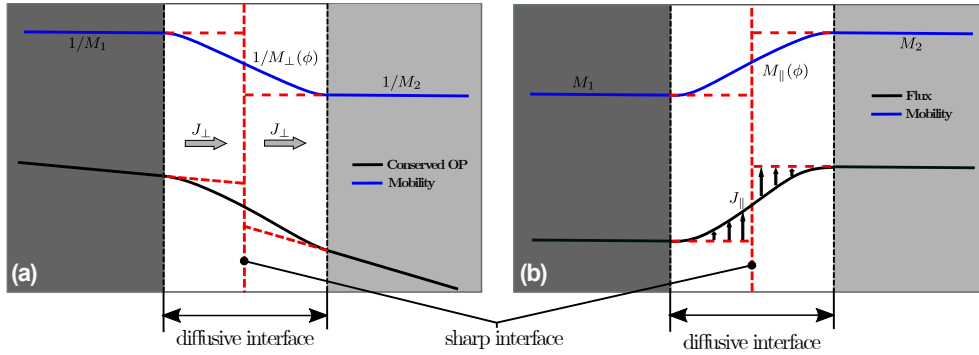


Figure 3.5: Schematics of (a) Normal flux across the diffusive interface in phase-field models and corresponding mobility function (b) Tangential flux along the diffusive interface in phase-field models and corresponding mobility function.

For a conserved quantity  $u$ , the flux can simply be written as  $\mathbf{J} = -M(\phi)\nabla u$  in a typical phase-field model where  $M(\phi)$  is mobility which is dependent on the phase-field  $\phi$  thereby interpolates based on the mobilities of neighboring phases. If a flux  $J_\perp$  flowing in the normal direction is considered, then the solution of the quantity  $u$  for a diffusive interface is

$$u(r) = u(0) - \int_{-\infty}^{+\infty} \frac{J_\perp}{M_\perp(\phi)} dr, \quad (3.10)$$

where  $u(0)$  is the value of quantity  $u$  at  $r = 0$  and  $M_\perp(\phi)$  is the mobility defined for the normal direction. On the other hand, for a sharp interface, the solution of the quantity

$u$  on both sides of the interface (phase 1 and phase 2) would be

$$u_1(r) = u(0) - \int_{-\infty}^0 \frac{J_{\perp}}{M_1} dr, \quad u_2(r) = u(0) - \int_0^{+\infty} \frac{J_{\perp}}{M_2} dr, \quad (3.11)$$

where  $M_1$  and  $M_2$  are the mobilities of phase 1 and phase 2 respectively. The difference between both solutions can be obtained as

$$\delta u = J_{\perp} \int_{-\infty}^0 \left[ \frac{1}{M_{\perp}(\phi)} - \frac{1}{M_1} \right] dr + J_{\perp} \int_0^{+\infty} \left[ \frac{1}{M_{\perp}(\phi)} - \frac{1}{M_2} \right] dr. \quad (3.12)$$

The excess  $\delta u$  can be eliminated if the two terms on the right-hand side (R.H.S) of Eq. (3.12) are equal. This is only possible if the interpolation of  $M_{\perp}(\phi)$  is taken as

$$\frac{1}{M_{\perp}(\phi)} = \frac{h(\phi)}{M_1} + \frac{1-h(\phi)}{M_2}, \quad (3.13)$$

where  $h(\phi)$  is an interpolation function;  $h(\phi) = 1$  in phase 1 and  $h(\phi) = 0$  in phase 2.

In another vein, if the flux  $J_{\parallel}$  flowing in the tangential direction is considered, then it can simply be obtained for a diffusive interface as

$$J_{\parallel} = \int_{-\infty}^{+\infty} M_{\parallel}(\phi) \nabla u dr, \quad (3.14)$$

where  $M_{\parallel}(\phi)$  is the mobility defined for the tangential direction. For a sharp interface,  $J_{\parallel}$  would be obtained as a contribution from both phases such that

$$J_{\parallel} = \int_{-\infty}^0 M_1 \nabla u dr + \int_0^{+\infty} M_2 \nabla u dr. \quad (3.15)$$

The excess of the flux obtained using a diffusive interface and a sharp interface can be expressed as

$$\delta J = \int_{-\infty}^0 [M_{\parallel}(\phi) - M_1] \nabla u dr + \int_0^{+\infty} [M_{\parallel}(\phi) - M_2] \nabla u dr. \quad (3.16)$$

The excess  $\delta J$  can be interpreted as excess flux flowing along the interface and can be eliminated if the interpolation of  $M_{\parallel}(\phi)$  is taken as

$$M_{\parallel}(\phi) = M_1 h(\phi) + M_2 (1 - h(\phi)). \quad (3.17)$$

---

Eqs. (3.13) and (3.17) show that consideration of the fluxes in normal and tangential directions in phase-field models with asymmetric diffusion imposes excess terms that can only be eliminated by specific choices of the interpolations of the mobility. The interpolations in Eqs. (3.13) and (3.17) are mutually exclusive therefore eliminating one excess term with a specific interpolation scheme means the other excess remains nonzero [77].

### 3.1.5 Quantitative phase-field models

The interface effects described above generally scale with interface velocity and interface width. This implies that at a sufficiently low velocity or for an interface with negligible interface width, these effects become trivial [39]. However, as discussed before, numerical simulations using phase-field models require larger interface widths for efficient simulations. Thus, the elimination of these effects is required for quantitative modeling and simulations, or else these effects will be artificially magnified with increased interface width. Different approaches have been employed to obtain quantitative phase-field models: non-variational and variational approaches. Both approaches will be explicitly discussed in the following discussions.

#### Non-variational

The first successful approach to obtain a quantitative phase-field model for asymmetric diffusion was introduced by Karma [47] for the solidification process in a dilute binary alloy. This approach requires altering the variational structure of the kinetic equations in phase-field models in order to ensure the elimination of the interface effects. In particular, Karma [47] introduced the so-called *antitrapping current* into the diffusion equation of the model. The fundamental idea of this current is to create an "anti" flux that corrects the spurious trapping effect at the diffusive interface [39]. Furthermore, the assumption of negligible diffusivity in the solid phase allows the interface stretching and surface diffusion effects to be eliminated by careful choice of specific interpolation functions. Generally, for a phase-field model with a non-conserved OP  $\phi$  and a conserved OP  $u$ , the *antitrapping current* is defined as

$$\mathbf{J}_A = -la(\phi, u)\dot{\phi}\frac{\nabla\phi}{|\nabla\phi|}, \quad (3.18)$$

where  $l$  is interface width and  $a(\phi, u)$  is an antitrapping function that is obtained based on the condition of vanishing potential jump [78]. It is also important to note that the current  $\mathbf{J}_A$  is directed in the normal direction via  $\nabla\phi/|\nabla\phi|$  and as well proportional to  $\dot{\phi}$

which represents the rate at which the interface moves [78]. The addition of  $\mathbf{J}_A$  into the diffusion equation adds a source of flux that is subtracted from the conventional gradient flux. It can be seen as a theoretical "trick" to ensure that the phase-field model is correctly mapped to the associated sharp-interface model [39].

While the quantitative phase-field model with the antitrapping current was developed for a case of negligible diffusivity in one of the neighboring phases, antitrapping currents for the case of arbitrarily different diffusivities in neighboring phases have been also proposed for isothermal [48] and non-isothermal [44] scenarios. Thereby, a new parameter relating interface velocity and diffusion flux was further introduced to ensure full elimination of all interface artifacts. Moreover, quantitative phase-field models with antitrapping current have found extensive usage in different cases ranging from two-phase growth [79] to multi-component systems [80] and multiphase systems [81].

### Variational

It is important to note that the *antitrapping current* explained in the section above is purely phenomenological. The antitrapping flux was derived and added to the diffusion equation to specifically eliminate the abnormal trapping effect. However, modifying a variationally derived diffusion equation by prescribed antitrapping current does not necessarily guarantee the variational nature of the model, which is, however, important for the thermodynamics soundness of phase-field models. Therefore there have been efforts to develop variational formulations of quantitative phase-field models.

Using phenomenological linear relations, variational formulation of quantitative phase-field models have been developed by considering kinetic cross-coupling between the conserved diffusion fields and the nonconserved OPs (*non-diagonal model*) [49, 50, 51, 52]. These cross-couplings are based on the basic principles of non-equilibrium thermodynamics. For example, for a phase-field model with a non-conserved OP  $\phi$  and a conserved OP  $u$ , dissipative minimization of the total free energy  $F$  can be guaranteed by taking the following relations:

$$\begin{bmatrix} \mathbf{J} \\ \dot{\phi} \end{bmatrix} = \begin{bmatrix} M_{uu} & M_{u\phi} \\ M_{\phi u} & M_{\phi\phi} \end{bmatrix} \begin{bmatrix} \nabla \frac{\delta F}{\delta u} \\ \frac{\delta F}{\delta \phi} \end{bmatrix}. \quad (3.19)$$

$M_{uu}$  and  $M_{\phi\phi}$  are the diagonal mobilities that are generally considered in phase-field models. The non-diagonal mobilities  $M_{u\phi}$  and  $M_{\phi u}$  are mostly neglected in conventional phase-field models, whereas their consideration is the principal feature of the *non-diagonal model*. The consideration of the non-diagonal mobilities engenders cross-coupling kinetic terms that are formulated in a similar fashion (Onsager's symmetry)

in the time evolution equations of the model. Furthermore, the parameters of the coupling terms can be explicitly formulated in terms of model parameters by considering relevant thermodynamic relations between the phase-field model and the sharp-interface counterpart. The cross-coupling term obtained in the diffusion flux equation can be likened to the *antitrapping current* introduced by Karma [47]. This term has been noted to enable the elimination of interface effects [52, 82]. Moreover, the *non-diagonal model* has been employed to investigate quantitative phase-field simulations of dendritic growth [83] and to examine quantitative simulations of eutectic and eutectoid transformations [84] in which the necessity of the cross-coupling terms was substantiated in both instances.

By separately considering the thermodynamic quantities of two opposing phases and then treating the interface as a mixture of the phases (*two-phase variational approach*), Ohno et al. [38, 40] presented quantitative variational phase-field models for binary alloy solidification with two-sided diffusion. In the two-phase formulation, the diffusion field mixture laws are ensured at the interface as constraints implemented by the Lagrange multiplier approach, and the flux fields of each single-phase field are formulated variationally. For instance, for a phase-field model with a non-conserved OP  $\phi$  and a conserved OP  $u$ , quantity  $u$  can be defined for two phases as a mixture of  $u_1$  and  $u_2$  where  $u_i$  is the value of  $u$  in phase  $i$  as

$$u = u_1 h(\phi) + u_2 (1 - h(\phi)). \quad (3.20)$$

In the *two-phase variational approach*, the mixture law in Eq. (3.20) is taken as a constraint in the total free energy  $F$  such that

$$\bar{F} = F + \int_{\Omega} \Lambda [u - u_1 h(\phi) + u_2 (1 - h(\phi))] \, d\Omega, \quad (3.21)$$

where  $\Lambda$  is a Lagrange multiplier. The emergence of the Lagrange multiplier in the thermodynamic potential formulation would further give rise to cross-coupling terms in the model time evolution equations which serve to eliminate the abnormal interface effects. Though the two-phase variational approach is promising for the study of quantitative validity, the variational nature of the model is only implicitly implemented through variationally formulated single-phase fluxes. The variational behavior of the final model after inserting the Lagrange multiplier still needs to be examined. Moreover, due to the assumptions of negligible temperature jump or chemical potential jump across the diffuse interface, the models in Refs. [38, 40] are applicable mostly for slow solidification processes.

---

## 3.2 Phase-field Simulation of Sintering

Different phase-field models have been developed for modeling and simulation of sintering processes. In practice, these models have been largely employed to describe the complex microstructure evolution and the intricate multi-physics in sintering processes. Hereby presented are the various categories of these models which are generally differentiated based on the formulation of their thermodynamic potentials.

### 3.2.1 Conventional model

Phase-field models for sintering were initially proposed by Kazaryan et al. [26] and Wang [27] considering an isothermal scenario. In the model, the microstructure evolution during the sintering process is described by a combination of a conserved OP  $\rho$ , and a set of non-conserved OPs  $\eta_i$ . The OP  $\rho$  represents the mass density i.e. the distribution of the solid substance and pores/atmosphere. On the other hand, the OPs  $\eta_i$  depict the structural orientation of the individual solid grains, thus the total number of  $\eta_i$  is equivalent to the number of the solid grains in the microstructure. Moreover, the total free energy is formulated in terms of  $\rho$  and  $\eta_i$  as

$$F(\rho, \{\eta_i\}) = \int_{\Omega} \left[ f(\rho, \{\eta_i\}) + \frac{\beta_{\rho}}{2} |\nabla \rho|^2 + \frac{\beta_{\eta}}{2} \sum_i |\nabla \eta_i|^2 \right] d\Omega, \quad (3.22)$$

where  $f(\rho, \{\eta_i\})$  is the local free energy that exhibits minimal at the possible coexisting bulk regions such as the pores/atmosphere, and solid grains at different orientations.  $\beta_{\rho}$  and  $\beta_{\eta}$  are gradient energy coefficients associated with  $\rho$  and  $\eta_i$ . The function  $f(\rho, \{\eta_i\})$  as well as the gradient terms in Eq. (3.22) can be directly linked to material properties such as surface and grain boundary energies [27, 29]. Kinetic equations for  $\rho$  and  $\eta_i$  are respectively described by the Cahn-Hilliard and Allen-Cahn equations;

$$\frac{\partial \rho}{\partial t} = \nabla \cdot \left( M \nabla \frac{\delta F}{\delta \rho} \right), \quad (3.23)$$

and

$$\frac{\partial \eta_i}{\partial t} = -L \frac{\delta F}{\delta \eta_i}. \quad (3.24)$$

$M$  is the diffusion mobility and  $L$  is the mobility that characterizes the movement of the grain boundaries. To take into account the different mass transfer mechanisms in



sintering, mobility  $M$  is formulated to consider different diffusion paths such that

$$M = p_{ss}(\rho)M_{ss} + p_{at}(\rho)M_{at} + p_{sf}(\rho)M_{sf} + p_{gb}(\eta_i)M_{gb}, \quad (3.25)$$

where  $M_{ss}$ ,  $M_{at}$ ,  $M_{sf}$  and  $M_{gb}$  present the diffusion through solid, atmosphere/pores, surface, and grain boundary respectively.  $p_{rg}$  is an interpolation that is equal to 1 in the corresponding region "rg" [27, 29]. The phase-field solutions of  $\rho$  and  $\eta_i$  in Eqs. (3.23) and (3.24) apparently describe the microstructural evolution during the isothermal sintering process. The driving force of the microstructural evolution is the reduction of the total free energy  $F$  via mass transfer and structural relaxation. Thereby the surface and grain boundary energies are reduced via a collection of volume diffusion, surface diffusion, grain boundary diffusion, and grain boundary migration [26, 27].

The isothermal sintering model described above has been used for studying two-particle necking and coalescence [28, 29, 30, 31, 32, 85, 86] and densification of porous microstructure [29, 33], and in simulating the overall microstructure evolution of the particle aggregation [87] or particle stack [27, 88]. Also, rigid-body motions were incorporated within the model [27, 31, 86, 88] via modification of the kinetics equations (Eqs. (3.23) and (3.24)).

### 3.2.2 Grand-potential model

Another line of phase-field models developed for the sintering process was derived based on the grand potential concept [34, 89, 90]. Similar to the conventional model, a set of OPs  $\eta_i$  are introduced to distinguish the individual solid grains. However, an additional OP  $\phi$  is used to represent the pores and external void region. Moreover, a conserved OP  $c$  is used to indicate the concentration of vacancies. The thermodynamic potential is the grand potential and it is defined for the whole system as [90]

$$\Psi(\phi, \eta_i, \mu) = \int_{\Omega} [\omega_b(\phi, \eta_i) + \omega_{gr}(\nabla\eta_i, \nabla\phi) + h_s(\phi)\omega_s(\mu) + h_v(\phi)\omega_v(\mu)] d\Omega, \quad (3.26)$$

where  $\omega_s$  and  $\omega_v$  are respectively the grand potential densities for the solid and void regions where both are functions of the chemical potential of the vacancies  $\mu$ .  $\omega_b$  is the bulk contribution of the grand potential density and it is formulated as a multi-well potential exhibiting minima at the bulk values of the OPs.  $\omega_{gr}$  is the gradient contribution.  $h_s$  and  $h_v$  are interpolation functions associated with the corresponding regions. Also,  $\omega_s$  and  $\omega_v$  are respectively formulated as

$$\omega_s = f_s - c_s \frac{\mu}{V_a}, \quad (3.27)$$

$$\omega_v = f_v - c_v \frac{\mu}{V_a}, \quad (3.28)$$

where  $f_s$  and  $f_v$  are the Helmholtz free energies densities of the solid and void regions respectively.  $c_s$  and  $c_v$  are the concentration of the vacancies in the associated region and are related to OP  $c$  as;  $c = h_s c_s + h_v c_v$ . The chemical potential of the vacancies is defined as  $\mu = V_a \frac{\partial f_s}{\partial c_s} = V_a \frac{\partial f_v}{\partial c_v}$ .  $V_a$  is the atomic volume of the material. The kinetic equations for OPs  $\phi$  and  $\eta_i$  are defined using modified Allen-Cahn equations;

$$\frac{\partial \phi}{\partial t} = -L_s \frac{\delta \Psi}{\delta \phi}, \quad (3.29)$$

$$\frac{\partial \eta_i}{\partial t} = -L_v \frac{\delta \Psi}{\delta \eta_i}. \quad (3.30)$$

$L_s$  and  $L_v$  are mobility parameters. Moreover, based on the grand-potential concept, the kinetic equation for  $\mu$  is defined such that

$$\frac{\partial \mu}{\partial t} = \frac{1}{\chi} \left[ \nabla \cdot (\chi \mathbf{D} \nabla \mu) - \frac{1}{V_a} \frac{\partial c}{\partial \phi} \frac{\partial \phi}{\partial t} \right], \quad (3.31)$$

where  $\mathbf{D}$  is the diffusivity tensor and  $\chi$  is susceptibility. In particular,  $\chi$  can be defined as  $\chi = \frac{1}{V_a} \frac{\partial c}{\partial \mu}$  which degenerates into the well-known thermodynamic factor in the bulk regions;  $\chi = \frac{1}{V_a^2} \frac{\partial^2 f_s}{\partial c_s^2} = \frac{1}{V_a^2} \frac{\partial^2 f_v}{\partial c_v^2}$  [89].

The major advantage of the grand-potential model stems from the projection of the thermodynamic energies in the grand potential space rather than the energies itself [34]. The usage of the grand potential densities decouples the interface energy and thickness from the chemical free energy of the system [90]. Thereby the bulk and interface parameters can be adjusted independently. Since the equilibrium interface thickness is not dependent on the thermodynamic driving force, the mesh/grid resolution can be conveniently chosen allowing simulations of large-scale domains. In practice, the grand-potential sintering model has been employed to simulate the sintering process of a huge number of particles [34, 90, 91]. For example, 3D sintering simulations of 24,897  $\text{Al}_2\text{O}_3$  grains based on the grand-potential sintering model were demonstrated in Ref. [34].

### 3.2.3 Entropy-based non-isothermal model

To simulate the sintering process under a highly heterogeneous thermal environment, the phase-field sintering model coupled with transient heat transfer is needed. Thus, a

variational non-isothermal phase-field sintering model was proposed in Refs. [36, 6]. The model incorporates the OPs  $\rho$  and  $\eta_i$  from the conventional model [27] in addition to the internal energy density contribution  $e$ . Therefore, the entropy of the system is defined as

$$S(e, \rho, \{\eta_i\}) = \int_{\Omega} \left[ s(e, \rho, \{\eta_i\}) - \frac{\kappa_{\rho}}{2} |\nabla \rho|^2 - \frac{\kappa_{\eta}}{2} \sum_i |\nabla \eta_i|^2 \right] d\Omega,$$

with

$$s = \Phi_{\text{ht}}(\rho, \{\eta_i\}) s_{\text{ht}} + s_{\text{cf}}(\rho, \{\eta_i\}), \quad (3.32)$$

where  $s$  is the local entropy density which receives contributions from thermal ( $s_{\text{ht}}$ ) and configurational ( $s_{\text{cf}}$ ) distributions.  $\Phi_{\text{ht}}$  is an interpolating function that interpolates the heat contributions from different regions.  $\kappa_{\rho}$  and  $\kappa_{\eta}$  are the gradient energy coefficients associated with  $\rho$  and  $\{\eta_i\}$  respectively. Moreover, the entropy  $S$  can be related to the free energy  $F$  through Legendre transformation such that

$$F(T, \rho, \{\eta_i\}) = \int_{\Omega} \left[ f(T, \rho, \{\eta_i\}) + \frac{T\kappa_{\rho}}{2} |\nabla \rho|^2 + \frac{T\kappa_{\eta}}{2} \sum_i |\nabla \eta_i|^2 \right] d\Omega, \quad (3.33)$$

with

$$f(T, \rho, \{\eta_i\}) = \Phi_{\text{ht}} f_{\text{ht}}(T) + e_{\text{pt}} - T s_{\text{cf}}, \quad (3.34)$$

where  $f_{\text{ht}}$  represents the thermal contribution to the free energy.  $e_{\text{pt}}$  accounts for the spatial distribution of the internal energy proportional to  $\rho$  and  $\{\eta_i\}$ .  $T$  is the temperature. The kinetic equations for the OPs  $\rho$  and  $\{\eta_i\}$  are obtained based on non-equilibrium thermodynamics;

$$\frac{\partial \rho}{\partial t} = \nabla \cdot \left[ \mathbf{M} \nabla \frac{\delta F}{\delta \rho} + \frac{\delta F}{\delta \rho} \mathbf{M}_{\text{th}} \cdot \frac{\nabla T}{T} \right], \quad (3.35)$$

$$\frac{\partial \eta_i}{\partial t} = -L \frac{\delta F}{\delta \eta_i}. \quad (3.36)$$

$\mathbf{M}$  and  $\mathbf{M}_{\text{th}}$  are mobility tensors that are explicitly related to the diffusivity tensor and the transport heat of the material.  $L$  is a parameter related to the grain boundary mobility and grain boundary energy. Also, the heat transfer equation which is coupled with the microstructure evolution is obtained as

$$c_r \dot{T} + \frac{\partial e}{\partial \rho} \frac{\partial \rho}{\partial t} + \sum_i \frac{\partial e}{\partial \eta_i} \frac{\partial \eta_i}{\partial t} = \nabla \cdot [\mathbf{k} \cdot \nabla T], \quad (3.37)$$

where  $c_r$  is the specific heat capacity and  $\mathbf{k}$  is the thermal conductivity tensor.

---

The explicit consideration of temperature in the model presented above implies that the influence of both temperature-dependent and temperature-gradient-dependent effects such as Soret (thermophoresis), Dufour, and thermocapillary effects on sintering can be investigated. Thus, the model has been applied for simulations of the selective laser sintering on single-layer and multi-layer [37] powder beds, and for sintering under prescribed high-temperature gradient [6].

### 3.3 Finite-element Basics

The modeling of different physical phenomena is typically characterized by the use of partial differential equations (PDEs). Obtaining analytical or exact solutions for most of these PDEs is very intricate or for some, practically impossible. Thus numerical methods are often employed to obtain approximate solutions for the PDEs. One of the widely used numerical methods for obtaining these solutions is the finite element method (FEM). As illustrated in Fig. 3.6, the FEM discretizes a domain into subdomains called *finite elements*. These elements are interconnected at distinct points generally called *nodes*. The combination of the elements and nodes in the whole domain is called the *mesh*.

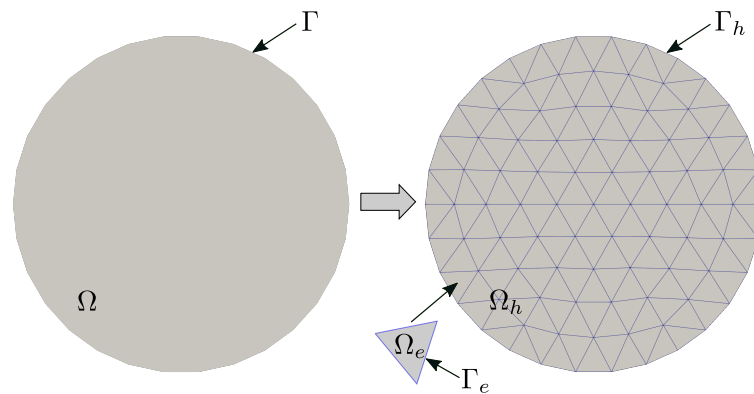


Figure 3.6: Schematic illustration of the finite element discretization of a 2D circular domain into subdomains of triangular elements.

To demonstrate the basic methodology of the FEM, a simple heat conduction equation

is considered,

$$c_r \dot{T} = k \nabla^2 T \quad \text{in } \Omega, \quad (3.38)$$

where  $\Omega$  is the domain,  $c_r$  is the specific heat, and  $T$  is the temperature field.  $k$  is the thermal conductivity and is assumed to be an arbitrary constant. In addition, the domain's boundary is defined as  $\Gamma = \partial\Omega$ , and corresponding boundary conditions (BCs) are applied on the different subsets of  $\Gamma$ , that is

$$T|_{\Gamma_D} = \bar{T}, \quad (3.39)$$

$$\nabla T|_{\Gamma_N} \cdot \hat{\mathbf{n}} = J, \quad (3.40)$$

with  $\Gamma = \Gamma_D \cup \Gamma_N$ . Eq. (3.39) is called the *Dirichlet* BC whereby a specified temperature  $\bar{T}$  is given along the boundary  $\Gamma_D$ . Eq. (3.40) is the *Neumann* BC which imposes a flux  $J$  on the boundary  $\Gamma_N$ . The PDE in Eq. (3.38) as well as the BCs defined above are typically referred to as the *strong form* of the heat conduction problem. In FEM, the *weak form* of the problem is needed to obtain approximate solutions. The weak form of Eq. (3.38) is obtained by multiplying both sides of the equation by a *test function*  $\psi$  and further integrating the result over the domain  $\Omega$  such that

$$\int_{\Omega} c_r \dot{T} \psi \, d\Omega - \int_{\Omega} k \nabla^2 T \psi \, d\Omega = 0. \quad (3.41)$$

Applying integration by parts on the second term of Eq. (3.41) yields

$$\int_{\Omega} c_r \dot{T} \psi \, d\Omega - \int_{\Omega} k \nabla \cdot (\psi \nabla T) \, d\Omega + \int_{\Omega} k \nabla \psi \nabla T \, d\Omega = 0. \quad (3.42)$$

Considering the Gauss/divergence theorem:  $\int_{\Omega} \nabla \cdot \mathbf{F} \, d\Omega = \int_{\Gamma} \mathbf{F} \cdot \hat{\mathbf{n}} \, d\Gamma$ , and also the BCs in Eqs. (3.39) and (3.40), Eq. (3.42) yields

$$\int_{\Omega} c_r \dot{T} \psi \, d\Omega - \int_{\Gamma_N} k \psi J \, d\Gamma + \int_{\Omega} k \nabla \psi \nabla T \, d\Omega = 0. \quad (3.43)$$

Eq. (3.43) is the weak form of the heat conduction problem and it contains the first derivatives of temperature. Compared to the strong form in Eq. (3.38) which contains second-order derivatives, it becomes apparent that the weak form is defined to reduce the intricacy of higher-order derivatives.

Based on FEM, the integral terms in Eq. (3.43) are defined as a sum over each finite element. The domain  $\Omega$  approximated as  $\Omega_h$  is defined as

$$\Omega \approx \Omega_h = \sum_e^{N_{el}} \Omega_e, \quad (3.44)$$

where  $\Omega_e$  is the domain of an element and  $N_{el}$  is the number of nodes associated with the element. Thus Eq. (3.43) can be written as

$$\sum_e^{N_{el}} \int_{\Omega_e} c_T \dot{T} \psi \, d\Omega - \sum_e^{N_{el}} \int_{\Gamma_{eN}} k \psi J \, d\Gamma + \sum_e^{N_{el}} \int_{\Omega_e} k \nabla \psi \nabla T \, d\Omega = 0. \quad (3.45)$$

The fields  $T$  and  $\psi$  need to be continuous in the domain  $\Omega$  to ensure zero values for the surface integrals between adjacent elements. Also, their first derivatives may be discontinuous in  $\Omega$ . Continuous functions whose first derivatives are discontinuous are generally referred to as  $C^0$  functions. On the other hand,  $C^1$  functions and their first derivatives are continuous.  $C^0$  functions are widely used in FEM and are defined based on the *isoparametric* formulation [92, 93]. Taking this into account, the numerical solution of  $T$  can be approximated as  $T_h$  following the Galerkin finite element method as

$$T \approx T_h = \sum_I^{N_{el}} T_I N_I(\xi), \quad (3.46)$$

where  $T_I$  are the nodal values of temperature,  $I$  is a node number,  $N_I$  is called the *shape function* for node  $I$  and  $\xi$  are natural coordinates. Shape functions like  $N_I$  generally have two major properties: they have a value of either 0 or 1 at a node and they sum up to 1;  $\sum_I^{N_{el}} N_I(\xi) = 1$ . Moreover,  $\psi$  can also be expressed as

$$\psi = \sum_I^{N_{el}} \psi_I N_I(\xi), \quad (3.47)$$

where  $\psi_I$  are arbitrary parameters. The gradients of  $T$  and  $\psi$  can also be defined as

$$\nabla T \approx \nabla T_h = \sum_I^{N_{el}} T_I \nabla N_I(\xi), \quad (3.48)$$

and

$$\nabla \psi = \sum_I^{N_{el}} \psi_I \nabla N_I(\xi). \quad (3.49)$$

To obtain  $\nabla T$  and  $\nabla \psi$ ,  $\nabla N_I$  is needed. It can be obtained using chain rule such that

$$\frac{\partial N_I}{\partial \mathbf{r}} = \mathbf{J}^{-1} \frac{\partial N_I}{\partial \xi}, \quad (3.50)$$

where  $\mathbf{J}$  is the Jacobian transformation between  $\mathbf{r}$  and  $\boldsymbol{\xi}$ . In addition,  $\dot{T}$  can be expressed as

$$\dot{T} = \sum_I^{N_{el}} \dot{T}_I N_I(\boldsymbol{\xi}). \quad (3.51)$$

Taking into account all the aforementioned, the weak form in Eq. (3.45) can be written as

$$\sum_e^{N_{el}} \psi_I (M_{IJ} \dot{T}_J + K_{IJ} T_J - F_I) = 0, \quad (3.52)$$

where

$$M_{IJ} = \int_{\Omega_e} c_r N_I N_J \, d\Omega, \quad (3.53)$$

$$K_{IJ} = \int_{\Omega_e} k \nabla N_I \nabla N_J \, d\Omega, \quad (3.54)$$

and

$$F_I = \int_{\Gamma_{eN}} k N_I J \, d\Gamma. \quad (3.55)$$

Noting that  $\psi_I$  is an arbitrary parameter, Eq. (3.52) can be written in a matrix notation such that

$$\mathbf{M}\dot{\mathbf{T}} + \mathbf{K}\mathbf{T} - \mathbf{F} = 0. \quad (3.56)$$

In the practical usage of the FEM, Eq. (3.56) is taken as the residual of the heat conduction equation, and a solution is obtained when this residual is equal to zero. Therefore obtaining a solution would then require computing the arrays  $\mathbf{M}$ ,  $\mathbf{K}$ , and  $\mathbf{F}$  in each finite element.





---

## 4 Variational Quantitative Phase-field Model of Non-isothermal Sintering: Model Development and Asymptotic Analysis

---

As presented in Chapter 3, variational phase-field models have been instrumental in describing the intricate pore-structure evolution and the complex multi-physics in non-isothermal sintering processes. However, as one of the diffuse-interface approaches, the models employ a finite interface width in representing the transient microstructure. They have to be projected asymptotically onto their corresponding sharp-interface models to obtain quantitative simulations of microstructure evolution. An early approach introduced for this projection is an asymptotic analysis at the *sharp-interface limit* where diffusive interface width is taken to be very small [74, 75, 76]. However, setting the interface width to extremely small values implies a huge computational cost. Another approach is the so-called *thin-interface limit* introduced by Karma and Rappel [45, 46]. In this approach, diffusive interface width is taken to be much larger than the realistic value but also smaller compared to any physical length on the microstructural scale. Based on the *thin-interface limit*, Karma and Rappel obtained a quantitative phase-field model for solidification assuming equal diffusivity in neighboring phases (*symmetric diffusion*).

An extension of the *thin-interface limit* to unequal diffusivity in neighboring phases (*asymmetric diffusion*) showed the existence of several abnormal interface effects such as the trapping effects in variational phase-field models [41]. These effects scale with interface velocity and width, and thus are artificially magnified when the diffusive interface width is taken to be much larger than realistic values. One common procedure for eliminating these interface effects is by prescribing a correction term called *antitrapping current* in the diffusion equation [47]. This term is proportional to the interface velocity

---

and is a source of flux necessary to correct the trapping effect at the interface. While the quantitative model based on the *antitrapping current* was initially developed with negligible diffusivity in one of the neighboring phases, it has been extended for the cases with arbitrarily different diffusivities in neighboring phases [44, 48]. However, it is important to note that simply introducing the *antitrapping current* into phase-field models is not sufficient to eliminate all the abnormal interface effects. Moreover, the term can be seen as a theoretical idea to ensure that phase-field models are correctly mapped to the associated sharp-interface model. It is purely phenomenological and is not derived based on variational formulations. Thus, non-equilibrium thermodynamics is not satisfied [40].

While there have been efforts to develop variational quantitative phase-field models for solidification processes [38, 49], there is no related work addressing the interfaces in non-isothermal sintering. Most sintering systems demonstrate *asymmetric diffusion* with the surfaces between the solid phase and surrounding vapor regions exhibiting strong asymmetries of mass and thermal properties. For example, in the sintering of yttria-stabilized zirconia, the ratio of thermal diffusivity in the vapor to the one in the solid is in the order of  $10^{-2}$  [6]. Moreover, in comparison to non-isothermal solidification models with non-conserved order parameters, additional challenges can be expected due to the conserved order parameters that describe the interfaces in non-isothermal sintering models. The major aim of this chapter is to introduce the variational formulation of a quantitative phase-field model applicable to non-isothermal sintering processes. The model is derived based on phenomenological linear relations as an extension of the non-diagonal phase-field model [49, 50, 51, 52].

The formulations of the variational quantitative model are first derived in Section 4.1 where the entropy and free energy functionals as well as the time evolution equations are explicitly given. In Section 4.2, the sharp-interface description of a typical free surface in a non-isothermal sintering process is first introduced. Moreover, an asymptotic analysis linking the parameters of the quantitative model and that of the sharp-interface equations is demonstrated. The importance of this linkage and the specific choice of *anisotropic interpolations* of diffusion mobilities, as regards the elimination of abnormal interface effects, is also discussed. Finally, a detailed analysis of an additional abnormal interface effect; the deviation of the conserved order parameter across the free surfaces is demonstrated in Section 4.3.

---

## 4.1 Model Formulations

In this section, a framework for deriving a non-isothermal variational quantitative phase-field sintering model is presented. Generally, the underlying physical processes involved in non-isothermal sintering can be classified as but not limited to (a) the mass/heat transport, including diffusion through sorts of paths (volume, surface, and grain boundaries) and mass flows (viscous or fluid flow); (b) the structural relaxation, including the rigid-body motions of powders and interface (mostly the grain boundaries) migration. All these underlying interactive processes collectively lead to two significant phenomena: one is the densification (eliminating the pores), in which the total surface energy should be reduced; the other is the grain coarsening, in which the total grain-boundary energy should decrease [10, 11, 94]. Consequently, in this model, a conserved OP  $\rho$  denoting the solid density fraction is used to indicate the solid region ( $\rho = 1$ ) and the atmosphere/pores region ( $\rho = 0$ ) while a series of non-conserved OPs  $\{\eta_i\}$  are used to represent the different grain orientations of the solid grains.

### 4.1.1 Entropy and free energy functionals

Considering a non-isothermal scenario, the entropy functional  $S$  for a subdomain  $\Omega$  within the sintering system can be defined as

$$S(e, \rho, \{\eta_i\}) = \int_{\Omega} \left[ s(e, \rho, \{\eta_i\}) - \frac{\kappa_{\rho}}{2} |\nabla \rho|^2 - \frac{\kappa_{\eta}}{2} \sum_i |\nabla \eta_i|^2 \right] d\Omega,$$

with

$$s = \frac{1 + h(\rho)}{2} s_{ss}(e_{ss}) + \frac{1 - h(\rho)}{2} s_{at}(e_{at}) + s_{cf}(\rho, \{\eta_i\}), \quad (4.1)$$

where  $s$  is the local entropy density,  $e$  is the internal energy density while  $\kappa_{\rho}$  and  $\kappa_{\eta}$  are the gradient energy coefficients associated with  $\rho$  and  $\{\eta_i\}$  respectively.  $s_{ss}$  is the solid phase bulk entropy density and is dependent on the internal energy density of the solid  $e_{ss}$ . The bulk entropy density of the atmosphere  $s_{at}$  is dependent on the internal energy density of the atmosphere  $e_{at}$ .  $h(\rho) = 2\rho - 1$  is an interpolation function. The configurational entropy  $s_{cf}$  is related to the spatial distribution of entropy density proportional to  $\rho$  and  $\{\eta_i\}$ . It is formulated in the form of a Landau-type polynomial

similar to the one given by Ref. [27] as

$$s_{\text{cf}}(\rho, \{\eta_i\}) = \underline{C}_{\text{cf}} [\rho^2(1-\rho)^2] + \underline{D}_{\text{cf}} \left[ \rho^2 + 6(1-\rho) \sum_i \eta_i^2 - 4(2-\rho) \sum_i \eta_i^3 + 3 \left( \sum_i \eta_i^2 \right)^2 \right], \quad (4.2)$$

where  $\underline{C}_{\text{cf}}$  and  $\underline{D}_{\text{cf}}$  are constants. The multi-well potential in Eq. (4.2) can be seen to exhibit minimal at various regions such as: atmosphere ( $\rho = 0, \{\eta_1 = 0, \dots, \eta_n = 0\}$ ), and solid grains at different orientations ( $\rho = 1, \{\eta_1 = 1, \dots, \eta_n = 0\}$ ),  $\dots$ , ( $\rho = 1, \{\eta_1 = 0, \dots, \eta_n = 1\}$ ). One advantage of this potential form is that its constant parameters can be directly linked to material properties [29].

Assuming  $e$  can be expressed as

$$e = \frac{1+h(\rho)}{2} e_{\text{ss}} + \frac{1-h(\rho)}{2} e_{\text{at}} + e_{\text{pt}}(\rho, \{\eta_i\}), \quad (4.3)$$

where  $e_{\text{pt}}$  accounts for the spatial distribution of the internal energy proportional to  $\rho$  and  $\{\eta_i\}$  and is also formulated similarly to  $s_{\text{cf}}$  as

$$e_{\text{pt}}(\rho, \{\eta_i\}) = \underline{C}_{\text{pt}} [\rho^2(1-\rho)^2] + \underline{D}_{\text{pt}} \left[ \rho^2 + 6(1-\rho) \sum_i \eta_i^2 - 4(2-\rho) \sum_i \eta_i^3 + 3 \left( \sum_i \eta_i^2 \right)^2 \right], \quad (4.4)$$

where  $\underline{C}_{\text{pt}}$  and  $\underline{D}_{\text{pt}}$  are constants.

Following Legendre transformation, the free energy functional  $F$  can be obtained as

$$F(T, \rho, \{\eta_i\}) = \int_{\Omega} \left[ f(T, \rho, \{\eta_i\}) + \frac{T\kappa_{\rho}}{2} |\nabla\rho|^2 + \frac{T\kappa_{\eta}}{2} \sum_i |\nabla\eta_i|^2 \right] d\Omega, \quad (4.5)$$

with

$$f(T, \rho, \{\eta_i\}) = \frac{1+h(\rho)}{2} f_{\text{ss}}(T) + \frac{1-h(\rho)}{2} f_{\text{at}}(T) + e_{\text{pt}} - T s_{\text{cf}}, \quad (4.6)$$

where  $f_{\text{ss}}$  and  $f_{\text{at}}$  are the free energy densities of the solid phase and the atmosphere, respectively.  $T$  is the temperature. Substituting Eqs. (4.2) and (4.4) into Eq. (4.6), I

obtain

$$f(T, \rho, \{\eta_i\}) = \frac{1+h(\rho)}{2} f_{ss}(T) + \frac{1-h(\rho)}{2} f_{at}(T) + \underline{C} [\rho^2(1-\rho)^2] + \underline{D} \left[ \rho^2 + 6(1-\rho) \sum_i \eta_i^2 - 4(2-\rho) \sum_i \eta_i^3 + 3 \left( \sum_i \eta_i^2 \right)^2 \right], \quad (4.7)$$

with

$$\underline{C} = \underline{C}_{pt} - T \underline{C}_{cf},$$

$$\underline{D} = \underline{D}_{pt} - T \underline{D}_{cf}.$$

#### 4.1.2 Kinetic equations

Considering that  $\rho$  and  $e$  are conserved OPs, they satisfy mass and energy conservation laws respectively:

$$\dot{\rho} = -\nabla \cdot \mathbf{J}_\rho, \quad (4.8)$$

$$\dot{e} = -\nabla \cdot \mathbf{J}_e. \quad (4.9)$$

$\mathbf{J}_\rho$  is the mass diffusion flux and  $\mathbf{J}_e$  is the energy flux.

Following the work in Ref. [6], the non-negative entropy production  $\sigma$  in the subdomain can be formulated as

$$\sigma = \int_{\Omega} \left[ \mathbf{J}_\rho \cdot \nabla \frac{\delta S}{\delta \rho} + \mathbf{J}_e \cdot \nabla \frac{\delta S}{\delta e} + \sum_i \dot{\eta}_i \frac{\delta S}{\delta \eta_i} \right] d\Omega, \quad (4.10)$$

where  $\nabla(\delta S/\delta \rho)$  is the driving force conjugated to  $\mathbf{J}_\rho$ ,  $\nabla(\delta S/\delta e)$  is the driving force conjugated to  $\mathbf{J}_e$  and  $\delta S/\delta \eta_i$  is the driving force conjugated to  $\dot{\eta}_i$ . In the view of the *phenomenological linear laws* of non-equilibrium thermodynamics and also ensuring non-negative production of the entropy, the relationships between the fluxes, the non-conserved OPs time evolution equations, and their driving forces can be defined as

$$\begin{bmatrix} \mathbf{J}_\rho \\ \mathbf{J}_e \\ \dot{\eta}_1 \\ \vdots \\ \dot{\eta}_n \end{bmatrix} = \begin{bmatrix} \mathbf{L}_{\rho\rho} & \mathbf{L}_{\rho e} & \mathbf{L}_{\rho\eta_1} & \cdots & \mathbf{L}_{\rho\eta_n} \\ \mathbf{L}_{e\rho} & \mathbf{L}_{ee} & \mathbf{L}_{e\eta_1} & \cdots & \mathbf{L}_{e\eta_n} \\ \mathbf{L}_{\eta_1\rho} & \mathbf{L}_{\eta_1 e} & \mathbf{L}_{\eta_1\eta_1} & \cdots & \mathbf{L}_{\eta_1\eta_n} \\ \vdots & \vdots & \vdots & \ddots & \vdots \\ \mathbf{L}_{\eta_n\rho} & \mathbf{L}_{\eta_n e} & \mathbf{L}_{\eta_n\eta_1} & \cdots & \mathbf{L}_{\eta_n\eta_n} \end{bmatrix} \begin{bmatrix} \nabla \frac{\delta S}{\delta \rho} \\ \nabla \frac{\delta S}{\delta e} \\ \frac{\delta S}{\delta \eta_1} \\ \vdots \\ \frac{\delta S}{\delta \eta_n} \end{bmatrix}, \quad (4.11)$$

where  $n$  represents the total number of grain orientations.  $\mathbf{L}_{\rho\rho}$ ,  $\mathbf{L}_{\rho e}$ ,  $\mathbf{L}_{e\rho}$  and  $\mathbf{L}_{ee}$  are positively defined rank 2 tensors and for  $i = 1, 2, \dots, n$ ,  $\mathbf{L}_{\rho\eta_i}$ ,  $\mathbf{L}_{e\eta_i}$ ,  $\mathbf{L}_{\eta_i\rho}$  and  $\mathbf{L}_{\eta_i e}$  are positively defined rank 1 tensors while  $\mathbf{L}_{\eta_i\eta_i}$  is a positively defined rank 0 tensor.

Diagonal terms  $\mathbf{L}_{\rho\rho}$  and  $\mathbf{L}_{ee}$  are the diffusional mobilities of mass and energy diffusion respectively. Mobility term associated with the grain orientations,  $\mathbf{L}_{\eta_i\eta_i}$  is simply a scalar function and is thereafter taken as  $L_{\eta_i}$  where I assume isotropic condition taking it to be the same regardless of  $i$ . The non-diagonal terms in the Onsager matrix in Eq. (4.11) represent cross-couplings between the various OPs. Based on the Onsager reciprocal relations, we have  $\mathbf{L}_{\rho e} = \mathbf{L}_{e\rho}$ ,  $\mathbf{L}_{\rho\eta_i} = \mathbf{L}_{\eta_i\rho}$  and  $\mathbf{L}_{e\eta_i} = \mathbf{L}_{\eta_i e}$ . The cross-coupling between the different grain orientations is not considered, resulting in a similar  $\dot{\eta}_i$  formulation for all  $i$ . Hence I consider only one  $\dot{\eta}_i$  whose formulation is representative for all  $i$ . The quantities  $\mathbf{L}_{\rho e}$  and  $\mathbf{L}_{e\rho}$  are associated with the mass flux due to temperature gradient (thermophoresis effect) and with the energy flux due to chemical potential gradient (Dufour effect), respectively. A detailed examination of these effects is given in Ref. [6]. The terms associated with  $\mathbf{L}_{\rho e}$  and  $\mathbf{L}_{e\rho}$  in the fluxes formulations are tentatively dropped. Thus, the time evolution equations can then be written as

$$\dot{\rho} = \nabla \cdot \left[ \mathbf{L}_{\rho\rho} \cdot \nabla \left( \frac{\mu}{T} \right) \right] + \nabla \cdot \left[ \frac{1}{T} \sum_i \mathbf{L}_{\rho\eta_i} \frac{\delta F}{\delta \eta_i} \right], \quad (4.12a)$$

$$\dot{e} = \nabla \cdot \left[ \mathbf{L}_{ee} \cdot \frac{\nabla T}{T^2} \right] + \nabla \cdot \left[ \frac{1}{T} \sum_i \mathbf{L}_{e\eta_i} \frac{\delta F}{\delta \eta_i} \right], \quad (4.12b)$$

$$\dot{\eta}_i = -\mathbf{L}_{\eta_i\rho} \cdot \nabla \left( \frac{\mu}{T} \right) - \mathbf{L}_{\eta_i e} \cdot \frac{\nabla T}{T^2} - L_{\eta_i} \frac{1}{T} \frac{\delta F}{\delta \eta_i}, \quad (4.12c)$$

with

$$\frac{\mu}{T} = -\frac{\delta S}{\delta \rho}, \quad \frac{1}{T} \frac{\delta F}{\delta \eta_i} = -\frac{\delta S}{\delta \eta_i}, \quad \frac{1}{T} = \frac{\delta S}{\delta e},$$

where  $\mu = \delta F / \delta \rho$  is defined as the chemical potential.

Formulations expressed in Eqs. (4.11) and (4.12) present the fluxes and time evolution equations of the associated OPs in terms of the driving forces. However, for consistency with similar models [50, 52] as well as ease of relating the model to the sharp-interface counterpart as will be discussed later, I reformulate the phenomenological linear relations employing the linear relations of the driving forces in terms of the fluxes and time evolution equations such that

$$-\nabla \left( \frac{\mu}{T} \right) = \mathbf{L}_{\rho\rho}^{-1} \cdot \mathbf{J}_{\rho} + \mathbf{L}_{\rho\eta_i}^{-1} \sum_i \dot{\eta}_i, \quad (4.13a)$$

$$-\frac{\nabla T}{T^2} = \mathbf{L}_{ee}^{-1} \cdot \mathbf{J}_e + \mathbf{L}_{e\eta_i}^{-1} \sum_i \dot{\eta}_i, \quad (4.13b)$$

$$-\frac{1}{T} \frac{\delta F}{\delta \eta_i} = \mathbf{L}_{\rho\eta_i}^{-1} \cdot \mathbf{J}_\rho + \mathbf{L}_{\eta_i,e}^{-1} \cdot \mathbf{J}_e + L_{\eta_i}^{-1} \dot{\eta}_i. \quad (4.13c)$$

Since the variations of mass density and internal energy are found across free surfaces of the solid grains, the cross-coupling terms  $\mathbf{L}_{\rho\eta_i}^{-1} = \mathbf{L}_{\eta_i,\rho}^{-1}$  and  $\mathbf{L}_{e\eta_i}^{-1} = \mathbf{L}_{\eta_i,e}^{-1}$  should be defined such that they are only evaluated at the free surfaces. Also, the non-equilibrium effects associated with these cross-terms scale with the diffuse interface width  $l$ . Accordingly, following Refs. [49, 50, 52], I propose the following formulations:

$$\mathbf{L}_{\rho\eta_i}^{-1} = \mathbf{L}_{\eta_i,\rho}^{-1} = M_1(\rho) l \nabla \rho, \quad (4.14a)$$

$$\mathbf{L}_{e\eta_i}^{-1} = \mathbf{L}_{\eta_i,e}^{-1} = M_2(\rho) l \nabla \rho. \quad (4.14b)$$

$M_1$  and  $M_2$  are scalar functions used to parametrize the associated cross-coupling terms.  $l \nabla \rho$  is a vector normal to the free surfaces and has a magnitude of 1 at the center of the free surfaces assuming the parameter  $\alpha$  used to adjust the definition of  $l$  in Ref. [95] equals 2 [36]. Substituting Eq. (4.13) into (4.10) and taking into account the aforementioned, the entropy production in the subdomain can be obtained as

$$\begin{aligned} \sigma = \int_{\Omega} & \left[ \mathbf{L}_{\rho\rho}^{-1} \cdot \mathbf{J}_\rho \cdot \mathbf{J}_\rho + \mathbf{L}_{ee}^{-1} \cdot \mathbf{J}_e \cdot \mathbf{J}_e + L_{\eta_i}^{-1} \left( \sum_i \dot{\eta}_i \right)^2 \right. \\ & \left. + 2l \nabla \rho \sum_i \dot{\eta}_i \cdot (M_1 \mathbf{J}_\rho + M_2 \mathbf{J}_e) \right] d\Omega. \end{aligned}$$

Furthermore, time evolution equations can be obtained as

$$\dot{\rho} = \nabla \cdot \left[ \mathbf{L}_{\rho\rho} \cdot \left( \nabla \left( \frac{\mu}{T} \right) + M_1 l \nabla \rho \sum_i \dot{\eta}_i \right) \right], \quad (4.15a)$$

$$c_T \dot{T} + \frac{\partial e}{\partial \rho} \dot{\rho} + \sum_i \frac{\partial e}{\partial \eta_i} \dot{\eta}_i = \nabla \cdot \left[ \mathbf{L}_{ee} \cdot \left( \frac{\nabla T}{T^2} + M_2 l \nabla \rho \sum_i \dot{\eta}_i \right) \right], \quad (4.15b)$$

$$\hat{L}_{\eta_i}^{-1} \dot{\eta}_i = \kappa_{\eta_i} \nabla^2 \eta_i - \frac{1}{T} \frac{\partial f}{\partial \eta_i} + l \nabla \rho \cdot \left[ M_1 \mathbf{L}_{\rho\rho} \cdot \nabla \left( \frac{\mu}{T} \right) + M_2 \mathbf{L}_{ee} \cdot \frac{\nabla T}{T^2} \right], \quad (4.15c)$$

with

$$\hat{L}_{\eta_i}^{-1} = L_{\eta_i}^{-1} - [M_1^2 l^2 \nabla \rho \cdot \mathbf{L}_{\rho\rho} + M_2^2 l^2 \nabla \rho \cdot \mathbf{L}_{ee}] \cdot \nabla \rho. \quad (4.16)$$

---

Hereby  $c_r = \frac{1+h(\rho)}{2}c_{ss} + \frac{1-h(\rho)}{2}c_{at}$  is the relative specific heat, where  $c_{ss} = \partial e_{ss}/\partial T$  and  $c_{at} = \partial e_{at}/\partial T$  are the volumetric specific heat of solid and atmosphere, respectively.

Comparing the heat transfer equation (Eq. (4.15b)) to that of conventional non-isothermal quantitative phase-field model [44], the second term on the right-hand-side (RHS) can be likened to the *thermal antitrapping current* related to the elimination of thermal trapping (associated with temperature jump) at the free surfaces. Similarly, the second term on the RHS of Eq. (4.15a) represents a form of antitrapping current valued only at the free surfaces. Similar to solutal antitrapping current [43, 47] associated with solute trapping due to the jump of chemical potential, this term can be termed as the *mass antitrapping current*. The last two terms on the RHS of the grain orientation time evolution equations (Eq. (4.15c)) represent cross-coupling terms associated with mass and energy diffusion across the free surfaces, respectively. These terms alongside the antitrapping terms are absent in time evolution equations of conventional non-isothermal phase-field sintering models but are vital in eliminating abnormal interface effects such as the trapping effects at the free surfaces of the solid phase. Moreover, considering no variation of solid density and thermal properties across the grain boundaries, Eq. (4.15c) has no cross-coupling terms and simply takes the form of the Allen-Cahn equation at the grain boundaries.

## 4.2 Thin-interface Asymptotics

The major objective of this section is to derive the relationships between the parameters of the quantitative model and those of a corresponding sharp-interface model at the thin-interface limit. The derivation of these relationships is essential so that the phase-field parameters can be formulated such that the quantitative phase-field model reproduces its associated sharp-interface conditions. Therefore, a sharp-interface description of non-isothermal sintering is first introduced followed by the analysis of the quantitative model at the *thin-interface limit*. Lastly, explicit formulations of the model parameters as well as anisotropic interpolation of diffusion mobilities are presented and discussed.

### 4.2.1 Sharp-interface description of non-isothermal sintering

As described in Section 4.1, the introduced cross-coupling terms in the quantitative model are only significant at the free surfaces of the solid region. Hence, subsequent derivations, and analysis are limited to the free surfaces. Considering a simple nonisothermal system



consisting of a sharp free surface between a solid grain and the atmosphere/pore region, the following set of sharp-interface equations can be described in the bulk regions:

$$\frac{\partial \rho}{\partial t} = \nabla \cdot (M_{\text{rg}} \nabla \mu), \quad (4.17)$$

$$c_{\text{rg}} \frac{\partial T}{\partial t} = \nabla \cdot (k_{\text{rg}} \nabla T). \quad (4.18)$$

For a bulk region rg ("ss" for solid and "at" for atmosphere),  $M_{\text{rg}}$ ,  $c_{\text{rg}}$ , and  $k_{\text{rg}}$  represent the region's effective mass mobility coefficient, volumetric specific heat, and effective thermal conductivity respectively.  $\rho$  here adopts the physical meaning of the normalized density of the solid. Eqs. (4.17) and (4.18) describe mass and heat transfer in the bulk regions. For the bulk atmosphere region in particular,  $M_{\text{at}}$  describes the effective mobility considering mass transfer mechanisms notably evaporation and condensation. Hence, the driving force  $\nabla \mu$  for mass transfer in the atmosphere takes into account vapor pressure differences due to local curvature [10, 11]. Similarly,  $k_{\text{at}}$  describes effective thermal conductivity taking into account convection and radiation.

Furthermore, *energy conservation* condition at the free surface can be described as

$$v e_{\text{ss}} + k_{\text{ss}} \nabla T|_{\text{ss}} \cdot \mathbf{n}_{\text{sf}} = v e_{\text{at}} + k_{\text{at}} \nabla T|_{\text{at}} \cdot \mathbf{n}_{\text{sf}} = J_T, \quad (4.19)$$

where  $v$  is the velocity of the migrating free surface.  $\nabla T|_{\text{ss}}$  and  $\nabla T|_{\text{at}}$  are the spatial gradients of the temperature at the solid and atmosphere sides of the free surface respectively.  $\mathbf{n}_{\text{sf}}$  is the unit vector normal to the free surface.  $J_T$  is the normal heat flux flowing through the free surface. Similarly, explicit formulation of *mass conservation* at the free surface is given as

$$v(\rho_{\text{ss}} - \rho_{\text{at}}) = -M_{\text{ss}} \nabla \mu|_{\text{ss}} \cdot \mathbf{n}_{\text{sf}} + M_{\text{at}} \nabla \mu|_{\text{at}} \cdot \mathbf{n}_{\text{sf}} + M_{\text{sf}} \nabla_{\text{sf}}^2 \mu, \quad (4.20)$$

where  $\rho_{\text{ss}}$  and  $\rho_{\text{at}}$  are the bulk densities in the solid and atmosphere and  $\nabla \mu|_{\text{ss}}$  and  $\nabla \mu|_{\text{at}}$  are the spatial gradients of the chemical potential at the solid and atmosphere sides of the free surface respectively.  $M_{\text{sf}}$  represents surface diffusion mobility.  $\nabla_{\text{sf}}^2$  is surface Laplacian. The last term in Eq. (4.20) describes surface diffusion typical to sharp-interface description of mass transfer in sintering [30]. Moreover,  $v$  can be defined as

$$v = v_s + v_b, \quad (4.21)$$

where  $v_s$  and  $v_b$  are the velocities contributed by surface diffusion and bulk/volume diffusion respectively and can be expressed in terms of their corresponding mass fluxes;

$$v_s = -V_m \nabla_{\text{sf}} \cdot \mathbf{J}_{\text{sf}}, \quad v_b = -V_m \mathbf{J}_b \cdot \mathbf{n}_{\text{sf}}. \quad (4.22)$$

$V_m$  is the molar volume and  $\nabla_{\text{sf}}$  is the surface gradient.  $\mathbf{J}_{\text{sf}}$  is the mass flux along the free surface associated with surface gradient of the free surface curvature  $k_{\text{sf}}$ ;  $\mathbf{J}_{\text{sf}} \propto \nabla_{\text{sf}} k_{\text{sf}}$ .  $\mathbf{J}_b$  is mass flux from the solid bulk to the free surface associated with the gradient of the chemical potential in the solid bulk grains  $\mu_{\text{ss}}$ ;  $\mathbf{J}_b \propto \nabla \mu_{\text{ss}}$ , [30, 96].

In addition, the chemical potential and temperature at the free surface obey the following relations:

$$\mu|_{\text{ss}} = \mu|_{\text{at}}, \quad (4.23a)$$

$$T|_{\text{ss}} - T|_{\text{at}} = J_T R_s. \quad (4.23b)$$

$\mu|_{\text{ss}}$  and  $\mu|_{\text{at}}$  represent chemical potentials at the solid and atmosphere sides of the free surface, respectively.  $T|_{\text{ss}}$  and  $T|_{\text{at}}$  represent the temperatures at the solid and atmosphere sides of the free surface, respectively.  $R_s$  represents Kapitza-type thermal resistance. In this work, I assume negligible  $R_s$ , thereby Eq. (4.23a) and Eq. (4.23b) indicate imposed *zero chemical potential* and *zero temperature jump* at the free surface.

Moreover, I infer that any jump in the chemical potential  $\delta\mu$  across the free surface is conjugated to  $v$  and also that any temperature jump  $\delta T$  across the free surface is conjugated to  $J_T$ . The kinetic boundary conditions can then be expressed in the framework of phenomenological linear relations as [97, 98]

$$\delta\mu = \mathcal{A}v + \mathcal{B}J_T, \quad (4.24)$$

$$\delta T = \mathcal{B}v + \mathcal{C}J_T, \quad (4.25)$$

where  $\mathcal{A}$ ,  $\mathcal{B}$  and  $\mathcal{C}$  are kinetic coefficients of the positive-definite Onsager matrix. Entropy production at the free surface  $\sigma_s$  can be formulated as

$$\sigma_s = v\delta\mu + J_T\delta T. \quad (4.26)$$

Substituting Eqs. (4.24) and (4.25) into (4.26) yields

$$\sigma_s = \mathcal{A}v^2 + \mathcal{C}J_T^2 + 2\mathcal{B}vJ_T. \quad (4.27)$$

## 4.2.2 Thin-interface limit of model

In this subsection, still considering a simple free surface between a solid grain and the atmosphere, I establish the relationships between the parameters  $\mathcal{A}$ ,  $\mathcal{B}$  and  $\mathcal{C}$  in Eqs. (4.24) and (4.25) and the quantitative model parameters. This is done to obtain explicit formulations of the model parameters that would guarantee that the

aforementioned sharp-interface conditions are obtained in the quantitative phase-field model. The analysis and derivations are done at the *thin-interface limit* following the reduction procedure presented in Ref. [50].

Considering a simple 1D system with the free surface centered at  $x = 0$  (shown in Fig. 4.1a),  $\rho$  and  $\eta$  vary from a semi-finite solid region ( $-\infty$ ) to a semi-finite atmosphere region ( $+\infty$ ). For simplicity, notation  $(\cdot)'$  is adopted to represent the derivative w.r.t. the spatial coordinate  $x$ . It is worth noting that I consider the profile of  $\rho$  between  $\rho_{ss}$  in the substance and  $\rho_{at}$  in the pore/atmosphere region. This is done partly to obtain consistency with Eq. (4.20) in the sharp-interface model and also to take into account the slight deviation of  $\rho$  from the ideal bulk values. The origin and the thermodynamic outcome of these deviated bulk values of  $\rho$  are explicitly examined and discussed in Section 4.3.

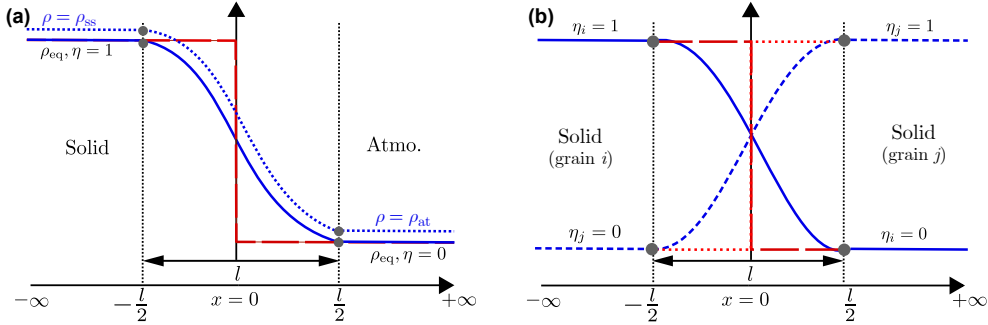


Figure 4.1: (a) Asymptotic schematic across a free surface; blue solid line represents phase-field profile at equilibrium and red large-dashed line represents sharp-interface profile; blue dotted line shows the profile of  $\rho$  with slightly deviated values; (b) Asymptotic schematic across a grain boundary; blue solid and dashed lines represent phase-field profiles and red large-dashed and dotted lines represent sharp-interface profiles.

According to the phase-field method, the entropy production (Eq. (4.15)) for the system considered can be formulated as

$$\begin{aligned} \sigma = & \int_{-\infty}^{-l/2} \left[ \frac{J_\rho^2(x)}{L_{pp}^{ss}} + \frac{J_e^2(x)}{L_{ee}^{ss}} \right] dx + \int_{l/2}^{\infty} \left[ \frac{J_\rho^2(x)}{L_{pp}^{at}} + \frac{J_e^2(x)}{L_{ee}^{at}} \right] dx \\ & + \int_{-l/2}^{l/2} \left[ \frac{J_\rho^2(x)}{L_{pp}} + \frac{J_e^2(x)}{L_{ee}} + L_{\eta, sf}^{-1} \dot{\eta}^2 + 2l\rho'(x)\dot{\eta}(M_1 J_\rho(x) + M_2 J_e(x)) \right] dx, \end{aligned} \quad (4.28)$$

where  $L_{\rho\rho}^{ss} = L_{\rho\rho}(\rho = \rho_{ss})$  and  $L_{\rho\rho}^{at} = L_{\rho\rho}(\rho = \rho_{at})$  are the effective mass mobilities in the corresponding regions. Also,  $L_{ee}^{ss} = L_{ee}(\rho = \rho_{ss})$  and  $L_{ee}^{at} = L_{ee}(\rho = \rho_{at})$  are the effective energy mobilities in the corresponding regions.  $L_{\eta, sf}$  is mobility of  $\eta$  at the free surface. It can be noted that in the bulk regions ( $|x| > l/2$ ), only the fluxes  $J_\rho(x)$  and  $J_e(x)$  contribute to entropy production as  $\dot{\eta}$  and  $\rho'(x)$  both go to zero.

The entropy production of the system considered can be formulated within the sharp-interface description as

$$\int_{-\infty}^0 \left[ \frac{J_\rho^2(x)}{L_{\rho\rho}^{ss}} + \frac{J_e^2(x)}{L_{ee}^{ss}} \right] dx + \int_0^{\infty} \left[ \frac{J_\rho^2(x)}{L_{\rho\rho}^{at}} + \frac{J_e^2(x)}{L_{ee}^{at}} \right] dx + \sigma_s. \quad (4.29)$$

Comparing Eqs. (4.28) and (4.29), I obtain entropy production at the free surface within the phase-field model as

$$\begin{aligned} \sigma_s = & \int_{-l/2}^{l/2} \left[ \frac{J_\rho^2(x)}{L_{\rho\rho}} + \frac{J_e^2(x)}{L_{ee}} + L_{\eta, sf}^{-1} \dot{\eta}^2 + 2l\rho'(x)\dot{\eta} \left( M_1 J_\rho(x) + M_2 J_e(x) \right) \right] dx \\ & - \int_{-l/2}^0 \left[ \frac{J_{ss(\rho)}^2}{L_{\rho\rho}^{ss}} + \frac{J_{ss(e)}^2}{L_{ee}^{ss}} \right] dx - \int_0^{l/2} \left[ \frac{J_{at(\rho)}^2}{L_{\rho\rho}^{at}} + \frac{J_{at(e)}^2}{L_{ee}^{at}} \right] dx, \end{aligned} \quad (4.30)$$

where for a region rg (“ss” for solid and “at” for atmosphere),  $J_{rg(\rho)}$  and  $J_{rg(e)}$  represent the region’s bulk mass and energy fluxes respectively.

For the purpose of making direct relations between Eq. (4.30) and its sharp-interface counterpart, Eq. (4.27), I express  $J_\rho(x)$ ,  $J_e(x)$  and  $\dot{\eta}$  in terms of  $v$  and  $J_T$ . First, analysis is made considering only fluxes that are flowing through the free surface along  $x$  direction (i.e normal to the free surface) thereby I tentatively drop the contribution of the surface diffusion flux  $J_{sf}$  to  $v$  since it is tangential to the free surface. Second, a quasisteady approximation is employed which assumes large gradients of  $\rho$ ,  $e$ , and  $\eta$  across the free surface such that their time derivatives can be defined as

$$\dot{\rho} \approx -v\rho'(x), \quad \dot{e} \approx -ve'(x), \quad \dot{\eta} \approx -v\eta'(x). \quad (4.31)$$

Integrating both sides of the conservation laws,  $\dot{e} = -J_e'(x)$  and  $\dot{\rho} = -J_\rho'(x)$  after substituting Eq. (4.31) yields

$$\int_{J_{ss(\rho)}}^{J_{at(\rho)}} dJ_\rho = v \int_{\rho_{eq}^{at}}^{\rho_{eq}^{ss}} d\rho, \quad \int_{J_{ss(e)}}^{J_{at(e)}} dJ_e = v \int_{e_{eq}^{ss}}^{e_{eq}^{at}} de, \quad (4.32)$$

with the boundary values as

$$\begin{aligned} J_{ss(\rho)} &\approx v\rho_{\text{eq}}^{\text{ss}}, & J_{\text{at}(\rho)} &\approx v\rho_{\text{eq}}^{\text{at}}, \\ J_{ss(e)} &\approx ve_{\text{eq}}^{\text{ss}} - J_T, & J_{\text{at}(e)} &\approx ve_{\text{eq}}^{\text{at}} - J_T, \end{aligned} \quad (4.33)$$

where  $\rho_{\text{rg}}^{\text{eq}}$  and  $e_{\text{rg}}^{\text{at}}$  (rg = ss, at) are the equilibrium conserved OPs and internal energies, respectively. The integrals in Eq. (4.32) yield

$$J_e(x) \approx ve(x) - J_T, \quad J_\rho(x) \approx v\rho(x). \quad (4.34)$$

Furthermore, sigmoid formulations for the profiles of  $\rho(x)$  and  $\eta(x)$  are adopted,

$$\rho(x) = \frac{1}{2} \left[ (\rho_{\text{ss}} + \rho_{\text{at}}) + (\rho_{\text{ss}} - \rho_{\text{at}}) \tanh \frac{2x}{l} \right], \quad (4.35)$$

$$\eta(x) = \frac{1}{2} \left[ 1 + \tanh \left( \frac{2x}{l} \right) \right], \quad (4.36)$$

with the diffuse interface width  $l$ .

Taking into account all the aforementioned, I obtain  $\sigma_s$  to be

$$\begin{aligned} \sigma_s &= \int_{-l/2}^{l/2} \left[ \frac{(v\rho(x))^2}{L_{\rho\rho}} - \frac{(v\rho_{\text{ss}})^2}{2L_{\rho\rho}^{\text{ss}}} - \frac{(v\rho_{\text{at}})^2}{2L_{\rho\rho}^{\text{at}}} \right] dx \\ &+ \int_{-l/2}^{l/2} \left[ \frac{(ve(x) - J_T)^2}{L_{ee}} - \frac{(ve_{\text{ss}} - J_T)^2}{2L_{ee}^{\text{ss}}} - \frac{(ve_{\text{at}} - J_T)^2}{2L_{ee}^{\text{at}}} \right] dx \\ &- \int_{-l/2}^{l/2} 4l\rho'(x)\eta'(x)v \left[ M_1(v\rho(x)) + M_2(ve(x) - J_T) \right] dx \\ &+ \int_{-l/2}^{l/2} L_{\eta,\text{sf}}^{-1} v^2 (\eta'_{\text{eq}}(x))^2 dx. \end{aligned} \quad (4.37)$$

Moreover, it should be noted that the integration range of Eq. (4.37) can also be taken from  $-\infty$  and  $+\infty$  without  $\sigma_s$  changing. In this regard, the integration interval is extended from  $[-l/2, +l/2]$  to  $[-\infty, +\infty]$  in the following discussion.

Comparing Eqs. (4.27) and (4.37), I obtain

$$\begin{aligned}
\mathcal{A} = & \int_{-\infty}^{\infty} \left[ \frac{\rho^2(x)}{L_{\rho\rho}} - \frac{(\rho_{ss})^2}{2L_{\rho\rho}^{ss}} - \frac{(\rho_{at})^2}{2L_{\rho\rho}^{at}} \right] dx - 4 \int_{-\infty}^{\infty} M_1 l \rho'(x) \eta'(x) \rho(x) dx \\
& + \int_{-\infty}^{\infty} \left[ \frac{e^2(x)}{L_{ee}} - \frac{(e_{ss})^2}{2L_{ee}^{ss}} - \frac{(e_{at})^2}{2L_{ee}^{at}} \right] dx - 4 \int_{-\infty}^{\infty} M_2 l \rho'(x) \eta'(x) e(x) dx \\
& + \int_{-\infty}^{\infty} L_{\eta, sf}^{-1} [\eta'(x)]^2 dx,
\end{aligned} \tag{4.38}$$

$$\mathcal{B} = \int_{-\infty}^{\infty} 2M_2 l \rho'(x) \eta'(x) dx - \int_{-\infty}^{\infty} \left[ \frac{e(x)}{L_{ee}} - \frac{e_{ss}}{2L_{ee}^{ss}} - \frac{e_{at}}{2L_{ee}^{at}} \right] dx, \tag{4.39}$$

$$\mathcal{C} = \int_{-\infty}^{\infty} \left[ \frac{1}{L_{ee}} - \frac{1}{2L_{ee}^{ss}} - \frac{1}{2L_{ee}^{at}} \right] dx. \tag{4.40}$$

The explicit formulations of  $\mathcal{A}$ ,  $\mathcal{B}$ , and  $\mathcal{C}$  imply that the quantitative phase-field model parameters can be carefully tuned to obtain  $\mathcal{A} = 0$ ,  $\mathcal{B} = 0$  and  $\mathcal{C} = 0$  which in turn guarantees that the sharp-interface imposed  $\delta\mu = 0$  and  $\delta T = 0$  is obtained in the quantitative model for a free surface with velocity  $v$ , which has heat flux  $J_T$  flowing through it.

### 4.2.3 Anisotropic interpolations and eliminating potential jumps

Before the explicit formulations of  $\mathcal{A}$ ,  $\mathcal{B}$ , and  $\mathcal{C}$  that guarantees  $\delta\mu = 0$  and  $\delta T = 0$  are given, it is important to note that Almgren [41] has shown that conservation law reproduced by phase-field models with asymmetric mobilities can be altered by two effects, namely interface stretching and surface diffusion even if  $\delta\mu = \delta T = 0$  is guaranteed. These two effects have been explicitly discussed in Subsection 3.1.4. In the sintering system, interface stretching represents excess mass and internal energy along the arclength of the free surfaces of the solid phase [43] and these excesses can both be respectively eliminated if  $\int_{-\infty}^{\infty} dx[\rho - \rho_{ss}/2 - \rho_{at}/2] = 0$  and  $\int_{-\infty}^{\infty} dx[e - e_{ss}/2 - e_{at}/2] = 0$ . Taking  $\rho$  as defined in Eq. (4.35) ensures that the interface excess of  $\rho$  is eliminated. Also, the interface excess of  $e$  is eliminated if interpolation function  $h(\rho)$  is taken as an odd function. Furthermore, surface diffusion terms in mass and energy conservation laws can be respectively parameterized by the mobilities  $L_{\rho\rho}^{sf} = \int_{-\infty}^{\infty} dx[L_{\rho\rho}(\rho) - L_{\rho\rho}^{ss}/2 - L_{\rho\rho}^{at}/2]$  and  $L_{ee}^{sf} = \int_{-\infty}^{\infty} dx[L_{ee}(\rho) - L_{ee}^{ss}/2 - L_{ee}^{at}/2]$  [41, 52].

In order to make  $\delta T = 0$ , one needs to ensure that  $\mathcal{B} = C = 0$  (see Eq. (4.25)). Consequently,  $L_{ee}$  should be formulated such that it gives the bulk region energy mobilities at the corresponding regions, ensures  $C = 0$ , and also guarantees that the model reproduces the sharp-interface energy conservation law (Eq. (4.19)) where there is no surface diffusion effect (i.e.  $L_{ee}^{sf} = 0$ ). To achieve this, Almgren [41] proposed a mobility interpolation function which is a combination of odd functions with parameters adjusted relative to the bulk mobilities. This method is contended by Ohno et al. [40] as the mobility interpolation function produces a non-monotonic function and also contributes to a limited ratio of possible bulk mobilities. Nevertheless, it is vital to note that while simultaneous elimination of  $\delta T$  and surface diffusion effect somewhat put constraints on a scalar formulation of  $L_{ee}$ , the emergence of both effects is actually direction dependent [77].  $L_{ee}$  formulation constraint due to  $\delta T$  (Eq. (4.40)) emerges under the consideration of flux components normal to the free surfaces as seen in the analysis done in Subsection 4.2.2 while the integral associated with the surface diffusion effect modification of energy conservation emanates due to consideration of flux components in tangential direction to the free surfaces [77]. Therefore, ensuring  $C = 0$  and eliminating surface diffusion term in energy conservation equation are respectively pertinent only at the normal and tangential directions of the free surfaces. Considering all the aforementioned and also taking into account the physical context of the energy mobility, an anisotropic  $\mathbf{L}_{ee}$  is proposed for the full sintering description and also related to the anisotropic thermal conductivity, that is

$$\begin{aligned}\mathbf{L}_{ee} &= \left[ k_{\perp} \mathbf{N}_{sf} + k_{\parallel} \mathbf{T}_{sf} + k_{gb}^{\circ} \mathbf{T}_{gb} \right] T^2 \\ &= L_{ee}^{\perp} \mathbf{N}_{sf} + L_{ee}^{\parallel} \mathbf{T}_{sf} + L_{ee}^{gb} \mathbf{T}_{gb},\end{aligned}\quad (4.41)$$

with

$$k_{\perp} = \left[ \frac{1 + g(\rho)}{2k_{ss}} + \frac{1 - g(\rho)}{2k_{at}} \right]^{-1}, \quad (4.42)$$

$$k_{\parallel} = \frac{1 + g(\rho)}{2} k_{ss} + \frac{1 - g(\rho)}{2} k_{at}, \quad (4.43)$$

$$k_{gb}^{\circ} = 16 \sum_{i \neq j} \eta_i^2 \eta_j^2 k_{gb}, \quad (4.44)$$

and

$$\begin{aligned}\mathbf{N}_{sf} &= \mathbf{n}_{sf} \otimes \mathbf{n}_{sf}, \\ \mathbf{T}_{sf} &= \mathbf{I} - \mathbf{n}_{sf} \otimes \mathbf{n}_{sf}, \\ \mathbf{T}_{gb} &= \mathbf{I} - \mathbf{n}_{gb} \otimes \mathbf{n}_{gb}.\end{aligned}\quad (4.45)$$

In Eq. (4.41),  $L_{ee}^\perp$  is the energy mobility in the normal direction to the free surfaces defined to ensure  $C = 0$ ,  $L_{ee}^\parallel$  is the energy mobility in the tangential direction to the free surfaces formulated to ensure  $L_{ee}^{sf} = 0$  in the energy conservation law, and  $L_{ee}^{gb}$  represents the energy mobility in the grain boundary. Similarly,  $k_\perp$  and  $k_\parallel$  represent the thermal conductivities at the normal and tangential directions to the free surfaces respectively while  $k_{gb}$  represent the thermal conductivity in the grain boundary.  $k_{ss}$  and  $k_{at}$  are respectively the effective thermal conductivities in the solid phase and atmosphere region and  $k_{gb}$  is the effective thermal conductivity in the grain boundary. Surface and grain boundary normal vectors are calculated from the gradient of corresponding OPs, e.g.,  $\mathbf{n}_{sf} \equiv \nabla\rho/|\nabla\rho|$ .  $\mathbf{I}$  is the identity tensor and  $\otimes$  represents the dyadic product.  $g(\rho) = 2\rho - 1$  is an odd function that satisfies  $g(\rho = \rho_{ss}) = 1$  and  $g(\rho = \rho_{at}) = -1$ .

Noting that  $L_{ee}^\perp = k_\perp T^2$  and therefore substituting Eq. (4.42) into (4.39), I obtain

$$\mathcal{B} = 2\chi M_2 - \frac{\beta l}{2T^2} \left( \frac{1}{2k_{ss}} - \frac{1}{2k_{at}} \right), \quad (4.46)$$

with

$$\chi = l \int_{-\infty}^{\infty} \rho'(x) \eta'(x) dx = 2(\rho_{ss} - \rho_{at})/3, \quad (4.47)$$

$$\beta = \frac{e_{ht}}{l} \int_{-\infty}^{\infty} [h(\rho)g(\rho) - 1] dx = -e_{ht}(\rho_{ss} - \rho_{at})^2, \quad (4.48)$$

where  $e_{ht} = e_{ss} - e_{at}$ . The functions defined in Eqs. (4.35) and (4.36) are adopted to calculate integrals in Eqs. (4.47) and (4.48).

Therefore, to obtain  $\mathcal{B} = 0$ , I take

$$M_2 = \frac{\beta l}{4\chi T^2} \left( \frac{1}{2k_{ss}} - \frac{1}{2k_{at}} \right). \quad (4.49)$$

Following [6, 29, 99] whereby the different mass diffusion routes in the sintering process i.e bulk/volume diffusion, surface diffusion along the free surfaces, and grain boundary diffusion are taken into account, an anisotropic  $\mathbf{L}_{\rho\rho}$  is proposed and related to the anisotropic diffusivity as

$$\begin{aligned} \mathbf{L}_{\rho\rho} &= [D_v \mathbf{I} + D_{sf}^\circ \mathbf{T}_{sf} + D_{gb}^\circ \mathbf{T}_{gb}] / s_v \\ &= L_{\rho\rho}^v \mathbf{I} + L_{\rho\rho}^{sf} \mathbf{T}_{sf} + L_{\rho\rho}^{gb} \mathbf{T}_{gb}, \end{aligned} \quad (4.50)$$



with

$$D_v = \left[ \frac{1 + g(\rho)}{2D_{ss}} + \frac{1 - g(\rho)}{2D_{at}} \right]^{-1}, \quad (4.51)$$

$$D_{sf}^\circ = 16\rho^2(1 - \rho)^2 D_{sf}, \quad (4.52)$$

$$D_{gb}^\circ = 16 \sum_{i \neq j} \eta_i^2 \eta_j^2 D_{gb}, \quad (4.53)$$

and the volumetric entropy as

$$s_v = \frac{1}{T} \frac{\partial \mu}{\partial \rho}, \quad (4.54)$$

where the linear approximation is sometimes taken as  $s_v \approx \mathcal{R}/V_m$  with the ideal gas constant  $\mathcal{R}$  and molar volume  $V_m$  [6, 29, 100]. In Eq. (4.50),  $L_{\rho\rho}^v$  is the mass mobility in the normal direction to the free surfaces associated with the bulk/volume diffusion in solid phase and atmosphere region,  $L_{\rho\rho}^{sf}$  is the mass mobility in the tangential direction to the free surfaces associated with mass transport via surface diffusion. Consideration of  $L_{\rho\rho}^{sf}$  ensures that the model reproduces the sharp-interface mass conservation law Eq. (4.20) where surface diffusion is considered.  $L_{\rho\rho}^{gb}$  represent the mass mobility in the grain boundary. Similarly,  $D_v$  represents the volume diffusivity, which is interpolated by the effective diffusivities in the solid phase ( $D_{ss}$ ) and atmosphere region ( $D_{at}$ ).  $D_{sf}$  and  $D_{gb}$  are the effective diffusivities in the free surfaces and grain boundary, respectively.

Moreover, I propose  $M_1$  to have a similar formulation as  $M_2$  in Eq. (4.49) as

$$M_1 = -\frac{3ls_v}{16} \left( \frac{A_{ss}}{2D_{ss}} - \frac{A_{at}}{2D_{at}} \right), \quad (4.55)$$

with

$$A_{ss} = \rho_{ss} + \rho_{at}, \quad (4.56)$$

$$A_{at} = 3A_{ss} - 2. \quad (4.57)$$

Substituting Eqs. (4.49) and (4.55) into (4.38), I obtain

$$\mathcal{A} = \frac{\psi L_{\eta, sf}^{-1}}{l} - \frac{l(\rho_{ss} - \rho_{at})^2}{4} \left[ \frac{s_v A_{ss}}{D_{ss}} + \frac{\zeta}{T^2} \left( \frac{1}{2k_{ss}} + \frac{1}{2k_{at}} \right) \right], \quad (4.58)$$

with

$$\zeta = \frac{e_{ht}^2}{l} \int_{-\infty}^{\infty} [1 - h^2(\rho)] dx = e_{ht}^2, \quad (4.59)$$

and

$$\psi = l \int_{-\infty}^{\infty} (\eta'(x))^2 dx = 2/3, \quad (4.60)$$

also taking into account:

$$\int_{-\infty}^{\infty} [(\rho(x))^2 + g(\rho)(\rho(x))^2 - 1] dx = -\frac{3l}{4} A_{ss} (\rho_{ss} - \rho_{at})^2, \quad (4.61)$$

$$\int_{-\infty}^{\infty} [(\rho(x))^2 [1 - g(\rho)]] dx = \frac{l}{4} A_{at} (\rho_{ss} - \rho_{at})^2. \quad (4.62)$$

The functions defined in Eq. (4.36) and (4.35) are again adopted to calculate integrals in Eq. (4.60) and Eqs. (4.59) - (4.62).

Therefore, in order to ensure  $\mathcal{A} = 0$ , I take

$$L_{\eta, sf}^{-1} = \frac{l^2 (\rho_{ss} - \rho_{at})^2}{4\psi} \left[ \frac{s_v A_{ss}}{D_{ss}} + \frac{\zeta}{T^2} \left( \frac{1}{2k_{ss}} + \frac{1}{2k_{at}} \right) \right]. \quad (4.63)$$

The mobility  $L_{\eta, gb}^{-1}$  of  $\{\eta_i\}$  can be obtained from the physical grain boundary mobility  $G_{gb}^{\text{eff}}$  and grain boundary energy  $\gamma_{gb}$  as [6, 101]

$$L_{\eta, gb}^{-1} = \frac{\kappa_{\eta}}{G_{gb}^{\text{eff}} \gamma_{gb}}. \quad (4.64)$$

Recalling Eqs. (4.15c) and (4.16), it is worth mentioning that this mobility is defined under the driving force represented by entropy, which should be distinguished from the original formulation in Ref. [101] as here  $\kappa_{\eta}$  adopts the dimension of the entropy per length. Accordingly,  $L_{\eta}^{-1}$  as regards the full sintering description can be formulated as

$$L_{\eta}^{-1} = 16\rho^2 (1 - \rho)^2 L_{\eta, sf}^{-1} + L_{\eta, gb}^{-1}. \quad (4.65)$$

Recalling the anisotropic definitions of  $\mathbf{L}_{ee}$  and  $\mathbf{L}_{\rho\rho}$  in Eqs. (4.41) and (4.50), calculation of  $\hat{L}_{\eta}^{-1}$  in Eq. (4.16) can be further simplified as

$$\hat{L}_{\eta}^{-1} = L_{\eta}^{-1} - l^2 |\nabla\rho|^2 [M_1^2 L_{\rho\rho}^v + M_2^2 L_{ee}^{\perp}], \quad (4.66)$$

as  $L_{ee}^{\perp}$  and  $L_{\rho\rho}^v$  are respectively one of the eigen-values of  $\mathbf{L}_{ee}$  and  $\mathbf{L}_{\rho\rho}$ , corresponding to the eigen-direction of  $\mathbf{n}_{sf}$  ( $\mathbf{n}_{sf} \equiv \nabla\rho/|\nabla\rho$ ).

---

Here, I note that  $M_1$  and  $M_2$  are derived based on the constant postulate, i.e.,  $M_1$  and  $M_2$  are spatio-temporal independent constants for a sintering system with known mass diffusivities and thermal conductivities of substance and atmosphere as well as given diffuse interface width, since the spatio-temporal dependency of all OP-related terms (Eqs. (4.47)-(4.48), (4.60), and (4.59)-(4.62)) vanish after integral. More importantly, the quantitative phase-field model degenerates to the conventional one when the system has no differences in mass diffusivity and thermal conductivity between solid and atmosphere. In that sense, when  $D_{ss} = D_{at}$ ,  $M_1 = 0$  and also when  $k_{ss} = k_{at}$ ,  $M_2 = 0$ , demonstrating that the antitrapping terms in Eqs. (4.15a) and (4.15b) and cross-coupling term in Eq. (4.15c) reduce to zero.

Moreover, it is worth noting that variational quantitative phase-field models generally do not demonstrate high numerical accuracy [38, 40, 46]. Correct mapping of the variational model onto the associated sharp-interface equations only guarantees its quantitative validity and not its numerical efficiency needed for realistic utilization [40]. Therefore, a nonvariational form of the model might be best suited for practicability. The nonvariational form can be simply developed via modification of model parameters and functions while ensuring that the thin-interface asymptotic remains consistent.

### 4.3 Analysis of Order Parameter Deviation

In addition to the well-known abnormal interface effects in variational phase-field models, there exists an additional effect peculiar to Cahn-Hilliard (CH) dynamics. This effect involves the deviation of the associated CH conserved OP in the bulk regions due to the usage of finite interface width combined with comparable curvature radius [102, 103]. This implies that the conserved OP  $\rho$  that differentiates the solid and atmosphere regions deviates from ideal values of 1 and 0 i.e.  $\rho_{ss} \neq 1$  and  $\rho_{at} \neq 0$  in the bulk regions due to the dynamics of Eq. (4.15a). The major aim of this section is to give a theoretical analysis of this dynamic and associated deviation of  $\rho$ . First, I give a description of associated governing equations considering a simple free surface between a solid grain and atmosphere region. Afterward, a mathematical analysis of the deviation of  $\rho$  is done showing a detailed derivation of the magnitude of this deviation as well as its dependencies.

### 4.3.1 General considerations

For this analysis, I consider an isothermal system consisting of a free surface between a solid grain and the atmosphere/pore region. Heat transfer is not considered solely for the sake of simplicity. Accordingly, the free energy functional  $F$  in Eq. (4.5) is reduced to

$$F(\rho, \eta) = \int_{\Omega} \left[ f(\rho, \eta) + \frac{\kappa_{\rho}}{2} |\nabla \rho|^2 + \frac{\kappa_{\eta}}{2} |\nabla \eta|^2 \right] d\Omega, \quad (4.67)$$

where the local free energy in Eq. (4.7) reduces to a double-well potential exhibiting minimal at the solid and atmosphere regions, that is

$$f(\rho) = W_{\text{sf}} [\rho^2(1 - \rho)^2], \quad (4.68)$$

with  $W_{\text{sf}} = \underline{C} + 7\underline{D}$  assuming identical profiles of  $\rho$  and  $\eta$  across the free surface. The time evolution equations of the OPs across the free surface can be obtained following Eq. (4.15). Moreover, for simplicity, I neglect the anisotropy of the mobility  $\mathbf{L}_{\rho\rho}$  and also drop all the antitrapping cross-coupling terms. Thereby, the time evolution of the conserved OP  $\rho$  in Eq. (4.15a) is reduced to a simple CH equation formulated as

$$\dot{\rho} = \nabla \cdot L_{\rho\rho} \nabla \mu. \quad (4.69)$$

The evolution of the non-conserved OP  $\eta$  in Eq. (4.15c) is also reduced to a simple Allen-Cahn equation given as

$$\dot{\eta} = -L_{\eta} \frac{\delta F}{\delta \eta}. \quad (4.70)$$

Employing the appropriate boundary condition  $\mathbf{n} \cdot \nabla \mu|_{\text{d}\Omega} = 0$  where  $\mathbf{n}$  is the normal to  $\text{d}\Omega$ , the integration of Eq. (4.69) yields

$$\frac{d}{dt} \int_{\Omega} \rho \, d\Omega = 0. \quad (4.71)$$

Eq. (4.71) implies that the CH dynamics in Eq. (4.69) conserves mass over the whole domain. Consequently, since  $\rho$  takes constant values of 1 and 0 in the solid and atmosphere regions respectively, this also implies mass conservation for each region as long as the free surface is thin enough. However, the numerical implementations of the CH dynamics have shown that while the CH equation ensures the conservation of the total mass in a simulation domain, the mass of individual phases is not inherently conserved. It has been demonstrated that the volume of the region enclosed by the interface shrinks during simulations and thus the profile of the conserved OP shifts from its ideal profile

due to the finite volume precept of CH dynamics [102, 103, 104]. A numerical analysis of the CH dynamics presented in Eq. (4.69) showing similar results as in Refs. [102, 103, 104] is given in Section 5.5.

### 4.3.2 Theoretical analysis

Here, I present a theoretical analysis of the deviation of  $\rho$  from its ideal values following a procedure presented in Ref. [102]. The procedure is based on the concept of energy minimization. It is assumed that obtaining ideal values of  $\rho$  in the bulk regions is contingent on the free surface having negligible volume compared to the bulk regions so that only the local free energy finds minimization. In cases where the free surface has considerable concentrated energy, the total free energy can be reduced by shrinking the area enclosed by the free surface, which subsequently shifts the bulk values of  $\rho$  from the ideal ones due to the finite volume precept. Thus, it implies that the solid region would shrink as the new shape of the relaxed free surface enjoys lower energy.

Considering a circular free surface with radius  $R$  as presented in Fig. 4.2, the total free energy of the system can be divided into two parts: the bulk energy  $F_{\text{bulk}}$  integrated over the two bulk regions, and the interfacial energy  $F_{\text{int.}}$  integrated over the free surface region. For an initial condition of  $\rho$  equal to 1 and 0,  $F_{\text{bulk}} = 0$  and  $F_{\text{int.}} = \gamma P$  where  $P = 2\pi R$  is the perimeter of the circular free surface. Moreover, I assumed a thin free surface whereby  $l \ll R$ . Also, a change in radius  $\delta R$  will be accompanied by a shift  $\delta\rho$  in the bulk values of  $\rho$ . The relationship between  $\delta\rho$  and  $\delta R$  is obtained as [102]

$$\delta\rho \approx -\frac{2P\delta R}{V} = -\frac{4\pi R\delta R}{V}, \quad (4.72)$$

where  $V$  is the volume of the domain  $\Omega$ . In Eq. (4.72) and hereinafter, only the leading order terms are considered.

The change in  $F_{\text{int.}}$  due to  $\delta R$  is obtained as

$$\delta F_{\text{int.}} \approx \gamma\delta P = 2\pi\gamma\delta R, \quad (4.73)$$

where I assumed negligible change in  $\gamma$  due to  $\delta\rho$ . Furthermore, the change in  $F_{\text{bulk}}$  due to accompanied shift in the bulk values of  $\rho$  can be obtained as

$$\delta F_{\text{bulk}} \approx \int_{\Omega} \delta f \, d\Omega \approx W_{\text{sf}}\delta\rho^2 V. \quad (4.74)$$

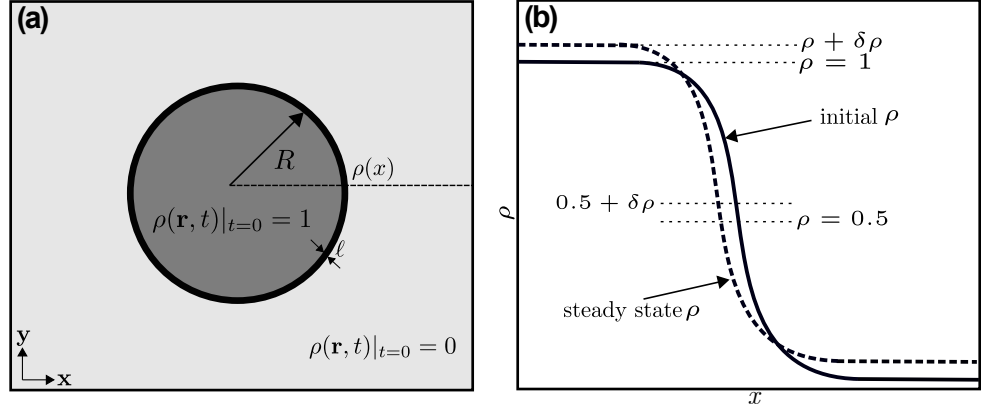


Figure 4.2: (a) Schematic of a circular free surface with radius  $R$  in a square domain. Initial values of  $\rho$  are 1 and 0 in the solid and atmosphere regions respectively; (b) Schematic of the change of  $\rho$  from its initial profile to a steady deviated profile.  $\delta\rho$  is the value of this deviation.

Combining Eqs. (4.72) - (4.74), the variation of the total energy  $F$  can be obtained as

$$\delta F \approx 2\pi\gamma\delta R + W_{\text{sf}} \frac{(4\pi R)^2}{V} \delta R^2. \quad (4.75)$$

In order to obtain  $\delta R$  and hence the final state of the circular free surface, I simply take the lowest energy state  $\frac{\partial(\delta F)}{\partial(\delta R)} = 0$ . Taking this derivative in Eq. (4.75) yields

$$\delta R = \frac{-\gamma V}{16W_{\text{sf}}\pi R^2} = \frac{-\sqrt{2}V}{96\pi R^2} \sqrt{\frac{\kappa_\eta}{6D}}, \quad (4.76)$$

where I have employed the definition of the free surface energy  $\gamma = \frac{W_{\text{sf}}}{6} \sqrt{\frac{2\kappa_\eta}{6D}}$  [29]. Substituting Eq. (4.76) into Eq. (4.72), I obtain  $\delta\rho$  as

$$\delta\rho = \frac{l}{48R}, \quad (4.77)$$

where I have also employed the formulation of the free surface width  $l = \sqrt{4\kappa_\eta/3D}$  [29]. Eq. (4.77) indicates that the deviation of  $\rho$  is directly proportional to the free surface width  $l$ , and also inversely proportional to the radius of the circular solid grain  $R$ . Hence,

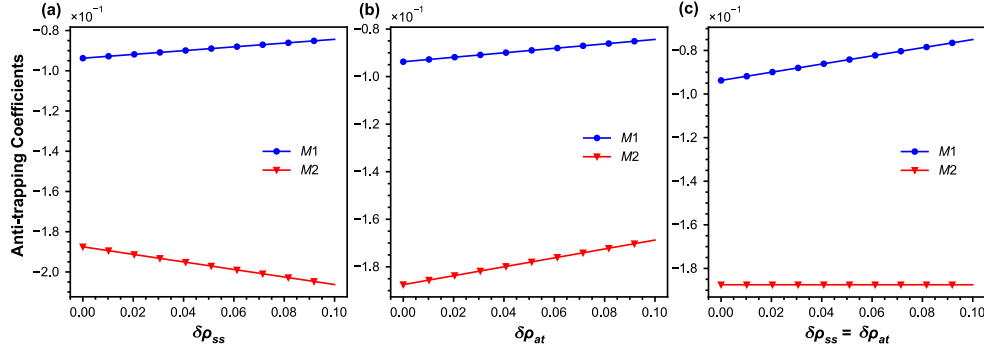


Figure 4.3: The antitrapping coefficients  $M_1$  and  $M_2$  with respect to (a) varying  $\delta\rho_{ss}$  when  $\delta\rho_{at} = 0$ , (b) varying  $\delta\rho_{at}$  when  $\delta\rho_{ss} = 0$ , and (c) varying simultaneously  $\delta\rho_{ss}$  and  $\delta\rho_{at}$  while holding  $\delta\rho_{ss} = \delta\rho_{at}$ .

a way to significantly reduce the deviation of  $\rho$  would be to consider a value of  $l$  which is relatively smaller compared to  $R$ . Eq. (4.77) also implies that the deviation of  $\rho$  has a strong direct dependency on curvature. Moreover, it also denotes that theoretically, the deviation of  $\rho$  becomes negligible as  $l$  tends towards the sharp-interface limit ( $l \rightarrow 0$ ). In addition, the comparison of theoretically obtained  $\delta\rho$  in Eq. (4.77) and that of the observed  $\delta\rho$  in numerical results is made in Section 5.5.

#### Variations of $M_1$ and $M_2$ with deviation of $\rho$

Since the antitrapping coefficients  $M_1$  and  $M_2$  are dependent on the bulk values of  $\rho$ ,  $\rho_{ss}$  and  $\rho_{at}$  (as seen in Eqs. (4.49) and (4.55)), the variations of  $M_1$  and  $M_2$  with deviation of  $\rho$  are examined. These variations are presented in Fig. 4.3 with  $\delta\rho_{ss} = \rho_{ss} - 1$  and  $\delta\rho_{at} = \rho_{at} - 1$  up to 0.1. In Fig. 4.3a,  $\delta\rho_{at} = 0$  is taken and the variations of  $M_1$  and  $M_2$  with  $\delta\rho_{ss}$  are examined. Similarly,  $\delta\rho_{ss} = 0$  is taken and the variations of  $M_1$  and  $M_2$  with  $\delta\rho_{at}$  are examined in Fig. 4.3b. Then, the variations of  $M_1$  and  $M_2$  with  $\delta\rho_{ss} = \delta\rho_{at}$  are presented in Fig. 4.3c. The results demonstrate that  $M_1$  presents a linear tendency vs. increasing deviations in all cases.  $M_2$ , however, decreases along with growing  $\delta\rho_{ss}$  but increases with growing  $\delta\rho_{at}$ . For  $\delta\rho_{ss} = \delta\rho_{at}$ ,  $M_2$  stays constant. This can be explained via Eq. (4.49) where  $M_2$  is proportional to  $(\rho_{ss} - \rho_{at})$ , which is reduced to one when  $\delta\rho_{ss} = \delta\rho_{at}$  as  $(\rho_{ss} - \rho_{at}) = [(\delta\rho_{ss} + 1) - \delta\rho_{at}] = 1$ .





---

## 5 Variational Quantitative Phase-field Model of Non-isothermal Sintering: Numerical Implementation and Verification

---

Following the introduction of the formulations of a variational quantitative phase-field model for non-isothermal sintering, the numerical implementation and verification of the model are presented in this chapter. First, the details of the numerical implementation of the governing equations based on the finite element method are presented in Section 5.1. Moreover, the verification of the quantitative model is performed in Section 5.2, considering diffusion-driven reshaping simulations. The importance of the proposed mass and thermal antitrapping currents in the sense of eliminating abnormal interface effects was demonstrated with respect to various interface widths. Following this, the quantitative model was also compared to the existing conventional model via thermo-microstructural evolutions and sintering kinetics. For simple numerical simulations of two grains coalescence, the results of the evolution of microstructure, temperature distribution, sintering neck, and dihedral angle were compared for both models as presented in Section 5.3. The importance of the proposed anisotropic interpolations of mass and thermal diffusion mobilities was also demonstrated in Section 5.4. Finally, a detailed numerical analysis of the deviation of the conserved order parameter across the free surfaces is given in Section 5.5.

### 5.1 Finite-element Implementation

Here the detailed finite element implementation including discretization and linearization of residuals, and the utilization of the penalty method for the constraint of OPs is

presented. The numerical implementation is done within the open-sourced simulation package NisoS (*Non-Isothermal Simulator*) [6, 36] which was developed based on the MOOSE (*Multiphysics Object Oriented Simulation Environment*) framework [105, 106]. The basic features regarding the MOOSE framework, including transient solver with preconditioned Jacobian-Free Newton–Krylov method (PJFNK) and backward Euler algorithm, and adaptive meshing and time stepping schemes, are explicitly given in Ref. [105].

The residuals for the weak forms of Eq. (4.15) can be formulated by introducing corresponding trial functions  $\psi_\mu$ ,  $\psi_\rho$ ,  $\psi_\eta$  and  $\psi_T$ , respectively, and integrating by parts over the subdomain  $\Omega$ , i.e.

$$\left\{ \begin{aligned}
 R_\mu &= \int_\Omega \dot{\rho} \psi_\mu d\Omega + \int_\Omega \mathbf{L}_{\rho\rho} \cdot \left[ \nabla \left( \frac{\mu}{T} \right) + M_1 l \sum_i \dot{\eta}_i \nabla \rho \right] \cdot \nabla \psi_\mu d\Omega \\
 &\quad - \int_\Gamma \psi_\mu \mathbf{L}_{\rho\rho} \cdot \left[ \nabla \left( \frac{\mu}{T} \right) + M_1 l \sum_i \dot{\eta}_i \nabla \rho \right] \cdot \mathbf{n} d\Gamma \\
 R_\rho &= \int_\Omega \frac{\partial f}{\partial \rho} \psi_\rho d\Omega - \int_\Omega \mu \psi_\rho d\Omega + \int_\Omega \kappa_\rho T \nabla \rho \cdot \nabla \psi_\rho d\Omega - \int_\Gamma \kappa_\rho T \nabla \rho \psi_\rho \cdot \mathbf{n} d\Gamma \\
 &\quad + \int_\Omega \mathfrak{p} \frac{\partial \Sigma_h}{\partial \rho} \psi_\rho d\Omega \\
 R_{\eta_i} &= \int_\Omega \hat{L}_{\eta_i}^{-1} \dot{\eta}_i \psi_\eta d\Omega + \int_\Omega \frac{1}{T} \frac{\partial f}{\partial \eta_i} \psi_\eta d\Omega + \int_\Omega \kappa_\eta \nabla \eta_i \nabla \psi_\eta d\Omega - \int_\Gamma \kappa_\eta \nabla \eta_i \psi_\eta \cdot \mathbf{n} d\Gamma \\
 &\quad + \int_\Omega l \nabla \rho \cdot M_1 \mathbf{L}_{\rho\rho} \cdot \nabla \left( \frac{\mu}{T} \right) \psi_\eta d\Omega + \int_\Omega l \nabla \rho \cdot M_2 \mathbf{k} \cdot \nabla T \psi_\eta d\Omega + \int_\Omega \mathfrak{p} \frac{\partial \Sigma_h}{\partial \eta_i} \psi_\eta d\Omega \\
 R_T &= \int_\Omega c_r T \psi_T d\Omega + \int_\Omega \frac{\partial e}{\partial \rho} \dot{\rho} \psi_T d\Omega + \sum_i \int_\Omega \frac{\partial e}{\partial \eta_i} \dot{\eta}_i \psi_T d\Omega \\
 &\quad + \int_\Omega \mathbf{k} \cdot \left[ \nabla T + M_2 T^2 l \sum_i \dot{\eta}_i \nabla \rho \right] \cdot \nabla \psi_T d\Omega - \int_\Gamma \mathbf{k} \cdot (\nabla T \psi_T \cdot \mathbf{n}) d\Gamma \\
 &\quad - \int_\Gamma M_2 T^2 l \sum_i \dot{\eta}_i \psi_T \mathbf{k} \cdot \nabla \rho \cdot \mathbf{n} d\Gamma,
 \end{aligned} \right. \quad (5.1)$$

where  $\mathbf{n}$  is the normal vector to the boundary  $\Gamma$  of the subdomain.  $\mathfrak{p}$  is the penalty prefactor and  $\Sigma_h$  is the penalty function, i.e.

$$\Sigma_h = \left[ \left( h_\rho + \sum_i h_{\eta_i} \right) - 1 \right]^2, \quad (5.2)$$

with

$$h_\rho = 1 - \rho^3 (10 - 15\rho + 6\rho^2), \quad h_{\eta_i} = \eta_i^3 (10 - 15\eta_i + 6\eta_i^2),$$

introduced to implement the OPs constraint  $(1 - \rho) + \sum_i \eta_i = 1$ .

Following the Galerkin approach, the test functions are discretized as

$$\psi_\mu = \sum_I N_\mu^I \psi_\mu^I, \quad \psi_\rho = \sum_I N_\rho^I \psi_\rho^I, \quad \psi_\eta = \sum_I N_\eta^I \psi_\eta^I, \quad \psi_T = \sum_I N_T^I \psi_T^I,$$

where  $I$  denotes the node index and  $\psi_\mu^I, \psi_\rho^I, \psi_\eta^I$  and  $\psi_T^I$  are the nodal weights while  $N_\mu^I, N_\rho^I, N_\eta^I$  and  $N_T^I$  are the shape functions for the corresponding variables. The discretized residuals from Eq. (5.1) can then be obtained as

$$\left\{ \begin{aligned} R_\mu^I &= \int_\Omega \dot{\rho} N_\mu^I d\Omega + \int_\Omega \mathbf{L}_{\rho\rho} \cdot \left[ \nabla \left( \frac{\mu}{T} \right) + M_1 l \sum_i \eta_i \nabla \rho \right] \cdot \nabla N_\mu^I d\Omega \\ &\quad - \int_\Gamma N_\mu^I \mathbf{L}_{\rho\rho} \cdot \left[ \nabla \left( \frac{\mu}{T} \right) + M_1 l \sum_i \eta_i \nabla \rho \right] \cdot \mathbf{n} d\Gamma \\ R_\rho^I &= \int_\Omega \frac{\partial f}{\partial \rho} N_\rho^I d\Omega - \int_\Omega \mu N_\rho^I d\Omega + \int_\Omega \kappa_\rho T \nabla \rho \cdot \nabla N_\rho^I d\Omega - \int_\Gamma \kappa_\rho T \nabla \rho N_\rho^I \cdot \mathbf{n} d\Gamma \\ &\quad + \int_\Omega p \frac{\partial \Sigma_h}{\partial \rho} N_\rho^I d\Omega \\ R_{\eta_i}^I &= \int_\Omega \hat{L}_\eta^{-1} \eta_i N_\eta^I d\Omega + \int_\Omega \frac{1}{T} \frac{\partial f}{\partial \eta_i} N_\eta^I d\Omega + \int_\Omega \kappa_\eta \nabla \eta_i \nabla N_\eta^I d\Omega - \int_\Gamma \kappa_\eta \nabla \eta_i N_\eta^I \cdot \mathbf{n} d\Gamma \\ &\quad + \int_\Omega l \nabla \rho \cdot M_1 \mathbf{L}_{\rho\rho} \cdot \nabla \left( \frac{\mu}{T} \right) N_\eta^I d\Omega + \int_\Omega l \nabla \rho \cdot M_2 \mathbf{k} \cdot \nabla T N_\eta^I d\Omega + \int_\Omega p \frac{\partial \Sigma_h}{\partial \eta_i} N_\eta^I d\Omega \\ R_T^I &= \int_\Omega c_r \dot{T} N_T^I d\Omega + \int_\Omega \frac{\partial e}{\partial \rho} \dot{\rho} N_T^I d\Omega + \sum_i \int_\Omega \frac{\partial e}{\partial \eta_i} \dot{\eta}_i N_T^I d\Omega \\ &\quad + \int_\Omega \mathbf{k} \cdot \left[ \nabla T + M_2 T^2 l \sum_i \eta_i \nabla \rho \right] \cdot \nabla N_T^I d\Omega - \int_\Gamma \mathbf{k} \cdot (\nabla T N_T^I \cdot \mathbf{n}) d\Gamma \\ &\quad - \int_\Gamma M_2 T^2 l \sum_i \eta_i N_T^I \mathbf{k} \cdot \nabla \rho \cdot \mathbf{n} d\Gamma. \end{aligned} \right. \quad (5.3)$$

Similarly, the variable fields  $\mu, \rho, \eta_i, T$  as well as their time derivatives  $\dot{\mu}, \dot{\rho}, \dot{\eta}_i, \dot{T}$  are also discretized by the shape functions, i.e.

$$\begin{aligned}\rho &= \sum_J N_\rho^J \rho^J, & \mu &= \sum_J N_\mu^J \mu^J, & \eta_i &= \sum_J N_\eta^J \eta_i^J, & T &= \sum_J N_T^J T^J; \\ \dot{\rho} &= \sum_J N_\rho^J \dot{\rho}^J, & \dot{\mu} &= \sum_J N_\mu^J \dot{\mu}^J, & \dot{\eta}_i &= \sum_J N_\eta^J \dot{\eta}_i^J, & \dot{T} &= \sum_J N_T^J \dot{T}^J,\end{aligned}$$

where  $\mu^J, \rho^J, \eta_i^J$  and  $T^J$  are the nodal values. The linearization of the residuals gives the following element-level linear equations

$$\begin{aligned}\begin{bmatrix} R_\mu^I \\ R_\rho^I \\ R_{\eta_1}^I \\ \vdots \\ R_{\eta_n}^I \\ R_T^I \end{bmatrix} &= - \begin{bmatrix} K_{\mu,\mu}^{IJ} & K_{\mu,\rho}^{IJ} & K_{\mu,\eta_1}^{IJ} & \cdots & K_{\mu,\eta_n}^{IJ} & K_{\mu,T}^{IJ} \\ K_{\rho,\mu}^{IJ} & K_{\rho,\rho}^{IJ} & K_{\rho,\eta_1}^{IJ} & \cdots & K_{\rho,\eta_n}^{IJ} & K_{\rho,T}^{IJ} \\ K_{\eta_1,\mu}^{IJ} & K_{\eta_1,\rho}^{IJ} & K_{\eta_1,\eta_1}^{IJ} & \cdots & K_{\eta_1,\eta_n}^{IJ} & K_{\eta_1,T}^{IJ} \\ \vdots & \vdots & \vdots & \ddots & \vdots & \vdots \\ K_{\eta_n,\mu}^{IJ} & K_{\eta_n,\rho}^{IJ} & K_{\eta_n,\eta_1}^{IJ} & \cdots & K_{\eta_n,\eta_n}^{IJ} & K_{\eta_n,T}^{IJ} \\ K_{T,\mu}^{IJ} & K_{T,\rho}^{IJ} & K_{T,\eta_1}^{IJ} & \cdots & K_{T,\eta_n}^{IJ} & K_{T,T}^{IJ} \end{bmatrix} \begin{bmatrix} \delta\mu^J \\ \delta\rho^J \\ \delta\eta_1^J \\ \vdots \\ \delta\eta_n^J \\ \delta T^J \end{bmatrix} \\ &- \begin{bmatrix} D_{\mu,\mu}^{IJ} & D_{\mu,\rho}^{IJ} & D_{\mu,\eta_1}^{IJ} & \cdots & D_{\mu,\eta_n}^{IJ} & D_{\mu,T}^{IJ} \\ D_{\rho,\mu}^{IJ} & D_{\rho,\rho}^{IJ} & D_{\rho,\eta_1}^{IJ} & \cdots & D_{\rho,\eta_n}^{IJ} & D_{\rho,T}^{IJ} \\ D_{\eta_1,\mu}^{IJ} & D_{\eta_1,\rho}^{IJ} & D_{\eta_1,\eta_1}^{IJ} & \cdots & D_{\eta_1,\eta_n}^{IJ} & D_{\eta_1,T}^{IJ} \\ \vdots & \vdots & \vdots & \ddots & \vdots & \vdots \\ D_{\eta_n,\mu}^{IJ} & D_{\eta_n,\rho}^{IJ} & D_{\eta_n,\eta_1}^{IJ} & \cdots & D_{\eta_n,\eta_n}^{IJ} & D_{\eta_n,T}^{IJ} \\ D_{T,\mu}^{IJ} & D_{T,\rho}^{IJ} & D_{T,\eta_1}^{IJ} & \cdots & D_{T,\eta_n}^{IJ} & D_{T,T}^{IJ} \end{bmatrix} \begin{bmatrix} \delta\dot{\mu}^J \\ \delta\dot{\rho}^J \\ \delta\dot{\eta}_1^J \\ \vdots \\ \delta\dot{\eta}_n^J \\ \delta\dot{T}^J \end{bmatrix}.\end{aligned}\tag{5.4}$$

The terms in the tangent matrix and the damping matrix are obtained as  $K_{\xi,\zeta}^{IJ} = \partial R_\xi^I / \partial \zeta^J$  and  $D_{\xi,\zeta}^{IJ} = \partial R_\xi^I / \partial \dot{\zeta}^J$ . These terms were all obtained using the automatic differentiation (AD) method in MOOSE framework. The basic description and features of the AD method as implemented in MOOSE are explicitly given in Ref. [107].

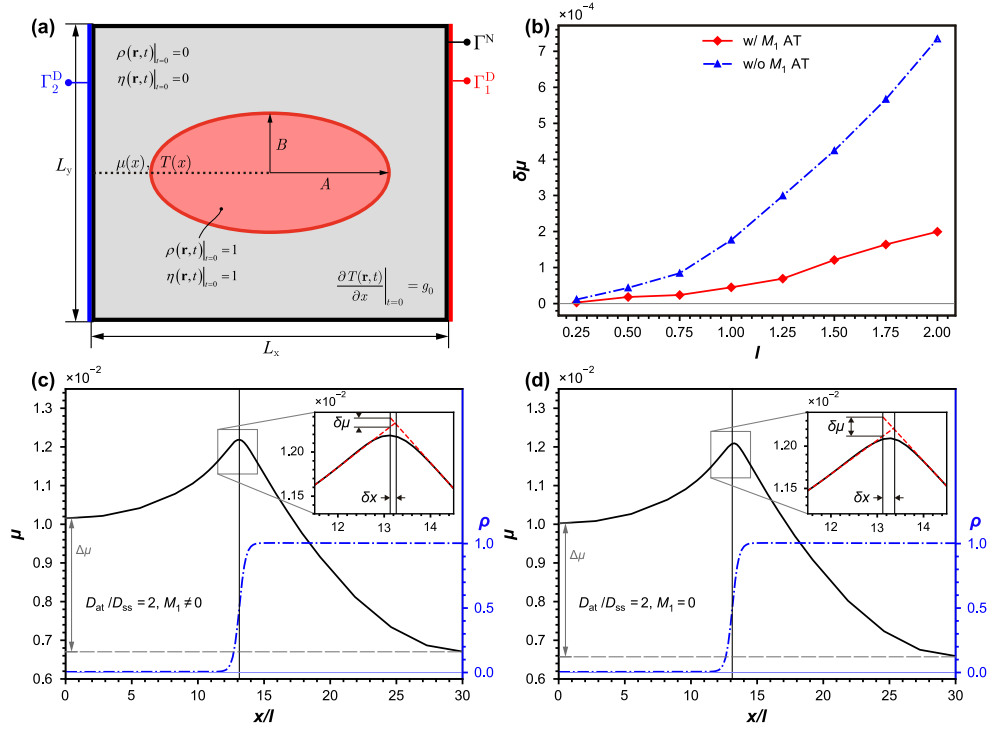


Figure 5.1: (a) Schematic of the simulation setup in a 2D simulation of an elliptical particle (b) Comparison of chemical potential jump  $\delta\mu$  across the free surface with respect to interface width; blue triangle symbols represent model with  $M_1 = 0$  while red diamond symbols represent model with  $M_1 \neq 0$ . Plots of  $\mu$  and  $\rho$  across the free surface as a function of  $x$  with  $l = 1$ ,  $D_{at}/D_{ss} = 2$  for (c)  $M_1 \neq 0$  and (d)  $M_1 = 0$ .  $\delta\mu$  is obtained using an extrapolation of  $\mu$  at the center of the free surface  $\rho = 0.5$ .  $\Delta\mu$  is the chemical potential difference between the bulk values.

## 5.2 Model Verification For an Elliptical Inclusion

In order to examine the capability of the quantitative model in ensuring *zero temperature jump* and *zero chemical potential jump* ( $\delta\mu = \delta T = 0$ ) at the free surface, diffusion-driven reshaping simulations of an elliptical inclusion are performed. A simulation domain with the lengths  $L_x$  and  $L_y$  in  $x$  and  $y$  direction is set up. An elliptical particle with major

Table 5.1: Set of dimensionless quantities and parameters employed for simulations.

$L_x$	$L_y$	$g_0$	$\underline{C}$	$\underline{D}$	$e_{\text{ht}}$	$L_{\eta,\text{gb}}$	$s_v$
60	50	0.01	1	0.062	1	1	1

axis  $A$  and minor axis  $B$  is placed at the center of the domain. Moreover, the domain is subjected to an initial temperature gradient  $\nabla T = g_0$  along the  $x$ -axis. The OP  $\rho$  is taken to vary smoothly from one in the inclusion ( $\rho_{\text{ss}} = 1$ ) to zero outside ( $\rho_{\text{at}} = 0$ ) with interface width  $l = 1$ . A full schematic of the simulation setup is given in Fig. 5.1a. Also, the normalized values of the employed model parameters are given in Table 5.1.

### 5.2.1 Mass antitrapping current

First, I consider a case of asymmetric mass transport where  $D_{\text{at}}/D_{\text{ss}} = 2$ . Thermal conductivity ratio  $k_{\text{at}}/k_{\text{ss}} = 1$  is set, thus only the mass antitrapping current term associated with mass diffusion is employed while the thermal antitrapping current is deprecated. Profile of chemical potential  $\mu(x)$  across the moving free surface is presented for the cases  $M_1 = 0$  and  $M_1 \neq 0$  in Figs. 5.1c and 5.1d, respectively. An extrapolation of  $\mu(x)$  gives the chemical potential jump ( $\delta\mu$ ) at the center of the free surface. Typically,  $\delta\mu \neq 0$  implies an exchange of mass between the solid and atmosphere, which is attributed to the trans-interface diffusion phenomenon. However, during sintering, no mass exchange is expected between the solid and atmosphere regions. Therefore,  $\delta\mu = 0$  should be held in phase-field simulations in order to achieve realistic mass diffusion. The case with  $M_1 = 0$  (Fig. 5.1c) shows a significantly larger  $\delta\mu$  compared to the one with  $M_1 \neq 0$  (Fig. 5.1d), in which the relatively small  $\delta\mu$  attributes to possible numerical errors. The results demonstrate that the mass antitrapping current, parameterized by  $M_1$  is necessary to eliminate the artificial diffusion flux across the free surface for cases of asymmetric mass transport. Figs. 5.1c and 5.1d also show the gap in space  $\delta x$  between the center of the free surface and the point where the extrapolations of  $\mu$  meet. Note that  $\delta x = 0$  when  $\delta\mu = 0$ , indicating the coherence between the numerically predicted interface by  $\rho \approx 0.5$  and the theoretical sharp interface where  $\delta\mu = 0$ . Similar to  $\delta\mu$ , the numerical results demonstrate a significantly larger  $\delta x$  for the case with  $M_1 = 0$  compared to the one with  $M_1 \neq 0$ , implying an apparent deviation in the position between the predicted interface and theoretical sharp interface.

Meanwhile, I note the existence of another chemical potential drop  $\Delta\mu$  across the free

surface, characterizing the differences between the bulk values, as depicted in Figs. 5.1c and 5.1d. This  $\Delta\mu$ , which is identical for both cases at a time point, was numerically examined to be the outcome of the deviated bulk values of  $\rho$ , i.e.,  $\rho_{ss}$  and  $\rho_{at}$  that are slightly deviated from ideal (equilibrium) one and zero respectively, as listed in Table 5.2. Such chemical potential drop generally does not appear in the conventional sharp-interface interpretation of the sintering [10, 11]. The deviated bulk values of the conserved mass OP have also been depicted in previous works [102, 103, 108, 109, 110]. Theoretical and numerical analyses of the deviation of OP  $\rho$  in the bulk regions are given in Sections 4.3 and 5.5 respectively.

Table 5.2: The non-equilibrium bulk values of substance field and the chemical potential measured from simulations with  $M_1 = 0$  and  $M_1 \neq 0$ , respectively.

	$\rho_{at}^*$	$\rho_{ss}^*$	$\mu_{at}$	$\mu_{ss}$
$M_1 = 0$	0.00477	1.00308	0.01002	0.00659
$M_1 \neq 0$	0.00483	1.00313	0.01015	0.00671

Furthermore, Fig. 5.1b shows a comparison of chemical potential jump  $\delta\mu$  vs. diffuse interface width  $l$  between the cases with and without  $M_1$  parameterized. It can be observed that both cases present the convergence  $\delta\mu \rightarrow 0$  as  $l \rightarrow 0$ , replicating the sharp-interface condition when  $l$  tends to infinitesimal. However, as  $l$  increases,  $\delta\mu$  present relatively rapid growth in the case with  $M_1 = 0$  compared to the one with  $M_1 \neq 0$ , demonstrating that the employment of mass antitrapping current parameterized by  $M_1$  can significantly reduce the abnormal interface effect (here the growing  $\delta\mu$ ) along with increasing diffuse interface width. In this sense, mass antitrapping current allows reasonable quantitative simulations, especially at larger interface widths. Furthermore, it is worth noting that the convergence of both models might be well investigated considering a steady state free surface velocity. This serves as a major outlook of this thesis.

## 5.2.2 Thermal antitrapping current

Additionally, I investigate a case of asymmetric heat transport with  $k_{at}/k_{ss} = 0.05$ . Similar to the previous simulation, I examine the thermal antitrapping current term associated with heat transport. The mass antitrapping current term is tentatively dropped by simply

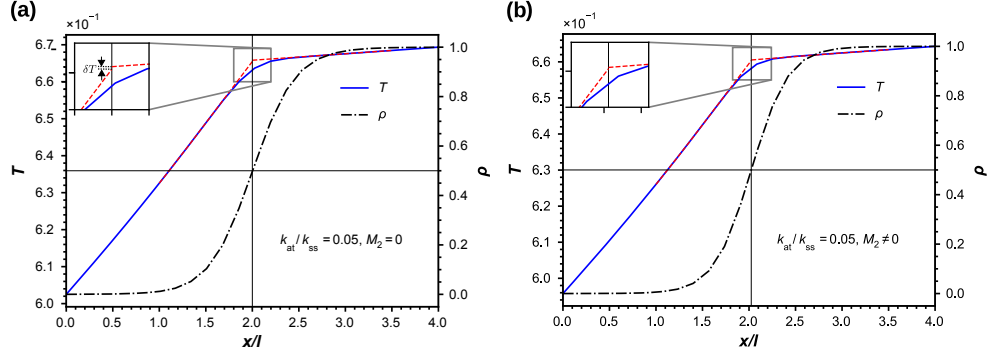


Figure 5.2: Plots of  $T$  and  $\rho$  across the free surface as a function of  $x$  with  $l = 1$ ,  $k_{\text{at}}/k_{\text{ss}} = 0.05$  for (a)  $M_2 = 0$  and (b)  $M_2 \neq 0$ .  $\delta T$  is obtained using an extrapolation of  $T$  at the centre of the free surface  $\rho = 0.5$ .

setting  $D_{\text{at}}/D_{\text{ss}} = 1$ . Simulations are performed for the existing model (i.e.,  $M_2 = 0$ ) and quantitative model with  $M_2 \neq 0$ . The results are shown in Fig. 5.2.  $\delta T = 0$  realized at the sharp-interface is expected to be obtained during phase-field simulations in order to guarantee quantitative simulations. For the model with  $M_2 = 0$ , however, emerging  $\delta T \neq 0$  demonstrates the importance of the thermal antitrapping current. However, it is important to note that the measured  $\delta T$  has a relatively low magnitude compared to the bulk temperature at the free surface. The importance of thermal antitrapping term  $M_2$  in eliminating temperature jump for asymmetric heat transport has also been demonstrated in Ref. [82] where a quantitative phase-field model was also used.

### 5.3 Comparison With Existing Model

This section presents the numerical simulations for grain coalescence of two spherical grains with distinct sizes. Comparisons of microstructure, temperature profile, and sintering kinetics are made between the quantitative model where antitrapping terms are taken into account, and the existing model where these terms are not considered. The two models are referred to as the *model with ATs* and the *model without ATs* in the following discussions. For the numerical simulations, I set up a simulation domain with the lengths  $L_x$  and  $L_y$  in  $x$  and  $y$  direction, respectively. Similar to the previous setup in Section 5.2, the domain is subjected to temperature gradient  $\nabla T = g_0$  along the  $x$ -axis.



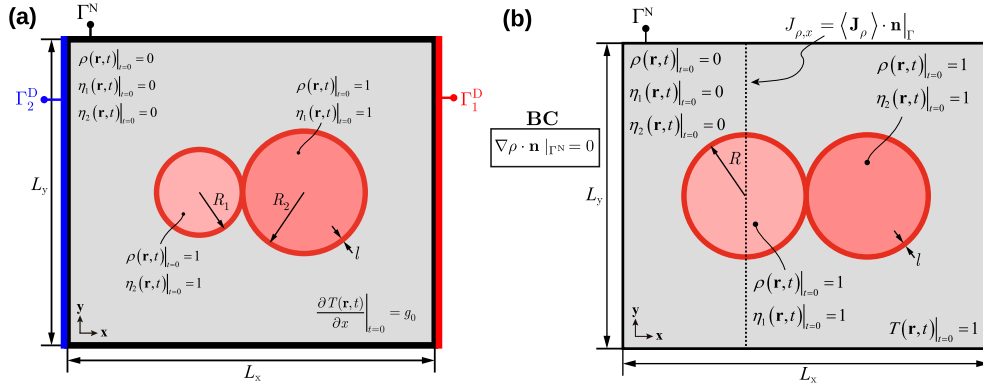


Figure 5.3: Schematic of the simulation setup and boundary conditions used in the 2D simulation of (a) two unidentical grains coalescence and (b) two identical grains coalescence.  $J_{\rho,x}$  (calculated on the denoted boundary) is also denoted.

Simulations are performed for asymmetric mass and heat transport where  $D_{at}/D_{ss} = 2$ ,  $k_{at}/k_{ss} = 0.05$  with interface width  $l = 2$ . A full schematic of the simulation setup is presented in Fig. 5.3a.

### 5.3.1 Thermo-microstructural comparison

Transient microstructures and temperature profiles for both models are compared and presented in Fig. 5.4. First, it can be observed that mass transport is faster for the model without ATs compared to the model with ATs. At  $t/t^* = 0.633$  and  $t/t^* = 0.815$  in Figs. 5.4c and 5.4d respectively, a more coalesced grain is obtained for the model without ATs compared to the model with ATs. Furthermore, results in Fig. 5.4 also show the comparison of the temperature profiles obtained for both models. A faster heat transport for the model without ATs compared to the model with ATs can be observed by comparing the movement of the temperature isolines. An example is given for isoline  $T = 0.71$ . Even though it initially tends to migrate towards the high- $T$  side, at  $t/t^* = 0.023$ , this tendency breaks for the model without ATs, where the isoline starts to move towards low- $T$  side but continues for the model with ATs. The result at  $t/t^* = 0.815$  in Fig. 5.4d indicates a colder grain for the model with ATs compared to the model without ATs.

The difference in the progress of coalescence and temperature profiles can be further

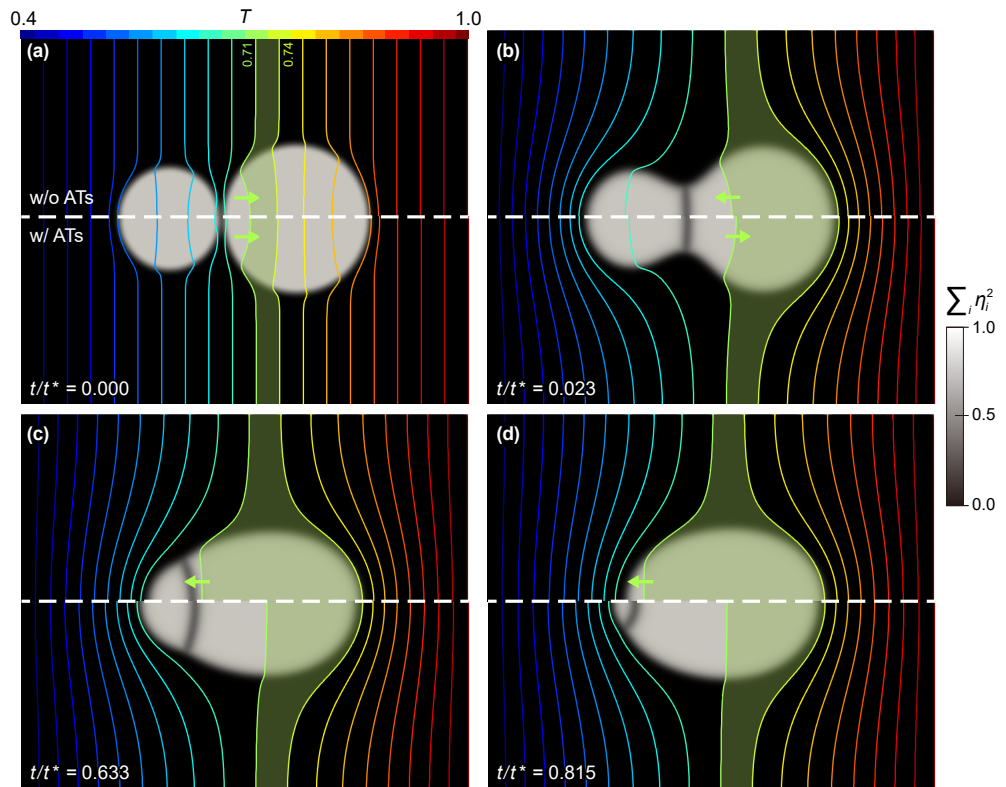


Figure 5.4: Snapshots of grains coalescence of two spherical grains with distinct sizes.  $D_{at}/D_{ss} = 2$ ,  $l = 2$  and  $k_{at}/k_{ss} = 0.05$  are set. Comparison is made between models with ATs and without ATs. Temperature isolines are also indicated.  $t^* = 10^3$  units.

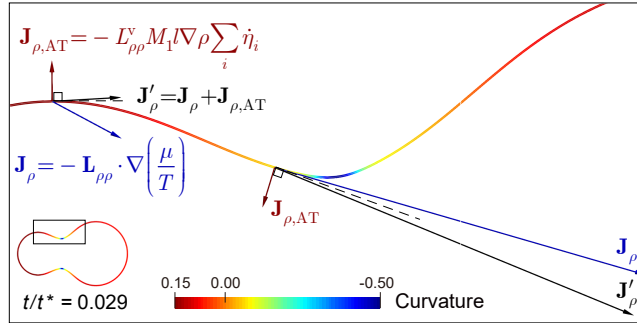


Figure 5.5: Surface profile ( $\rho = 0.5$ ) with curvature indicated by the coloring and the mass diffusion fluxes, i.e., the fluxes before ( $\mathbf{J}_\rho$ ) and after ( $\mathbf{J}'_\rho$ ) correction with the antitrapping contribution ( $\mathbf{J}_{\rho,AT}$ ), at two distinct sites. The lengths of visualized arrows have been scaled according to the magnitude of the fluxes uniformly.

explained by the visualization of mass diffusion fluxes at the free surface as presented in Fig. 5.5. The free surface profile is colored by the local curvature calculated as  $-\nabla \cdot \mathbf{n}_{sf}$ . Furthermore, mass diffusion fluxes are indicated at two distinct points; a concave point and a convex point. Typically, the mass flux at any point on the free surface is expected to be correctly captured along the tangential direction to the free surface at that point. It can be clearly observed that  $\mathbf{J}_\rho$ , the mass diffusion flux without the mass antitrapping current, deviates from the tangential direction (dash-dotted lines) to the free surface at both concave and convex points. The mass antitrapping flux  $\mathbf{J}_{\rho,AT}$  introduced in the quantitative model can be seen flowing through the free surface in the normal direction from the solid grain region to the atmosphere. The combined mass flux  $\mathbf{J}'_\rho = \mathbf{J}_\rho + \mathbf{J}_{\rho,AT}$  shows a corrected mass flux flowing along the tangential direction to the free surface. Therefore, the deviation of  $\mathbf{J}_\rho$  from its appropriate direction is due to the existence of a chemical potential jump at the free surface.  $\mathbf{J}_{\rho,AT}$  serves to eliminate this chemical potential jump which consequently corrects this deviation. Accordingly, this demonstrates the faster mass transport observed for the model without ATs. A chemical potential jump at the free surface tends to act as an extra driving force for grain coalescence leading to faster mass diffusion. The elimination of this jump via the antitrapping current leads to a slower mass transport for the model with ATs. Similarly, the temperature jump at the free surface can be seen as an extra driving force for heat transport in the model without ATs. This jump is eliminated for the model with ATs via the thermal antitrapping term thereby obtaining a slower heat transport. The presented thermal-microstructure evolution once more demonstrates the importance of

the antitrapping currents for mass and heat diffusion.

### 5.3.2 Kinetics of the sintering neck and dihedral angle

Here, the features of sintering kinetics are examined for the simulation results presented in Fig. 5.4. In particular, in-process sintering neck  $\lambda$  and dihedral angle  $\Phi$  are obtained and compared for both models.  $\lambda$  and  $\Phi$  are calculated by

$$\lambda = \int_{\Omega} \frac{16 \sum_{i \neq j} \eta_i^2 \eta_j^2}{l} d\Omega, \quad (5.5)$$

$$\Phi = \arctan \left( \frac{\partial C_{\eta_i}}{\partial x} \right)_{\text{neck}} - \arctan \left( \frac{\partial C_{\eta_j}}{\partial x} \right)_{\text{neck}},$$

where  $C_{\eta_i}$  and  $C_{\eta_j}$  are the fitted semi-circular tendencies by coordinates of contour  $\eta_i = 0.5$  and  $\eta_j = 0.5$ , respectively.  $\frac{\partial C_{\eta_i}}{\partial x}$  and  $\frac{\partial C_{\eta_j}}{\partial x}$  then provide the slopes of  $C_{\eta_i}$  and  $C_{\eta_j}$ . In this sense,  $\Phi$  is calculated using the difference between these two angles of slope at the neck point, as shown in the inset of Fig. 5.7b, adapted from Ref. [111]. Meanwhile, the equilibrium dihedral angle  $\Phi_{\text{eq}}$  can be also evaluated by the surface ( $\gamma_{\text{sf}}$ ) and grain boundary ( $\gamma_{\text{gb}}$ ) energies, i.e.,

$$\Phi_{\text{eq}} = 2 \arccos \frac{\gamma_{\text{gb}}}{2\gamma_{\text{sf}}}. \quad (5.6)$$

It is worth noting that  $\Phi$  approaches  $\Phi_{\text{eq}}$  when two particles with identical size are sintered isothermally, as  $\lambda$  reaches the maximum and stays constant, i.e., the system reaches equilibrium [6]. The value of  $\Phi_{\text{eq}}$  obtained is similar for both models with/without ATs as shown in Fig. 5.6a. This implies no modification to the thermodynamic equilibrium condition (characterized by  $\Phi_{\text{eq}}$ ) by applying the kinetic antitrapping terms. However, the evolution of neck size with time is different for both models. Considering the neck growth equation,  $(\lambda/d)^n = Kt$  where  $d$  is the original particle diameter,  $t$  is sintering time,  $K$  is a fitting parameter, and  $n$  is a coefficient that depends on the mass transfer process [10, 24, 27], the values of  $n$  obtained are different for both models (shown in Fig. 5.6b). For two non-identical grains, the time evolution of  $\lambda$  and  $\Phi$  are presented in Fig. 5.7. Comparison is made for the model with ATs and the model without ATs. It can be observed that for both models,  $\Phi$  approaches  $\Phi_{\text{eq}}$  at the points where  $\lambda$  attains maximum values. However, the progress of  $\Phi$  towards  $\Phi_{\text{eq}}$  is faster for the model without ATs compared to the model with ATs. This implies that while thermodynamic conditions are attained for both models, the antitrapping terms tend to modify the progress of

neck growth and grain coalescence by removing the extra flux perpendicular to the free surface, as evidently shown in Figs. 5.4 and 5.5.

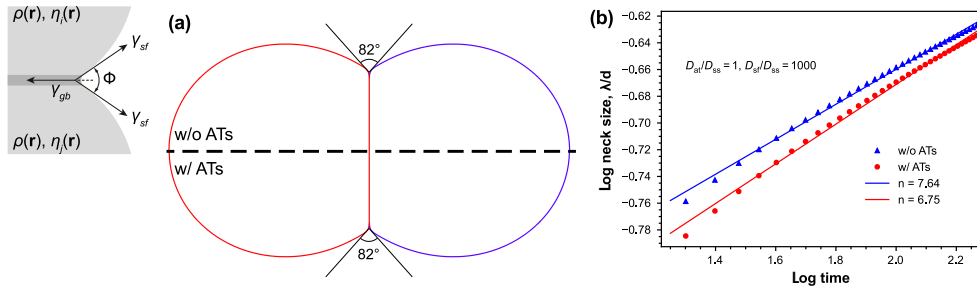


Figure 5.6: (a) Simulated dihedral angle for model without ATs and model with ATs. The red and blue curves shown are the isocontours of  $\eta_i = 1/2$  and  $\eta_j = 1/2$  respectively; (b) Evolution of neck size with time for the model without ATs and model with ATs. Inset: schematic of the formation of the dihedral angle where  $\gamma_{gb}$  and  $\gamma_{sf}$  are the grain boundary and surface energies respectively.

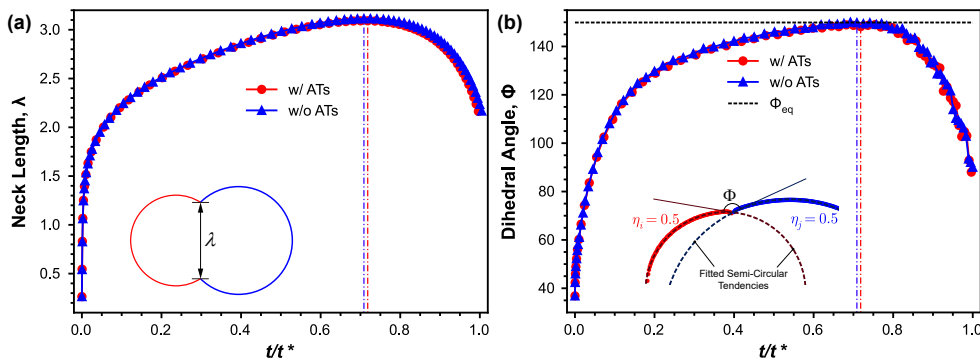


Figure 5.7: Time evolution of (a) sintering neck  $\lambda$  and (b) dihedral angle  $\Phi$  during the non-isothermal sintering process, as shown in Fig. 5.4. The time points reaching maximum values are indicated by colored vertical lines. The equilibrium dihedral angle  $\Phi_{eq}$ , calculated from the surface and grain boundary energies, is also indicated by a black dotted line in (b). The total simulation time  $t^* = 2084$  units.

---

## 5.4 Importance of Anisotropic Interpolations

In this section, the importance of the anisotropic interpolations of kinetics mobilities is demonstrated. As discussed in Subsection 4.2.3, interface trapping effects and the existence of surface diffusion in conservation laws are direction-dependent. Thus, conventional isotropic formulations of diffusion mobilities are limited in the sense of simultaneous elimination of all associated abnormal interface effects. The anisotropic interpolation scheme which differentiates the mobility interpolations at the normal and the tangential directions along the interface allows the elimination of all associated interface effects without any constraint. Within this section, numerical investigations are performed to demonstrate the importance of the choice of this anisotropic interpolation scheme. Numerical results obtained with the anisotropic interpolations of thermal conductivity and mass diffusivity are compared to the ones obtained using conventional isotropic formulations.

### 5.4.1 Thermal conductivity interpolation

#### Steady-state heat transfer

To demonstrate the importance of the anisotropic interpolation of the thermal conductivity in Eq. (4.41), I investigate a steady-state heat transfer scenario. The numerical validation test proposed by Nicoli et al. [77] is used and extended. Considering a square simulation domain defined as  $L_x = 1$  and  $L_y = 1$  in  $x$  and  $y$  directions, a temperature gradient  $\nabla T = -2$  is applied along the  $x$ -axis. The domain consists of a stationary disk-shaped solid grain with a radius  $R$  surrounded by an atmosphere region. A schematic of the simulation setup is given in Fig. 5.8a. For thermal conductivity ratio  $k_{at}/k_{ss} = 10$ , four cases of thermal conductivity interpolations are examined. I consider the form of interpolation utilized in current phase-field models of non-isothermal sintering [6, 36]. This interpolation form is similar to the formulation given in Eq. (4.43) and is hereafter referred to as the direct interpolation. Also, I consider another form of interpolation given in Ref. [112] to ensure heat flux conservation across the interface. This form of interpolation, hereafter referred to as the inverse interpolation, has its formulation as in Eq. (4.42). Moreover, an interpolation form proposed by Almgren [41] was used in Refs. [82] and [84] for their non-diagonal quantitative phase-field models. The interpolation thereafter called the special function (SF) interpolation is also examined

and can be expressed as

$$\frac{1}{k(\rho)} = \left( \frac{1}{2k_{ss}} + \frac{1}{2k_{at}} \right) + p_{sf}(\rho) \left( \frac{1}{2k_{ss}} - \frac{1}{2k_{at}} \right), \quad (5.7)$$

with

$$p_{sf}(\rho) = (2\rho - 1)[1 + 4a\rho(1 - \rho)], \quad (5.8)$$

where  $a \approx 0.90$  for  $k_{at}/k_{ss} = 10$ . Here, it is important to note that the formulation in Eq. (5.7) is adopted from Ref. [84] because  $\phi$  in Ref. [84] varies from 0 to 1 similar to  $\rho$ . Lastly, I consider the anisotropic form of thermal conductivity proposed in this thesis as expressed in Eq. (4.41). Abnormal interface effects are quantified by obtaining the average heat flux,  $J_{e,x}$  in the domain at  $x = 1$ . The plot of  $J_{e,x}$  against normalized interface widths  $l/R$  are presented in Fig. 5.8b for different interpolation forms. The black line in Fig. 5.8b indicates a reference case where no abnormal interface effect exists, i.e.  $J_{e,x}|_{l=0} = J_{e,x}|_{l>0}$ . Fig. 5.8c shows the temperature isolines across the free surface for the different interpolation forms. As shown in Fig. 5.8b, the direct and inverse interpolations show significant deviations from the reference case implying the deficit of these interpolation forms in eliminating interface effects. The SF interpolation also shows considerable deviation from the reference case. This deviation, which might be attributed to the nonmonotonic form of  $p_{sf}(\rho)$  [40] reinforces the limitation of the SF interpolation. On the other hand, the results using the anisotropic interpolation show very convincing agreement. The outstanding performance of the anisotropic form of interpolation necessitates its consideration for subsequent quantitative phase-field modeling. It is important to note that for common sintering scenarios, (an example is in Fig. 5.8c for  $k_{at}/k_{ss} = 0.2$ ), the SF interpolation might be utilized for quantitative simulations. The anisotropic form of interpolation, however, finds great importance in other processes where  $k_{at}/k_{ss}$  is higher such as the case studies in Ref. [113].

### Transient heat transfer

To further emphasize the importance of anisotropic thermal conductivity interpolation, a transient heat transfer scenario is simulated. A similar simulation setup to Fig. 5.8a is employed with the temperature in the solid grain set as 2 and the temperature in the atmosphere region set as 1. All boundaries are set to zero heat flux. A schematic of this setup is given in the inset of Fig. 5.9b. For thermal conductivity ratio  $k_{at}/k_{ss} = 0.01$ , the direct (Eq. (4.43)) and anisotropic (Eq. (4.41)) interpolations are examined and compared. Fig. 5.9 presents the temperature profiles across a chosen cross-section within the domain for both interpolation forms, considering different interface widths  $l$ . As observed in Fig. 5.9, the temperature profiles obtained using direct interpolation show

a significant dependence on the choice of interface width. However, the anisotropic interpolation maintains consistent temperature profiles across the domain even with increasing interface width. This implies that the anisotropic interpolation allows the use of larger interface widths in simulations without compromising quantitative accuracy.

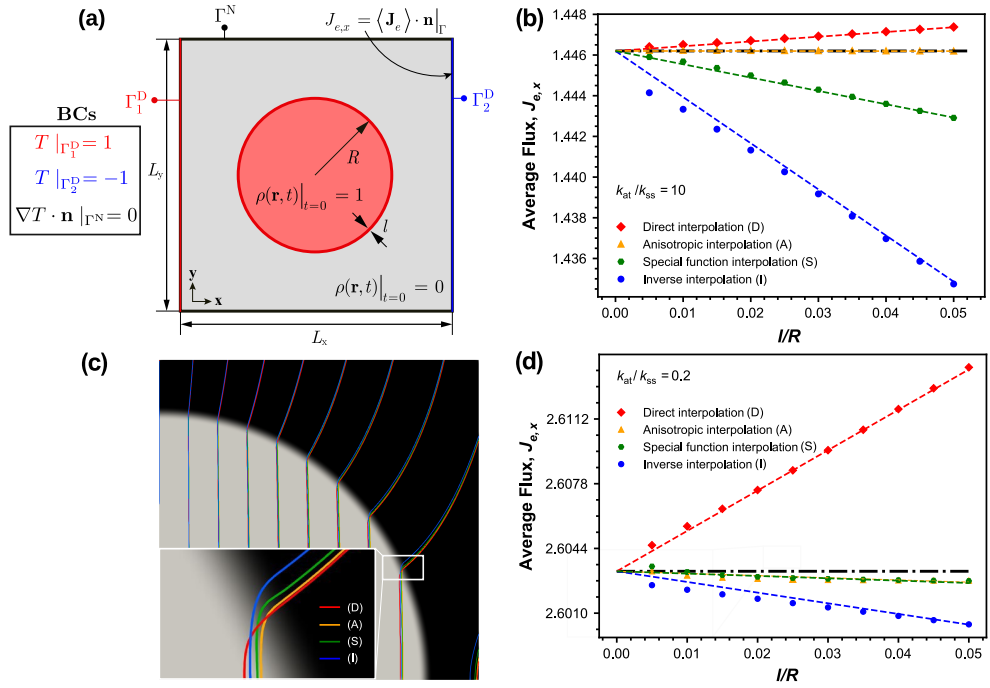


Figure 5.8: (a) Schematic of the simulation setup and boundary conditions used in the 2D simulation of steady state heat transfer.  $J_{e,x}$  (calculated on the denoted boundary) is also denoted (b) Comparison of  $J_{e,x}$  vs  $l/R$  for different thermal conductivity interpolations: direct interpolation (red diamonds), inverse interpolation (blue circles), special function interpolation (green hexagons) and anisotropic interpolation (orange triangles) for  $k_{at}/k_{ss} = 10$  where corresponding color lines are fitted simulation data lines and black dash-dot lines represent the plot of a case where no abnormal interface effects exist (c) Temperature isolines across the free surface for different thermal conductivity interpolations at  $l/R = 0.05$  (d) Comparison of  $J_{e,x}$  vs  $l/R$  for different thermal conductivity interpolations for  $k_{at}/k_{ss} = 0.2$ .



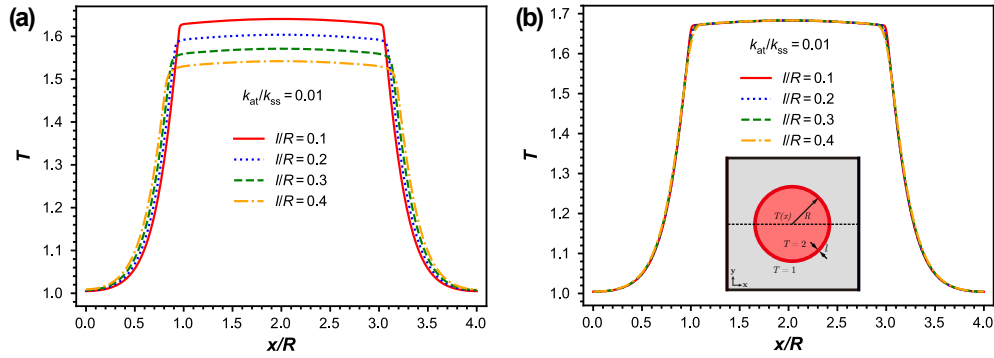


Figure 5.9: Comparison of the temperature profiles across the simulation domain for different interface widths and for (a) direct interpolation and (b) anisotropic interpolation of thermal conductivity. Inset in (b) is a schematic of the simulation setup and the cross-section where the temperature profile was taken.

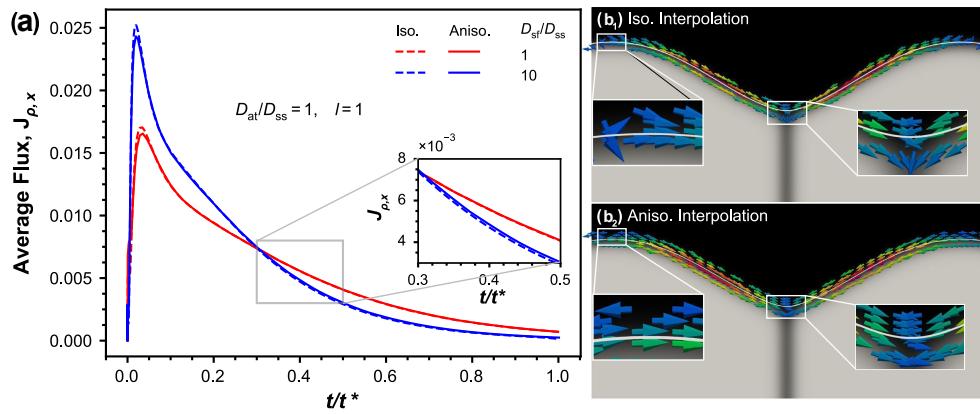


Figure 5.10: (a) Time evolution of  $J_{\rho,x}$  using different diffusivity interpolations: isotropic (dashdot lines), anisotropic (solid lines) for varied values of  $D_{\text{sf}}/D_{\text{ss}}$ . Local zooms around the neck of the grains using (b<sub>1</sub>) isotropic interpolation of diffusivity (b<sub>2</sub>) anisotropic interpolation of diffusivity.  $t^* = 14 \times 10^3$  units.

---

## 5.4.2 Mass diffusivity interpolation

Mass transfer during grain coalescence of two identical particles is considered in order to demonstrate the importance of anisotropic interpolation of mass diffusivity. A full schematic of the simulation setup is given in Fig. 5.3b. Numerical simulations are performed considering two different mass diffusivity interpolations. Comparisons are made between the anisotropic interpolation presented in this thesis, Eq. (4.50) and the conventional isotropic interpolation expressed as [27]

$$D = p_{ss}(\rho)D_{ss} + p_{at}(\rho)D_{at} + p_{sf}(\rho)D_{sf} + p_{gb}(\eta_i)D_{gb}, \quad (5.9)$$

where  $p_{ss}(\rho)$  and  $p_{at}(\rho)$  are interpolation functions valued as one only in the solid phase and atmosphere region respectively.  $p_{sf}(\rho)$  and  $p_{gb}(\rho)$  are interpolation functions valued as one only at the surface and grain boundary regions respectively. The average mass flux  $J_{\rho,x}$  is obtained across one of the grains, and the plots of  $J_{\rho,x}$  against normalized time  $t$  are shown in Fig. 5.10a.

The thin-interface limit analysis in Section 4.2 showed that eliminating chemical potential jump across the free surface does not require a specific mass diffusivity interpolation. Correspondingly, it has been derived in Refs. [114, 115] that the Cahn-Hilliard equation recovers the sharp-interface limit equation of motion for surface diffusion regardless of mass diffusivity form. Therefore, the  $J_{\rho,x}$  vs  $t$  curve is expected to be the same for both interpolations of mass diffusivity since theoretically no abnormal interface effect is related to the choice of diffusivity interpolation. However, as shown in Fig. 5.10a, there exist surprisingly numerical deviations of  $J_{\rho,x}$  when comparing the cases with isotropic and anisotropic mass diffusivity interpolations. These deviations can be explained by examining a close comparison of flux details at the free surface region. Fig. 5.10b<sub>1</sub> and Fig. 5.10b<sub>2</sub> show the calculated flux obtained using the isotropic and anisotropic diffusivity forms, respectively. It can be observed that the anisotropic form of diffusivity delivers a more reasonable description of the directions of the fluxes. Around the free surface in Fig. 5.10b<sub>1</sub> where isotropic diffusivity interpolation is used, there exist non-tangential fluxes at the free surface where only tangential fluxes are expected to contribute to surface diffusion. On the other hand, in Fig. 5.10b<sub>2</sub> where the anisotropic diffusivity form is used, only fluxes tangential to the free surface region exist to describe surface diffusion. Accordingly, it is imperative that, while thin-interface asymptotics confers no restriction on the diffusivity form as regards effecting quantitative simulations in mass diffusion, the anisotropic diffusivity form however makes it possible that the directions of fluxes are effectively described analogous to the sharp-interface description.

---

## 5.5 Numerical Analysis of Order Parameter Deviation

Within this section, results of the numerical analysis of the deviation of conserved OP  $\rho$  are presented considering different scenarios. Interface curvature dependency of the deviation is first demonstrated by comparing the steady-state profiles of  $\rho$  for circular and planar interface cases. Moreover, the theoretically obtained deviation of  $\rho$  in Eq. (4.13) is compared to the observed deviation in numerical simulations. In addition, an analysis of the deviation of  $\rho$  for an elliptical inclusion is presented.

### 5.5.1 Planar and Circular Interfaces

As obtained in the theoretical analysis of the deviation of  $\rho$  in Section 4.3, there exists a strong dependency of the deviation in bulk values of  $\rho$  on interface curvature. To demonstrate this, numerical results are presented for simple cases of planar and circular free surfaces between solid and atmosphere regions.

#### Curvature dependency

To analyze the curvature dependency of the deviation of  $\rho$ , a static planar free surface in a rectangular simulation domain with  $L_x = 60$  and  $L_y = 6$  is considered. On the other hand, a static circular free surface in a square simulation domain ( $L_x = 60$  and  $L_y = 60$ ) with radius  $R$  of the solid grain set to 15 is also considered. The initial values of  $\rho$  are set to be 1 and 0 in the solid and atmosphere regions respectively. A zero flux boundary condition is also imposed on all the edges of the simulation domains. The diffusive interface width of the free surface  $l$  is set to  $2\sqrt{2}$ . The simulation schematics are illustrated in Fig. 5.11.

The initial and final steady-state profiles of  $\rho(x)$  for both interface types are presented in Fig. 5.11. It can be observed that while the constant values of  $\rho$  in the bulk regions are maintained for the planar free surface (Fig. 5.11b), the final steady-state profile of  $\rho(x)$  for the curved free surface shows the deviation of  $\rho$  from 1 and 0 in the bulk regions (Fig. 5.11d). In addition, for the curved free surface, the area of the solid region is quantified and a comparison is made between the initial and final quantities. The change in area  $\Delta_A$  is obtained as  $-3.1\%$  indicating a shrinkage of the solid region.

The analysis above denotes that while the Cahn-Hilliard (CH) dynamics conserve mass in both regions in the case of a planar free surface, this is not the case when the free surface is curved. Yue et al. [102] remarked that the maintenance of the constant bulk values of the conserved OP in CH dynamics is dependent on the interface having

negligible volume compared to the bulk regions so that only the local free energy finds minimization. While this condition is viable for planar interfaces, it is not maintained for curved interfaces with concentrated energy at the interface. Therefore, the total free energy can be reduced by shrinking the area enclosed by the interface, which subsequently shifts the bulk values of the conserved OP due to the finite volume precept of CH dynamics.

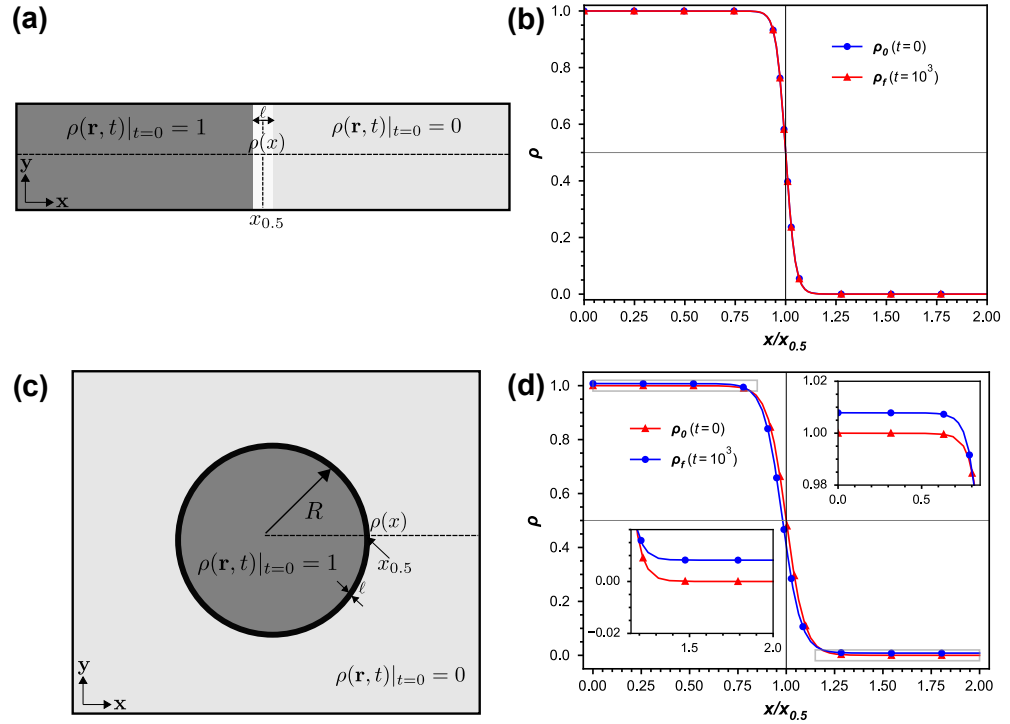


Figure 5.11: Schematic of the simulation setup used in the steady-state 2D simulation of (a) planar free surface and (c) circular free surface. Results of the initial and final steady-state profiles of  $\rho(x)$  for (b) planar free surface and (d) circular free surface.

### Comparison with theoretical results

The theoretically obtained deviation in Eq. (4.13) is compared to the observed  $\delta\rho$  in

numerical results. Employing the simulation schematic of the static circular free surface in Fig. 5.11c, the radius of the solid grain is set to  $R = 15$ , and a range of interface width  $l$  is considered. A comparison of the numerical and theoretical results of  $\delta\rho$  is presented in Fig. 5.12. The observed  $\delta\rho$  in the solid and atmosphere regions in the numerical results is respectively defined as  $\delta\rho_{ss} = \rho_{ss} - 1$  and  $\delta\rho_{at} = \rho_{at} - 1$  where  $\rho_{ss}$  and  $\rho_{at}$  are the observed values of  $\rho$  in the solid and atmosphere regions respectively. The average of  $\delta\rho_{ss}$  and  $\delta\rho_{at}$  is defined as  $\delta\rho_{avg}$ .

Fig. 5.12 shows a great agreement between theoretically obtained  $\delta\rho$  and numerically obtained  $\delta\rho_{ss}$ . As  $l$  increases, while  $\delta\rho_{ss}$  still fits very well with theoretically predicted  $\delta\rho$ ,  $\delta\rho_{at}$  tends to deviate from the theoretical results. Moreover, it can be observed that  $\delta\rho_{ss}$  and  $\delta\rho_{at}$  are similar for relatively smaller values of  $l$ . However, as  $l$  increases, there is a significant disparity in the values of  $\delta\rho_{ss}$  and  $\delta\rho_{at}$  which is contrary to the assumption of a single  $\delta\rho$  made in the theoretical analysis.

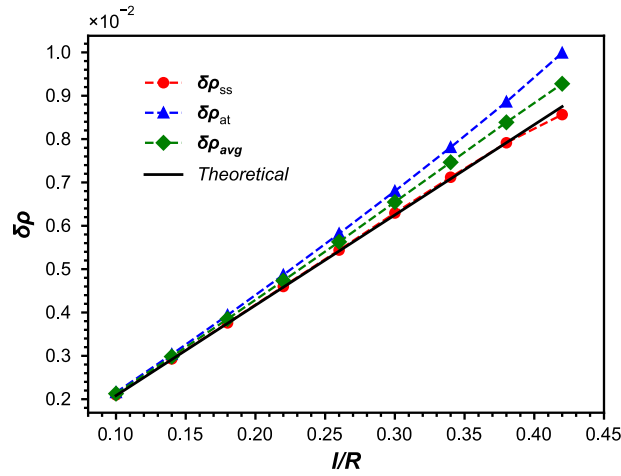


Figure 5.12: Comparison of the theoretical and numerical results of the deviation of  $\rho$ .  $\delta\rho_{ss}$  and  $\delta\rho_{at}$  respectively represent numerical results of the deviation of  $\rho$  in the solid and atmosphere regions.

---

## 5.5.2 Elliptical Interface

The numerical results of the deviated quantities of  $\rho$  in the elliptical free surface in Fig. 5.1a are presented and analyzed. The observed  $\delta\rho$  in the solid and atmosphere regions;  $\delta\rho_{ss}$  and  $\delta\rho_{at}$  are presented for cases when the solid grain is in elliptical and circular shapes. The tendencies of  $\delta\rho_{ss}$  and  $\delta\rho_{at}$  vs.  $l$  are respectively shown in Fig. 5.13a. Similar to previous results obtained for the circular free surface,  $\delta\rho_{ss}$  and  $\delta\rho_{at}$  increase with increasing  $l$ . When in the elliptical shape (implying a non-equilibrium condition),  $\delta\rho_{at} > \delta\rho_{ss}$  holds for almost every selected  $l$ , while  $\delta\rho_{ss} \approx \delta\rho_{at}$  when in the circular shape (implying an equilibrium condition). These differences can be attributed to the curvature dependency of the analytical profile of  $\rho$  [103]. It should be noted that  $\delta\rho_{ss}$  and  $\delta\rho_{at}$  exist even for symmetric mobilities with sufficiently large  $l$ , which is distinctive to the known interface effects (like trapping effects) that are incited by asymmetric kinetic mobilities.

As one of the significant outcomes, deviated bulk values of  $\rho$  incite deviated chemical potential  $\mu$  from its equilibrium ones in the bulk regions, which may result in the unexpected chemical potential drop as an extra driving force across the free surface. To examine this point, the deviated quantities of  $\mu$  are defined in a similar fashion as  $\delta\rho_{ss}$  and  $\delta\rho_{at}$ , i.e.,  $\delta\mu_{ss} = \mu_{ss}(\rho_{ss}) - \mu^{eq} = \mu_{ss}(\rho_{ss})$  and  $\delta\mu_{at} = \mu_{at}(\rho_{at}) - \mu_{at}^{eq} = \mu_{at}(\rho_{at})$ , noting that  $\mu_{ss}^{eq}(\rho_{ss} = 1) = \mu_{at}^{eq}(\rho_{at} = 0) = 0$ . In Fig. 5.13b, I present a similar tendency of  $\delta\mu_{ss}$  and  $\delta\mu_{at}$  vs.  $l$  when the particle is in the elliptical shape, where both  $\delta\mu_{ss}$  and  $\delta\mu_{at}$  grow along with increasing  $l$ .  $\delta\mu_{ss} > \delta\mu_{at}$  is depicted for every selected  $l$ , implying the existing chemical potential drop  $\Delta\mu = \delta\mu_{at} - \delta\mu_{ss} > 0$  across the free surface at the semi-major axis, as shown in Fig. 5.14a. Notably, when the particle is in the circular shape,  $\delta\mu_{ss} = \delta\mu_{at}$  is formed without the dependency of  $l$ , indicating no chemical potential drop across the free surface, i.e.,  $\Delta\mu = \delta\mu_{at} - \delta\mu_{ss} = 0$  as shown in Fig. 5.14b. This also demonstrates that the existing deviation in  $\mu$  incited by  $\delta\rho_{ss}$  and  $\delta\rho_{at}$  does not affect the supposing equilibrium condition, as the particle stops morphing in the circular shape.

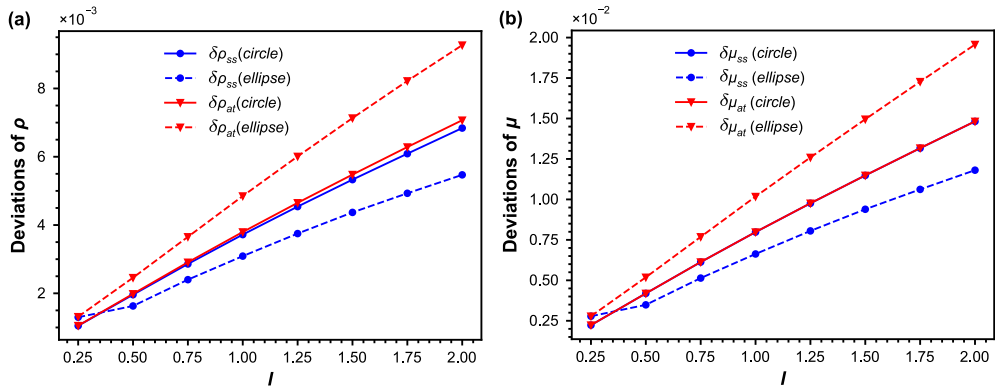


Figure 5.13: The deviated bulk values of (a)  $\rho$  and (b)  $\mu$  with respect to the diffuse interface width  $l$ . The deviated bulk values are read from the numerical results presented in Fig. 5.1a.

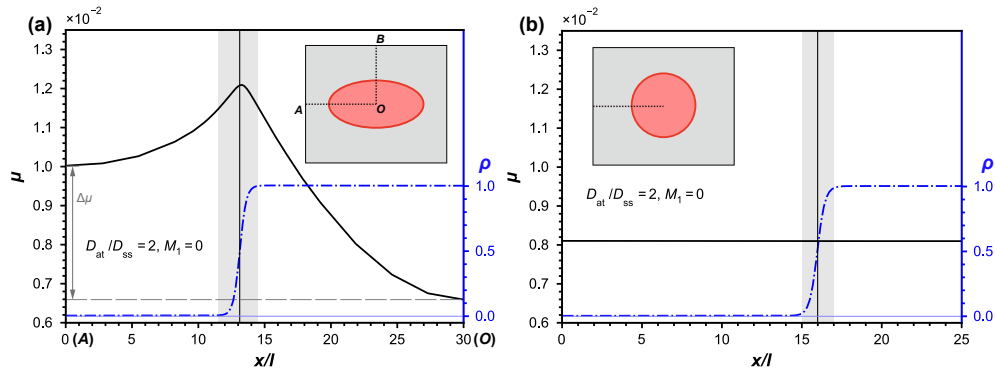


Figure 5.14: Chemical potential profile across the free surface: (a) profile from A to O; (c) profile at equilibrium. The diffuse interface width  $l = 1$ .





---

## 6 Variational Quantitative Phase-field Simulations of Non-conventional Sintering

---

Based on the verification of the variational quantitative phase-field model in Chapter 5, this chapter presents 3D simulations of yttria-stabilized zirconia (YSZ) micro-particles to demonstrate the applicability of the model in realistic scenarios. The chapter is structured as follows. Section 6.1 provides a detailed description of the simulation setup, including material properties and model parameters used for the simulations. Moreover, the results of isothermal sintering simulations are presented in Section 6.2. It presents the evolution of the microstructure, the relative density profiles, and compares the results obtained from the quantitative model with those from the conventional non-quantitative model. In addition, non-isothermal sintering simulations are also performed. Section 6.3 presents the results of non-isothermal simulations, including the transient thermo-microstructure profiles and segmental average temperature across the simulation domain.

### 6.1 General Simulation Set-up

Fig. 6.1a illustrates the general setup for the 3D simulations of YSZ micro-particles sintering. A cubic domain with dimensions of  $100 \times 100 \times 100 \mu\text{m}^3$  is used for all simulations. Moreover, the simulation domain is subjected to an initial temperature gradient  $\nabla T = g_0$  along the  $x$ -axis to adopt non-isothermal conditions. Additionally, a no-flux boundary condition is imposed on the mass transfer time evolution equation for all domain boundaries, implying no net transfer of mass across these boundaries. The normalized material properties for YSZ particles sintered in an argon atmosphere are adopted from Ref. [6] and are presented in Table 6.1. Simulations were conducted

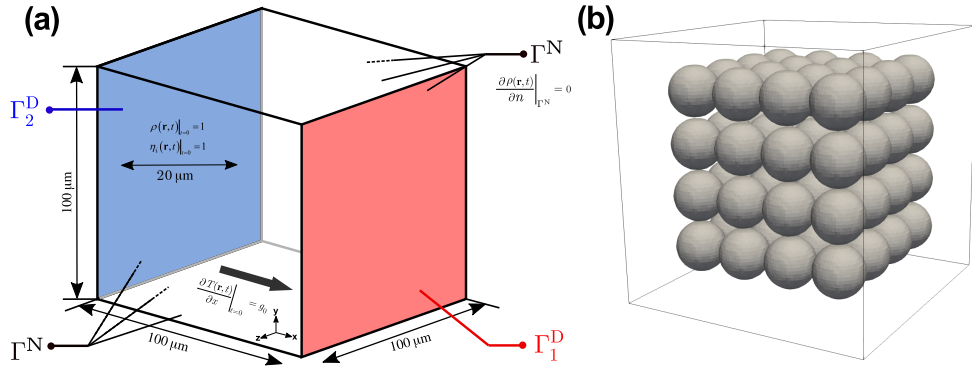


Figure 6.1: (a) Schematic of the initial and boundary conditions used in the 3D simulations of the sintering of yttria-stabilized zirconia (YSZ) micro-particles. The size of the simulation domain is also denoted; (b) Initial packing of 64 uniformly sized spherical particles in the simulation domain.

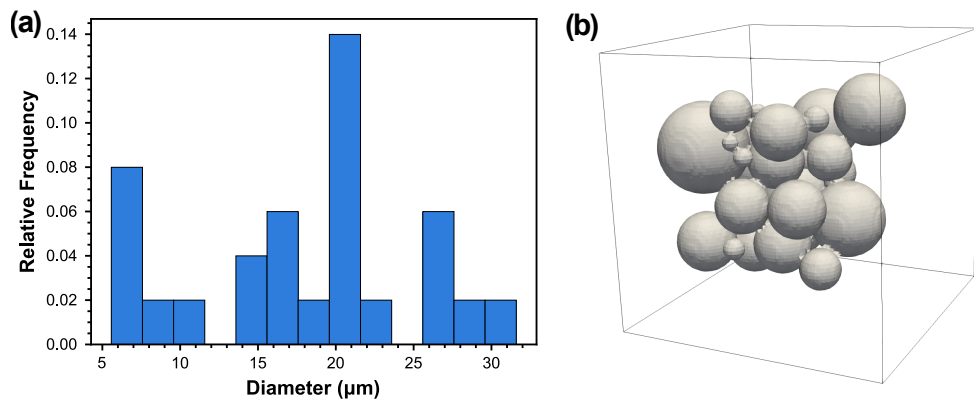


Figure 6.2: (a) Particle size distribution employed for the sintering simulation of the non-uniformly sized YSZ particles. Average diameter  $\bar{d}$  is 20 μm and standard deviation  $s_d$  is 10 μm; (b) Initial packing of 27 non-uniformly sized spherical particles in the simulation domain.

using both uniformly and non-uniformly sized spherical particles. For uniformly sized distribution, 64 identical particles, each with a diameter of 20 μm, were placed within the simulation domain. The packing of the particles is shown in Fig. 6.1b. Another set of

Table 6.1: Set of dimensionless quantities and normalized model parameters employed for 3D simulations of YSZ micro-particles [6].

$k_{\text{at}}$	$k_{\text{ss}}$	$D_{\text{ss}}$	$D_{\text{sf}}$	$D_{\text{gb}}$	$L_{\eta,\text{gb}}$
$1.40 \times 10^{10}$	$4.66 \times 10^{11}$	$4.91 \times 10^{-7}$	20	0.297	10
$c_{\text{r}}$	$\underline{C}$	$\underline{D}$	$\kappa_{\rho}$	$\kappa_{\eta}$	
830	1	0.062	0.531	0.185	

simulations involved the non-uniform distribution of particles. Here, 27 particles were packed within the domain using the Discrete Element Method (DEM) software GeoDict, employing the grain piling module, GrainGeo. The resulting particle size distribution and initial packing are shown in Fig. 6.2.

Maintaining the unique orientation of each particle during simulations requires a non-conserved order parameter (OP)  $\eta_i$  for every particle [36, 116, 117]. However, for 64 particles in Fig. 6.1b, this implies 64 non-conserved OPs  $\{\eta_i\}$  which is computationally expensive. Also, since only a few of the OPs are nonzero at any given point, the detailed representation of  $\{\eta_i\}$  is relatively non-essential [36]. To address this challenge, the Welsh-Powell and grain tracking algorithm [118] is applied to the particles' network to optimize the total number of  $\{\eta_i\}$  and thus reduce the computational cost. The algorithm assigns the same  $\eta_i$  to particles that are sufficiently spaced and remap the total  $\{\eta_i\}$  if particles with similar  $\{\eta_i\}$  approach coalescence [36]. Fig. 6.3a depicts the adjacency matrix, illustrating the neighboring particles for each of the 64 particles. The criterion of adjacency is taken as the distance between the largest particle and its nearest neighbor. Also, the coloring map obtained based on the adjacency matrix is presented in Fig. 6.3b. Based on this optimization, twelve  $\{\eta_i\}$  were sufficient to represent the 64 particles in the simulation, enhancing computational efficiency. For simulations conducted for the 27 non-uniformly sized particles in Fig. 6.2b, seven  $\{\eta_i\}$  were sufficient.

## 6.2 Isothermal Simulations

This section presents the numerical simulation results for the isothermal sintering of YSZ particles. To adopt an isothermal scenario, the temperature gradient  $\nabla T$  along the x-axis is set to zero thus neglecting temperature-related effects. This isothermal scenario allows a distinct investigation of mass transfer in sintering using a quantitative

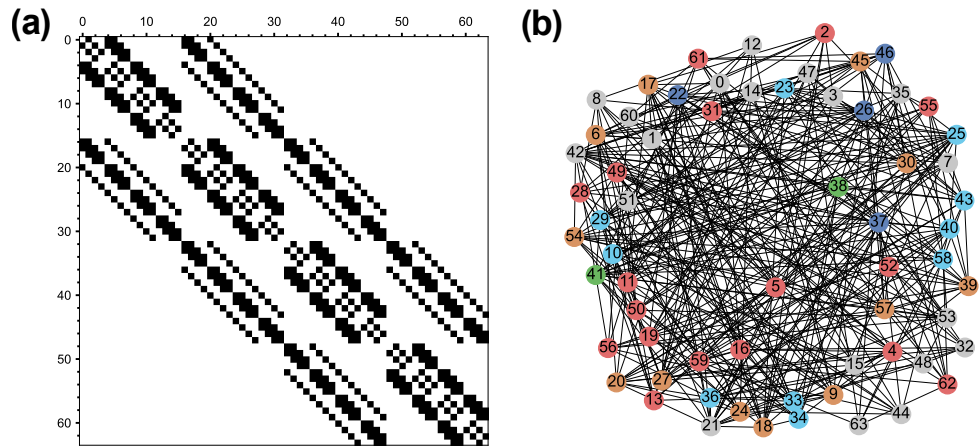


Figure 6.3: (a) Adjacency matrix of the powder particles; (b) Coloring map generated by adjacency matrix in (a).

phase-field model. The transient microstructure of the sintering process for the uniformly sized and non-uniformly sized particle configuration is first presented in this section. Subsequently, the nominative density distribution profiles with comparisons between the quantitative phase-field model and the non-quantitative conventional model are presented.

## 6.2.1 Transient microstructure

### Uniformly sized particles

Fig. 6.4 shows the transient evolution of the YSZ microstructure during the 3D sintering simulations of the uniformly sized particles in Fig. 6.1b. Transient structures are presented at three distinct time points for the isosurface value of  $\rho \geq 0.5$ . To further illustrate the transient microstructure changes, Fig. 6.4b shows the distribution of the particles at the cross-section  $x = 50 \mu\text{m}$ .

As observed in Fig. 6.4, the sintering process starts with the particles forming necks between one another, followed by further densification of the particles' mass. At the onset of the sintering process in Figs. 6.4a<sub>1</sub> and 6.4b<sub>1</sub>, the points where the particles make contacts transform into sintering necks. These necks subsequently grow and

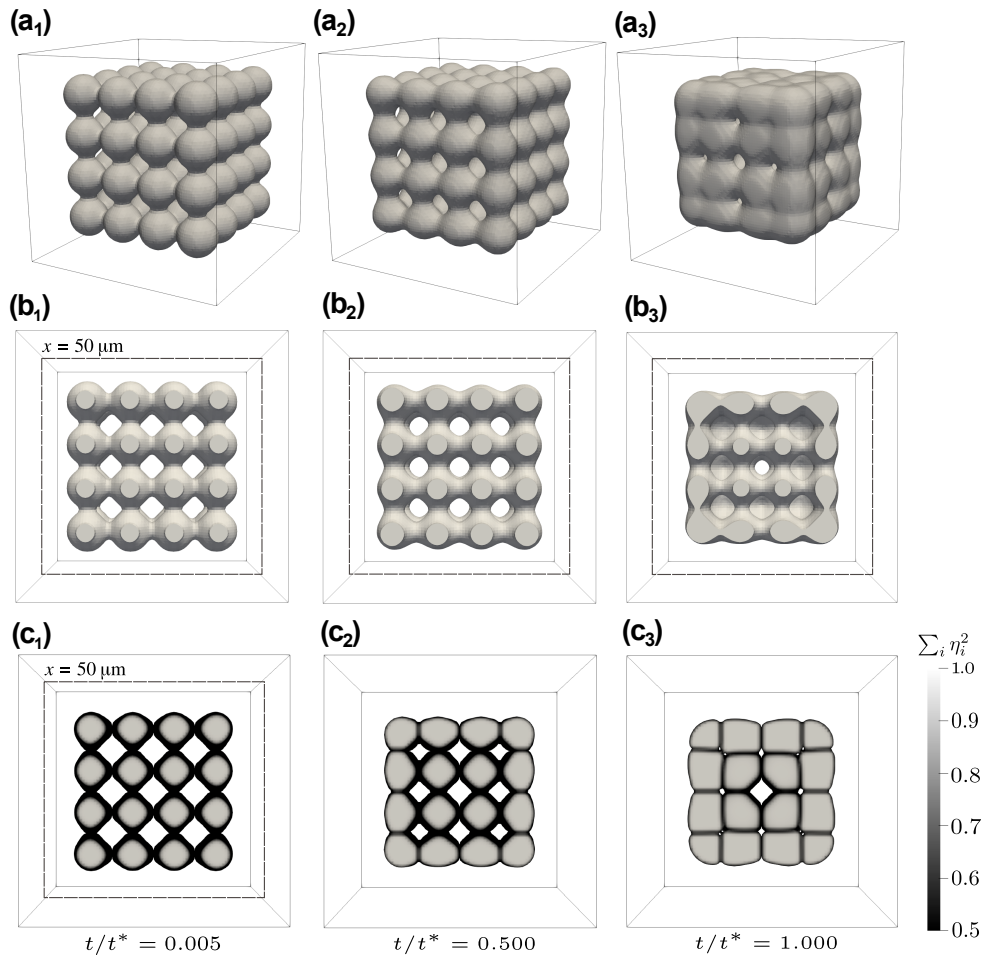


Figure 6.4: (a) Microstructure evolution of the particles sintered using the simulation setup in Fig. 6.1; (b) Evolution of the microstructure cross-section at  $x = 50 \mu\text{m}$ ; (c) Evolution of the microstructure cross-section showing the grain boundaries. The dimensionless end time is  $t^* = 200$  units.

develop into grain boundaries between neighboring particles as sintering progresses (Fig. 6.4b<sub>2</sub>). Furthermore, it can be seen in Fig. 6.4b<sub>2</sub> that the size of the pores is

gradually reduced at this stage indicating the onset of the densification process. Toward the end of the sintering process, densification continues with the continuous elimination of the pores. Figs. 6.4a<sub>3</sub> and 6.4b<sub>3</sub> show the eventual reduction in the volume of the pore region. Also, it can be seen that during densification, the densified particles' mass is drawn toward the overall center.

### Non-uniformly sized particles

Fig. 6.5a shows the snapshots of the transient evolution of the YSZ microstructure during the 3D sintering simulation of non-uniformly sized particles. The figure depicts morphological changes in particle structure over time. Additionally, Fig. 6.5b shows the particle distribution at a specific cross-section  $x = 50 \mu\text{m}$  within the simulation domain.

Similar to the observations in uniformly sized particle simulations, the sintering process begins with the formation of necks between particles. Afterward, these necks evolve in size with subsequent reduction in the pore size. At this stage, densification of the entire structure starts. As shown in Fig. 6.5b, smaller particles are gradually eliminated, contributing to the densification process whereby the entire structure is transformed into a denser mass.

## 6.2.2 Segment-wise density distribution

Fig. 6.6a presents the nominative density distribution along the  $x$ -direction obtained from the uniformly sized particle simulations in Fig. 6.4. Obtaining the distribution of the segment-wise density is preferred as the total density within the simulation domain remains constant throughout simulations. All segments are selected with the same volume,  $\Omega_{\text{seg}} = 2 \times 100 \times 100 \mu\text{m}^3$  without any overlapping as shown in the inset of Fig. 6.6a. For each segment, the nominative density is calculated as

$$\bar{\rho}_n = \left( \int_{\Omega_{\text{seg}}} \rho \, d\Omega \right) / \Omega_{\text{seg}}. \quad (6.1)$$

Moreover, Fig. 6.6b shows the time evolution of the density of the segment at the cross-section  $x = 50 - 60 \mu\text{m}$ . The density profiles in Fig. 6.6 are compared for two models: the proposed quantitative model where antitrapping terms are taken into account (*model with ATs*) and the conventional model where these terms are not considered (*model without ATs*). This comparison is done to examine the significance of the quantitative validity of the sintering model as regards the sintering of realistic scenarios.

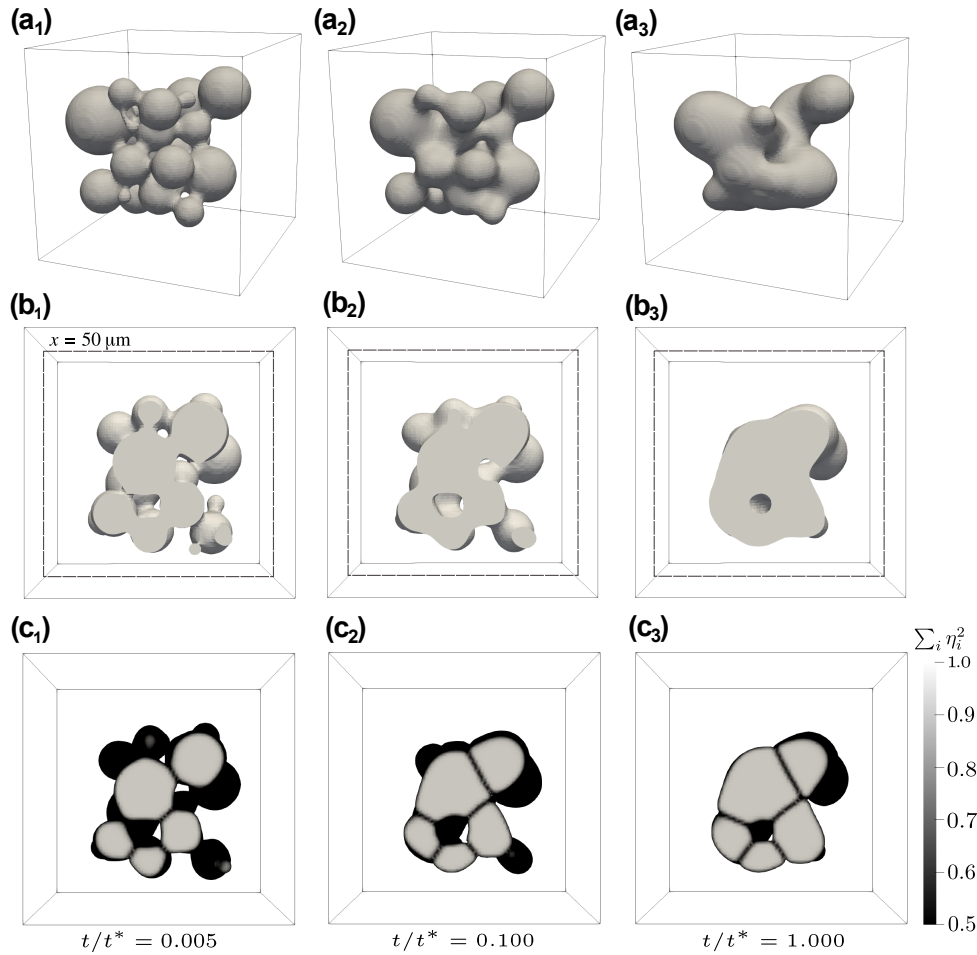


Figure 6.5: (a) Microstructure evolution of the sintered non-uniform particles; (b) Evolution of the microstructure cross-section at  $x = 50 \mu\text{m}$ ; (c) Evolution of the microstructure cross-section showing the grain boundaries. The dimensionless end time is  $t^* = 200$  units.

As observed in Fig. 6.6, there exist relatively minimal differences between the density distribution and profiles obtained using both models. A possible reason for this stems

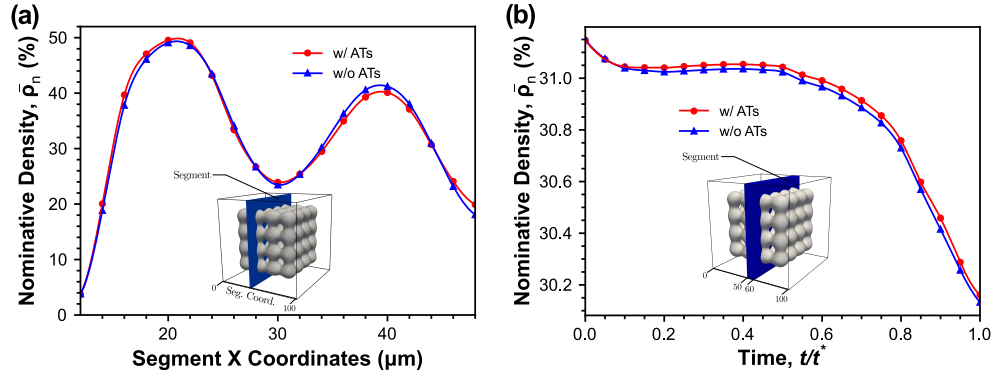


Figure 6.6: (a) Segment-wise density distribution of the sintered particles mass along the  $x$ -direction at the simulation end time  $t^*$ . The distribution is obtained up to  $x = 50 \mu\text{m}$  due to symmetry; (b) Time evolution of the density of the segment at  $x = 50 - 60 \mu\text{m}$ . Comparison is made between the quantitative model (with ATs) and the non-quantitative model (without ATs). The dimensionless end time of the simulation is  $t^* = 200$  units.

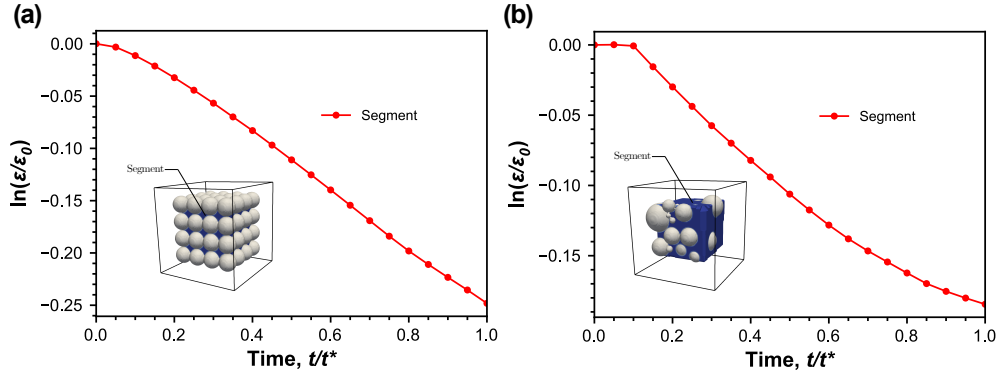


Figure 6.7: Temporal evolution of  $\ln(\epsilon/\epsilon_0)$  for the indicated segment for the sintered (a) uniform particles; (b) non-uniform particles. The segment size is  $60 \times 60 \times 60 \mu\text{m}^3$ . The dimensionless end time of the simulation is  $t^* = 200$  units.

from the fact that the mass transfer antitrapping term ( $M_1$  in Eq. (4.55)) introduced in the quantitative model depends not just on the symmetry of bulk diffusivities but



---

also on their values. As seen in Table 6.1, the bulk diffusivities of YSZ material are of a significant order lower than the surface diffusivity. Consequently, mass transfer during the sintering process is largely governed by surface diffusion with minimal contribution from bulk diffusion. Therefore, the abnormal interface effects caused by bulk diffusion, which the antitrapping term is formulated to eliminate, are not largely significant in this case.

Furthermore, it was proposed in Ref. [119] that the evolution of porosity during the densification process of sintered material follows the first-order kinetics law such as

$$\dot{\epsilon} = -k\epsilon, \quad (6.2)$$

where  $\epsilon$  is porosity,  $k$  is the sintering rate constant and  $\epsilon_0$  is the initial porosity. In Fig. 6.7, the temporal evolution of  $\ln(\epsilon/\epsilon_0)$  for a segment of the sintered particles are presented for both uniform particles and non-uniform particles. It can be observed that  $\ln(\epsilon/\epsilon_0)$  of the selected segments presents an approximate linear trend for both particle distributions. This shows that Eq. (6.2) is valid in the proposed model to describe the porosity evolution of the particles.

## 6.3 Non-isothermal Simulations

The numerical simulation results obtained for the non-isothermal sintering of YSZ particles are presented in this section. The temperature gradient  $\nabla T = g_0$  along the  $x$ -axis is set to  $10 \text{ K } \mu\text{m}^{-1}$ . Results of transient temperature profiles across the simulation domain are presented followed by segmental average temperature distribution. The temperature profiles and average temperature distribution are compared between the quantitative model where antitrapping terms are taken into account (*model with ATs*) and the conventional non-quantitative model where these terms are not considered (*model without ATs*).

### 6.3.1 Transient temperature profiles

Figs. 6.8 and 6.9 show the evolution of the temperature field across the simulation domain for the uniformly sized and non-uniformly sized particle configuration respectively. Results are presented and compared between the quantitative model and the conventional non-quantitative model.

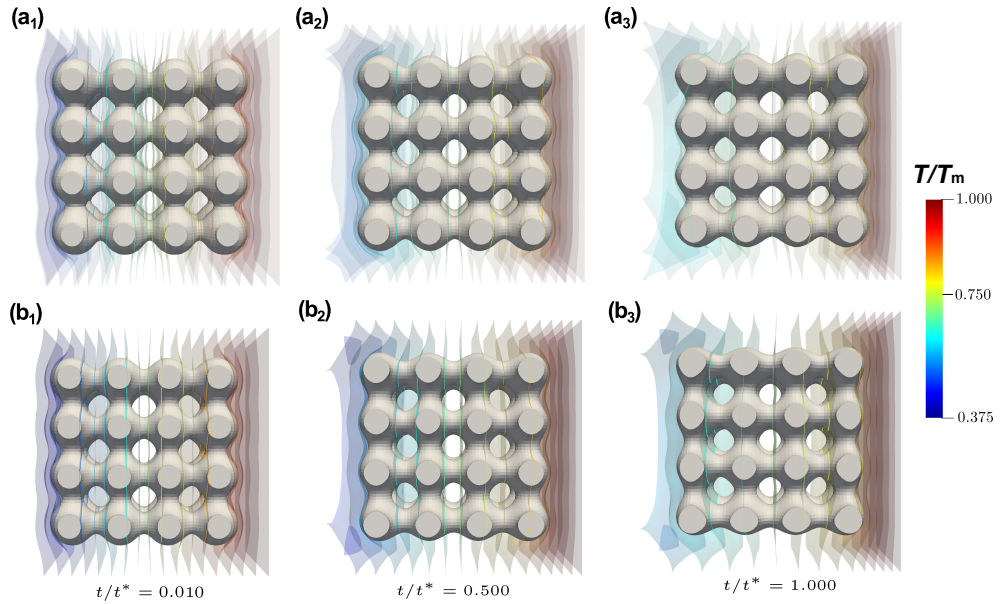


Figure 6.8: Evolution of thermo-microstructure for non-isothermal simulations of uniformly sized particles for the mid-section ( $z = 50 \mu\text{m}$ ) along the direction of the given  $\nabla T$ . The isotherms of temperature are indicated at the corresponding time point for (a) non-quantitative conventional model ; (b) quantitative model.  $T_M$  is  $1600\text{K}$ . The dimensionless end time of the simulation is  $t^* = 60$  units.

As observed in both figures, the predicted isotherms for both models are different at similar time points. The transient temperature profiles comparing both models show that heat transfer across the simulation domain is faster in the non-quantitative model compared to the quantitative model. As discussed in Section 5.3.1, these differences can be attributed to the presence of abnormal interface effects in the conventional model which are eliminated in the quantitative model.

### 6.3.2 Segment-wise temperature distribution

Fig. 6.10a presents the distribution of the sectional average temperature along the direction of the applied temperature gradient obtained from the simulations in Fig. 6.8.

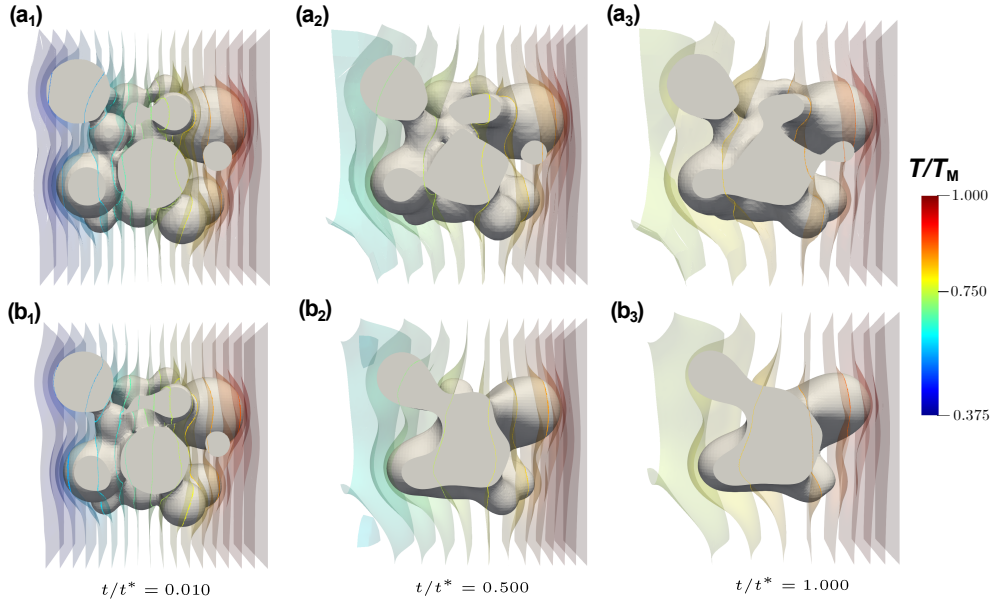


Figure 6.9: Evolution of thermo-microstructure for non-isothermal simulations of non-uniformly sized particles for the mid-section ( $z = 50 \mu\text{m}$ ) along the direction of the given  $\nabla T$ . The isotherms of temperature are indicated at the corresponding time point for (a) non-quantitative conventional model ; (b) quantitative model.  $T_M$  is 1600K. The dimensionless end time of the simulation is  $t^* = 60$  units.

Furthermore, Fig. 6.10b shows the time evolution of the average temperature of the segment at the cross-section  $x = 50 \mu\text{m}$ . All segments are selected with the same volume,  $\Omega_{\text{seg}} = 2 \times 100 \times 100 \mu\text{m}^3$  without any overlapping as shown in the inset of Fig. 6.10. The average temperature for each segment is obtained as

$$\bar{T}_{\text{seg}} = \left( \int_{\Omega_{\text{seg}}} T \rho \, d\Omega \right) / \Omega_{\text{seg}}. \quad (6.3)$$

The average temperature profiles in Fig. 6.10 are also compared between the quantitative model and the conventional non-quantitative model.

The results presented in Fig. 6.10 show substantial differences between the temperature profiles obtained for both models. Heat transfer across the simulation domain is faster in

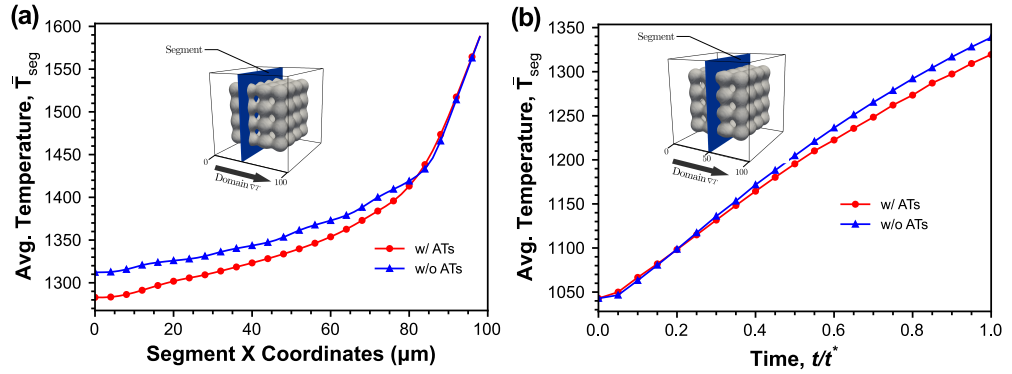


Figure 6.10: (a) Segment-wise average temperature distribution in the simulation domain along the direction of the applied  $\nabla T$  at the simulation end time  $t^*$ ; (b) Time evolution of the average temperature of the segment at  $x = 50 \mu\text{m}$ . Comparison is made between the quantitative model (with ATs) and the non-quantitative model (without ATs). The dimensionless end time of the simulation is  $t^* = 60$  units.

the non-quantitative model compared to the quantitative model. As seen in Fig. 6.10a, the values of the predicted segmental average temperature across the domain were higher for the non-quantitative model at the simulation end time.

Moreover, Fig. 6.10b demonstrates that the differences in the average temperature of the segments between the models become more pronounced with increasing simulation time. These differences can be attributed to the presence of abnormal interface effects in the conventional model, as discussed in Section 5.3.1. These effects emerge at the free surfaces of solid particles and serve as additional driving forces that enhance heat transfer. The quantitative model with antitrapping terms is specifically formulated to eliminate these abnormal effects, resulting in a slower observed heat transfer rate across the domain.

---

## 7 Conclusion and Outlook

---

### 7.1 Conclusion

Sintering, a widely used manufacturing process typically involves the compaction of powder particles using the direct application of heat and pressure. However, novel techniques generally called "unconventional sintering" have been developed in recent times. These techniques include selective laser sintering, spark plasma sintering, flash sintering, and microwave sintering where powder compaction is achieved using treatments other than direct heat or pressure. While unconventional sintering techniques offer advantages like higher heating rates and better efficiency, their heating mechanisms bring about a range of complexities. These techniques involve an interplay of non-isothermal factors, including heating/cooling rate and temperature inhomogeneity, alongside conventional factors like powder composition, powder size, atmosphere, and pressure. Understanding the relationship between these factors and the various physical effects involved in sintering is essential. This necessitates the development of a framework linking sintering process parameters, microstructure, and properties of sintered materials.

Numerical modeling and simulation provide a better approach to understanding microstructure and property relationships in sintering processes compared to traditional trial-and-error experiments. Simulations provide a fundamental understanding of the mechanisms of sintering and their impact on the resulting microstructure and properties of sintered products. A popular numerical technique for investigating microstructure evolution and the intricate multi-physics in sintering is the variational phase-field method. This method allows the simulation of microstructure evolution without explicitly tracking the interfaces. It has been successfully applied to both isothermal [26, 27, 34, 35] and non-isothermal scenarios [6, 36, 37].

However, a major challenge for variational phase-field models is their quantitative validity for diffusive processes like mass and heat transfer. This limits their applicability in quantitative modeling and simulation of realistic sintering scenarios. Due to the diffusive-interface feature of phase-field models, they need to be projected onto associated sharp-

---

interface models to ascertain quantitative validity. Nevertheless, this is not the case for typical models. During simulations, abnormal interface effects can emerge, such as trapping effects and violation of conservation laws. These effects become more significant when neighboring phases exhibit considerable asymmetries in kinetic properties or when larger interface widths are employed. The introduction of the *antitrapping current* in the diffusion equation has been proposed and often applied to eliminate these effects [44, 47, 48]. However, this method breaks the thermodynamics variational nature of phase-field models. While variational quantitative phase-field models have been developed for solidification cases [38, 40, 50], no such work has addressed the interfaces in non-isothermal sintering, where free surfaces between the solid phase and surrounding pores exhibit strong asymmetries in mass and thermal properties.

This study introduces a variational quantitative phase-field model for non-isothermal sintering processes. The model is developed based on the non-diagonal phase-field approach presented in Refs. [49, 50]. It is formulated to eliminate abnormal interface effects emerging from the diffuse-interface description of the free surfaces of the solid. Moreover, model formulations are obtained using a variational framework thus ensuring thermodynamic consistency. A major distinction between the proposed model and the conventional ones involves the consideration of cross-coupling terms between conserved kinetics (mass and heat transfer) and non-conserved kinetics (grain growth). These terms, parametrized by functions  $M_1$  and  $M_2$ , are similar to *antitrapping current* in traditional quantitative phase-field models and are essential for the quantitative description of the model. Also, the explicit formulations of  $M_1$  and  $M_2$  are derived in terms of the model parameters using an asymptotic analysis procedure introduced in Ref. [50]. Furthermore, anisotropic interpolations of mass and energy mobilities across the free surfaces are proposed. Employing this interpolation scheme is essential to ascertain the full elimination of abnormal interface effects.

Numerical tests were performed to highlight the importance of the introduced cross-coupling terms. The results show the emergence of interface effects, namely chemical potential jump ( $\delta\mu$ ) and temperature jump ( $\delta T$ ), at the free surface in the conventional non-isothermal model ( $M_1 = 0$  and  $M_2 = 0$ ). These non-zero jumps ( $\delta\mu \neq 0$  and  $\delta T \neq 0$ ) negate the assumptions inherent to the sharp-interface description of non-isothermal sintering. Furthermore, numerical results show that employing  $M_1 \neq 0$  and  $M_2 \neq 0$  as described in the proposed quantitative model eliminates these jumps. In addition, the convergence behavior of  $\delta\mu$  with respect to interface width ( $l$ ) was compared between the models with and without  $M_1$ . Both models showed  $\delta\mu \rightarrow 0$  as  $l \rightarrow 0$  indicating their accuracy for relatively small interface widths. The key advantage of the quantitative model becomes evident for larger interface width,  $l \gg 0$ . In this regime, the model

---

with  $M_1 = 0$  presents a significantly larger chemical potential jump  $\delta\mu$  compared to the model with  $M_1 \neq 0$ . This highlights the importance of the cross-coupling terms for achieving quantitative validity, particularly in cases with larger interface widths.

This study further examined the differences in transient microstructure and temperature profiles between the conventional and proposed models. The results demonstrate that the cross-coupling terms in the proposed model effectively eliminate the artificial driving forces brought about by non-zero chemical potential ( $\delta\mu$ ) and temperature ( $\delta T$ ) jumps at the free surface. Moreover, cross-coupling terms were shown to only modify the sintering kinetics with no impact on thermodynamic conditions. Additionally, the proposed anisotropic interpolation of kinetic mobilities was evaluated numerically and compared to other existing schemes. It was observed that, unlike other schemes, the proposed scheme delivers an effective description of diffusion fluxes comparable to the sharp-interface description. The above-mentioned results validate the proposed model as a powerful tool for investigating quantitative simulations of non-isothermal sintering and similar solid-state processes.

Furthermore, numerical 3D simulations of more realistic cases were considered. In particular, the sintering of YSZ micro-particles was performed considering both isothermal and non-isothermal scenarios. The results show minimal differences in the density distribution profiles predicted by the quantitative and non-quantitative models. This can be attributed to the fact that the sintering of YSZ material is largely governed by surface diffusion with minimal contribution from bulk diffusion. As the mass transfer cross-coupling term  $M_1$  mainly depends on the bulk diffusivity, its impact on density evolution is negligible for this material. Consequently, the abnormal interface effects associated with bulk diffusion, which the cross-coupling term aims to eliminate, have minimal influence in this scenario. On the other hand, significant differences emerged in the temperature profiles across the simulation domain for an applied temperature gradient ( $\nabla T$ ). The conventional model without cross-coupling terms shows faster heat transfer compared to the quantitative model. This disparity stems from the presence of abnormal interface effects in the conventional model. These effects emerge at the free surfaces of solid particles and serve as additional driving forces for heat transfer. The quantitative model, formulated to eliminate these effects through cross-coupling terms, predicts a slower heat transfer rate across the domain. The results for the realistic scenarios demonstrate the applicability of the proposed model for quantitative simulations of the non-isothermal sintering process.

---

## 7.2 Outlook

The developed model offers a powerful framework for quantitative modeling and simulations of non-isothermal sintering and similar processes. However, extending its applicability to quantitative modeling and simulations of complex additive manufacturing techniques like powder bed fusion (PBF) necessitates further model developments. A full non-isothermal model for the PBF process requires the consideration of different phenomena such as mass transfer, heat transfer, grain growth, solidification, and melt dynamics. Consequently, a quantitative phase-field model for PBF would necessitate the elimination of the diffusive interface effects associated with these phenomena. The developed model in this study solely considers mass transfer, heat transfer, and grain growth hence its applicability is limited to non-isothermal sintering and similar solid-state processes. Accordingly, future work on this would therefore focus on ensuring the quantitative validity of solidification coupled with melt dynamics in PBF. Based on the concepts presented in this study, the development of a quantitative phase-field model for the PBF process will be formulated to eliminate artificial interface effects while also ensuring thermodynamic consistency.

This study evaluated the quantitative validity of the model using diffusion-driven re-shaping simulations. A major outlook would be to obtain additional model verification results using other benchmark simulations. Developing and implementing additional benchmark simulations is essential to demonstrate the importance of the proposed cross-coupling terms for achieving quantitative validity. In particular, these benchmarks could involve obtaining the convergence of free surface velocity with respect to interface width. However, a key challenge in the investigation of the free surface velocity lies in the representation of the free surface with a conserved field. The movement of the free surface with a defined velocity (prescribed flux) can potentially violate the conservation law associated with the conserved field. Future efforts need to address this challenge to obtain accurate free surface velocity investigations.

Moreover, the results obtained from this study show an additional interface effect specific to the conserved field governed by Cahn-Hilliard dynamics in phase-field modeling. This effect involves the deviation of the conserved field from its equilibrium values in the bulk regions of the domain. The theoretical and numerical analysis of this deviation is given in this study. It is important to note that, unlike other well-known abnormal interface effects, this deviation depends solely on the interface width and curvature, and not on kinetic properties. One promising outlook is the formulation of a quantitative model that takes into account this deviation and potentially eliminates its influence on simulation results.



---

## Bibliography

---

- [1] FM Pinto, RC Silva, and FA La Porta. “Overview of conventional and unconventional sintering methods”. In: *Green Sustainable Process for Chemical and Environmental Engineering and Science*. Elsevier, 2021, pp. 15–35.
- [2] Volodymyr Shatokha. *Sintering: Methods and products*. BoD–Books on Demand, 2012.
- [3] Mohamed N Rahaman. *Ceramic processing and sintering*. Vol. 1. CRC press, 2017.
- [4] Sudipta Biswas et al. “A study of the evolution of microstructure and consolidation kinetics during sintering using a phase field modeling based approach”. In: *Extreme Mechanics Letters* 7 (2016), pp. 78–89.
- [5] Abhishek Indurkar et al. “Advances in sintering techniques for calcium phosphates ceramics”. In: *Materials* 14.20 (2021), p. 6133.
- [6] Yangyiwei Yang et al. “Investigation on temperature-gradient-driven effects in unconventional sintering via non-isothermal phase-field simulation”. In: *Scripta Materialia* 186 (2020), pp. 152–157.
- [7] Amparo Borrell and Maria Dolores Salvador. “Advanced Ceramic Materials Sintered by Microwave Technology”. In: *Sintering Technology*. Ed. by Malin Liu. Rijeka: IntechOpen, 2018. Chap. 1.
- [8] Munir Z.A., Anselmi-Tamburini U., and Ohyanagi M. “The effect of electric field and pressure on the synthesis and consolidation of materials: A review of the spark plasma sintering method.” In: *Journal of Materials Science* 41 (2006), 763–777.
- [9] Zoran S Nikolic, Ivona Mitrovic, and Vojislav V Mitic. “Computer Simulation of Neck Growth During Sintering Process”. In: *Advanced Science and Technology of Sintering* (1999), pp. 61–66.

- 
- [10] Suk-Joong Kang. *Sintering: Densification, Grain Growth and Microstructure*. Elsevier, 2004.
- [11] Randall German. *Sintering: from empirical observations to scientific principles*. Butterworth-Heinemann, 2014.
- [12] Ian Gibson Ian Gibson. *Additive manufacturing technologies 3D printing, rapid prototyping, and direct digital manufacturing*. 2015.
- [13] Muhammad Arif Mahmood et al. "Laser coatings via state-of-the-art additive manufacturing: A review". In: *Coatings* 11.3 (2021), p. 296.
- [14] Samira Savani et al. "Microwave sintering of ZrB<sub>2</sub>-based ceramics: A review". In: *Synthesis and Sintering* 3.3 (2023), pp. 143–152.
- [15] Total Materia. *Iron Spark Plasma Sintering (SPS): Part One*. 2018. URL: <https://www.totalmateria.com/page.aspx?ID=CheckArticle&site=kts&NM=511/>.
- [16] Carol A Handwerker, John E Blendell, and Robert L Coble. "Sintering of ceramics". In: *Science of Sintering: New Directions for Materials Processing and Microstructural Control* (1989), pp. 3–37.
- [17] Niu W. and Pan J. "4 - Computer modelling of sintering: theory and examples". In: *Sintering of Advanced Materials*. Ed. by Zhigang Zak Fang. Woodhead Publishing Series in Metals and Surface Engineering. Woodhead Publishing, 2010, pp. 86–109.
- [18] Min Yi et al. "Modeling and simulation of sintering process across scales". In: *Archives of Computational Methods in Engineering* 30.5 (2023), pp. 3325–3358.
- [19] JJ Frenkel. "Viscous flow of crystalline bodies under the action of surface tension". In: *J. phys. (USSR)* 9 (1945), p. 385.
- [20] GC Kuczynski. "Self-diffusion in sintering of metallic particles". In: *JOM* 1.2 (1949), pp. 169–178.
- [21] C.S. Smith. "Grains, phases, and interfaces: an interpretation of microstructure". In: *Trans. TMS-AIME* 175 (1948), pp. 15–51.
- [22] Robert L Coble. "Sintering crystalline solids. I. Intermediate and final state diffusion models". In: *Journal of applied physics* 32.5 (1961), pp. 787–792.
- [23] JK Mackenzie and Ro Shuttleworth. "A phenomenological theory of sintering". In: *Proceedings of the Physical Society. Section B* 62.12 (1949), p. 833.
- [24] German R. M. *Sintering Theory and Practice*. New York: John Wiley and Sons., 1996.

- 
- [25] Jean Marc Chaix. “Quantitative analysis of microstructure and modeling of sintering”. In: *Materials Science Forum*. Vol. 624. Trans Tech Publ. 2009, pp. 1–18.
- [26] A. Kazaryan, Y. Wang, and Bruce R. Patton. “Generalized phase field approach for computer simulation of sintering: incorporation of rigid-body motion”. In: *Scr. Mater.* 41.5 (1999), pp. 487–492.
- [27] Yu U. Wang. “Computer modeling and simulation of solid-state sintering: A phase field approach”. In: *Acta Materialia* 54.4 (2006), pp. 953–961.
- [28] V Kumar, Z Z Fang, and P C Fife. “Phase field simulations of grain growth during sintering of two unequal-sized particles”. In: *Mater. Sci. Eng. A* 528.1 (2010), pp. 254–259.
- [29] K Ahmed et al. “Phase field modeling of the effect of porosity on grain growth kinetics in polycrystalline ceramics”. In: *Modelling and Simulation in Materials Science and Engineering* 21.6 (2013), p. 065005.
- [30] Jie Deng. “A Phase Field Model of Sintering with Direction-Dependent Diffusion”. In: *Materials Transactions* 53 (2012), pp. 385–389.
- [31] Sudipta Biswas, Daniel Schwen, and Vikas Tomar. “Implementation of a phase field model for simulating evolution of two powder particles representing microstructural changes during sintering”. In: *J. Mater. Sci.* 53.8 (2018), pp. 5799–5825. ISSN: 15734803.
- [32] K. Chockalingam et al. “2D Phase field modeling of sintering of silver nanoparticles”. In: *Comput. Methods Appl. Mech. Eng.* 312 (2016), pp. 492–508. ISSN: 00457825.
- [33] Karim Ahmed et al. “Phase field simulation of grain growth in porous uranium dioxide”. In: *J. Nucl. Mater.* 446.1-3 (2014), pp. 90–99.
- [34] Johannes Hötzer et al. “Phase-field simulation of solid state sintering”. In: *Acta Mater.* 164 (2019), pp. 184–195.
- [35] Ian Greenquist et al. “Development of a microstructural grand potential-based sintering model”. In: *Comput. Mater. Sci.* 172 (2020), p. 109288.
- [36] Yangyiwei Yang et al. “3D non-isothermal phase-field simulation of microstructure evolution during selective laser sintering”. In: *npj Comput. Mater.* 5.1 (2019), p. 81.
- [37] Xiandong Zhou et al. “3D-multilayer simulation of microstructure and mechanical properties of porous materials by selective sintering”. In: *GAMM-Mitteilungen* 44.4 (2021), e202100017.

- 
- [38] Munekazu Ohno, Tomohiro Takaki, and Yasushi Shibuta. “Variational formulation of a quantitative phase-field model for nonisothermal solidification in a multicomponent alloy”. In: *Phys. Rev. E* 96 (3 2017), p. 033311.
- [39] Nikolas Provatas and Ken Elder. *Phase-field methods in materials science and engineering*. John Wiley & Sons, 2011.
- [40] Munekazu Ohno, Tomohiro Takaki, and Yasushi Shibuta. “Variational formulation and numerical accuracy of a quantitative phase-field model for binary alloy solidification with two-sided diffusion”. In: *Phys. Rev. E* 93 (1 2016), p. 012802.
- [41] R. Almgren. “Second-Order Phase Field Asymptotics for Unequal Conductivities”. In: *SIAM J. Appl. Math.* 59 (1999), pp. 2086–2107.
- [42] G.B. McFadden, A.A. Wheeler, and D.M. Anderson. “Thin interface asymptotics for an energy/entropy approach to phase-field models with unequal conductivities”. In: *Physica D: Nonlinear Phenomena* 144.1 (2000), pp. 154–168.
- [43] Blas Echebarria et al. “Quantitative phase-field model of alloy solidification”. In: *Phys. Rev. E* 70 (6 2004), p. 061604.
- [44] Munekazu Ohno. “Quantitative phase-field modeling of nonisothermal solidification in dilute multicomponent alloys with arbitrary diffusivities.” In: *Physical review. E, Statistical, nonlinear, and soft matter physics* 86 5 Pt 1 (2012).
- [45] Alain Karma and Wouter-Jan Rappel. “Phase-field method for computationally efficient modeling of solidification with arbitrary interface kinetics”. In: *Phys. Rev. E* 53 (4 1996), R3017–R3020.
- [46] Alain Karma and Wouter-Jan Rappel. “Quantitative phase-field modeling of dendritic growth in two and three dimensions”. In: *Phys. Rev. E* 57 (4 1998), pp. 4323–4349.
- [47] Alain Karma. “Phase-Field Formulation for Quantitative Modeling of Alloy Solidification”. In: *Phys. Rev. Lett.* 87 (11 2001), p. 115701.
- [48] Munekazu Ohno and Kiyotaka Matsuura. “Quantitative phase-field modeling for dilute alloy solidification involving diffusion in the solid”. In: *Phys. Rev. E* 79 (3 2009), p. 031603.
- [49] Efim A. Brener and G. Boussinot. “Kinetic cross coupling between nonconserved and conserved fields in phase field models”. In: *Phys. Rev. E* 86 (6 2012), p. 060601.
- [50] G. Boussinot and Efim A. Brener. “Interface kinetics in phase-field models: Isothermal transformations in binary alloys and step dynamics in molecular-beam epitaxy”. In: *Phys. Rev. E* 88 (2 2013), p. 022406.

- 
- [51] Angbo Fang and Yongli Mi. “Recovering thermodynamic consistency of the antitrapping model: A variational phase-field formulation for alloy solidification”. In: *Phys. Rev. E* 87 (1 2013), p. 012402.
- [52] G. Boussinot and Efim A. Brener. “Achieving realistic interface kinetics in phase-field models with a diffusional contrast”. In: *Phys. Rev. E* 89 (6 2014), p. 060402.
- [53] Volodymyr Kulyk et al. “The effect of sintering temperature on the phase composition, microstructure, and mechanical properties of yttria-stabilized zirconia”. In: *Materials* 15.8 (2022), p. 2707.
- [54] Mythili Prakasam et al. “Nanostructured pure and doped zirconia: syntheses and sintering for SOFC and optical applications”. In: *Sinter. Technol. Method Appl* 85 (2018), p. 90.
- [55] Ricardo HR Castro. “Overview of conventional sintering”. In: *Sintering: mechanisms of convention nanodensification and field assisted processes*. Springer, 2012, pp. 1–16.
- [56] GM Vasquez et al. “A targeted material selection process for polymers in laser sintering”. In: *Additive Manufacturing* 1 (2014), pp. 127–138.
- [57] RM German. “Thermodynamics of sintering”. In: *Sintering of advanced materials*. Elsevier, 2010, pp. 3–32.
- [58] RJ Brook. “Sintering: An Overview”. In: *Concise Encyclopedia of Advanced Ceramic Materials* (1991), pp. 438–440.
- [59] D Lynn Johnson. “Solid-state sintering”. In: *Concise Encyclopedia of Advanced Ceramic Materials*. Elsevier, 1991, pp. 454–458.
- [60] Hadrian Djohari, Jorge I Martínez-Herrera, and Jeffrey J Derby. “Transport mechanisms and densification during sintering: I. Viscous flow versus vacancy diffusion”. In: *Chemical Engineering Science* 64.17 (2009), pp. 3799–3809.
- [61] Suk-Joong L Kang and Yang-Il Jung. “Sintering kinetics at final stage sintering: model calculation and map construction”. In: *Acta materialia* 52.15 (2004), pp. 4573–4578.
- [62] Min Yu et al. “Review of flash sintering: materials, mechanisms and modelling”. In: *Advances in Applied Ceramics* 116.1 (2017), pp. 24–60.
- [63] D D Gu et al. “Laser additive manufacturing of metallic components: materials, processes and mechanisms”. In: *Int. Mater. Rev.* 57.3 (2012), pp. 133–164. issn: 0950-6608.

- 
- [64] Sanjay Kumar. “Selective laser sintering: A qualitative and objective approach”. In: *JOM* 55 (2003), pp. 43–47. ISSN: 1543-1851.
- [65] Olivier Guillon et al. “Field-Assisted Sintering Technology/Spark Plasma Sintering: Mechanisms, Materials, and Technology Developments”. In: *Advanced Engineering Materials* 16.7 (2014), pp. 830–849.
- [66] Mattia Biesuz and Vincenzo M. Sglavo. “Microstructural temperature gradient-driven diffusion: Possible densification mechanism for flash sintering of zirconia?” In: *Ceramics International* 45.1 (2019), pp. 1227–1236. ISSN: 0272-8842.
- [67] Long-Qing Chen. “Phase-field models for microstructure evolution”. In: *Annu. Rev. Mater. Res.* 32.1 (2002), pp. 113–140.
- [68] Nele Moelans, Bart Blanpain, and Patrick Wollants. “An introduction to phase-field modeling of microstructure evolution”. In: *Calphad* 32.2 (2008), pp. 268–294.
- [69] Long-Qing Chen and Yuhong Zhao. “From classical thermodynamics to phase-field method”. In: *Progress in Materials Science* 124 (2022), p. 100868.
- [70] Johannes Diederik Van der Waals. “The thermodynamic theory of capillarity under the hypothesis of a continuous variation of density”. In: *Journal of Statistical Physics* 20.2 (1979), pp. 200–244.
- [71] Lev Davidovich Landau. *Collected papers of LD Landau*. Pergamon, 1965.
- [72] John W Cahn and John E Hilliard. “Free energy of a nonuniform system. I. Interfacial free energy”. In: *The Journal of chemical physics* 28.2 (1958), pp. 258–267.
- [73] John W Cahn and John E Hilliard. “Free energy of a nonuniform system. III. Nucleation in a two-component incompressible fluid”. In: *The Journal of chemical physics* 31.3 (1959), pp. 688–699.
- [74] G Caginalp. “Stefan and Hele-Shaw type models as asymptotic limits of the phase-field equations”. In: *Physical Review A* 39.11 (1989), p. 5887.
- [75] G Caginalp and EA Socolovsky. “Computation of sharp phase boundaries by spreading: the planar and spherically symmetric cases”. In: *Journal of Computational Physics* 95.1 (1991), pp. 85–100.
- [76] GB McFadden et al. “Phase-field models for anisotropic interfaces”. In: *Physical Review E* 48.3 (1993), p. 2016.

- 
- [77] Matteo Nicoli, Mathis Plapp, and Hervé Henry. “Tensorial mobilities for accurate solution of transport problems in models with diffuse interfaces”. In: *Phys. Rev. E* 84 (4 2011), p. 046707.
- [78] Ingo Steinbach. “Phase-field models in materials science”. In: *Modelling and simulation in materials science and engineering* 17.7 (2009), p. 073001.
- [79] R Folch and M Plapp. “Quantitative phase-field modeling of two-phase growth”. In: *Physical Review E* 72.1 (2005), p. 011602.
- [80] Mathis Plapp. “Three-dimensional phase-field simulations of directional solidification”. In: *Journal of crystal growth* 303.1 (2007), pp. 49–57.
- [81] Seong Gyoon Kim. “A phase-field model with antitrapping current for multi-component alloys with arbitrary thermodynamic properties”. In: *Acta Materialia* 55.13 (2007), pp. 4391–4399.
- [82] G. Boussinot et al. “Elimination of surface diffusion in the non-diagonal phase field model”. In: *Continuum Mechanics and Thermodynamics* 29 (4 2017), pp. 969–976.
- [83] Kai Wang et al. “Modeling of dendritic growth using a quantitative nondiagonal phase field model”. In: *Phys. Rev. Materials* 4 (3 2020), p. 033802.
- [84] Kai Wang et al. “Quantitative nondiagonal phase field modeling of eutectic and eutectoid transformations”. In: *Phys. Rev. B* 103 (18 2021), p. 184111.
- [85] Yangyiwei Yang et al. *Phase-field modeling of non-isothermal grain coalescence in the unconventional sintering techniques*. 2018. arXiv: 1806.02799 [cond-mat.mtrl-sci].
- [86] Sudipta Biswas et al. “Phase field modeling of sintering: Role of grain orientation and anisotropic properties”. In: *Computational materials science* 148 (2018), pp. 307–319.
- [87] Rajdip Mukherjee et al. “Thermal stability of spherical nanoporous aggregates and formation of hollow structures by sintering—a phase-field study”. In: *ACS Nano* 5.4 (2011), pp. 2700–2706.
- [88] Robert Termuhlen et al. “Three-dimensional phase field sintering simulations accounting for the rigid-body motion of individual grains”. In: *Computational Materials Science* 186 (2021), p. 109963.
- [89] Mathis Plapp. “Unified derivation of phase-field models for alloy solidification from a grand-potential functional”. In: *Physical Review E* 84.3 (2011), p. 031601.
- [90] Ian Greenquist et al. “Development of a microstructural grand potential-based sintering model”. In: *Computational Materials Science* 172 (2020), p. 109288.

- 
- [91] Ian Greenquist et al. “Grand potential sintering simulations of doped UO<sub>2</sub> accident-tolerant fuel concepts”. In: *Journal of Nuclear Materials* 532 (2020), p. 152052.
- [92] Robert L Taylor. *FEAP-A finite element analysis program*. 2020.
- [93] Kelly Piaras. *Mechanics Lecture Notes: An Introduction to the Finite Element Method*. 2020.
- [94] Eugene A Olevsky. “Theory of sintering: from discrete to continuum”. In: *Materials Science and Engineering: R: Reports* 23.2 (1998), pp. 41–100.
- [95] Seong Gyoon Kim, Won Tae Kim, and Toshio Suzuki. “Phase-field model for binary alloys”. In: *Phys. Rev. E* 60 (6 1999), pp. 7186–7197.
- [96] Andrey L. Maximenko and Eugene A. Olevsky. “Effective diffusion coefficients in solid-state sintering”. In: *Acta Materialia* 52.10 (2004), pp. 2953–2963. ISSN: 1359-6454.
- [97] Sébastien Balibar, Harry Alles, and Alexander Ya. Parshin. “The surface of helium crystals”. In: *Rev. Mod. Phys.* 77 (1 2005), pp. 317–370.
- [98] Efim A. Brener and D. E. Temkin. “Onsager approach to the one-dimensional solidification problem and its relation to the phase-field description”. In: *Phys. Rev. E* 85 (3 2012), p. 031601.
- [99] Michael R Tonks et al. “Development of a grain boundary pinning model that considers particle size distribution using the phase field method”. In: *Modelling and Simulation in Materials Science and Engineering* 23.4 (2015), p. 045009.
- [100] Liangzhe Zhang et al. “Phase-field modeling of temperature gradient driven pore migration coupling with thermal conduction”. In: *Computational materials science* 56 (2012), pp. 161–165.
- [101] N. Moelans, B. Blanpain, and P. Wollants. “Quantitative analysis of grain boundary properties in a generalized phase field model for grain growth in anisotropic systems”. In: *Phys. Rev. B* 78 (2 2008), p. 024113.
- [102] Pengtao Yue, Chunfeng Zhou, and James J Feng. “Spontaneous shrinkage of drops and mass conservation in phase-field simulations”. In: *Journal of Computational Physics* 223.1 (2007), pp. 1–9.
- [103] Abdolrahman Dadvand et al. “Advected phase-field method for bounded solution of the Cahn-Hilliard Navier-Stokes equations”. In: *Physics of Fluids* 33.5 (2021), p. 053311.



- 
- [104] Yibao Li, Jung-Il Choi, and Junseok Kim. “A phase-field fluid modeling and computation with interfacial profile correction term”. In: *Communications in Nonlinear Science and Numerical Simulation* 30.1-3 (2016), pp. 84–100.
- [105] Michael R Tonks et al. “An object-oriented finite element framework for multiphysics phase field simulations”. In: *Computational Materials Science* 51.1 (2012), pp. 20–29.
- [106] Cody J Permann et al. “MOOSE: Enabling massively parallel multiphysics simulation”. In: *SoftwareX* 11 (2020), p. 100430.
- [107] Alexander Lindsay et al. “Automatic differentiation in MetaPhysicL and its applications in MOOSE”. In: *Nuclear Technology* 207.7 (2021), pp. 905–922.
- [108] David Jacqmin. “Calculation of two-phase Navier–Stokes flows using phase-field modeling”. In: *Journal of computational physics* 155.1 (1999), pp. 96–127.
- [109] Pengtao Yue et al. “A diffuse-interface method for simulating two-phase flows of complex fluids”. In: *Journal of Fluid Mechanics* 515 (2004), pp. 293–317.
- [110] James J Feng et al. “An energetic variational formulation with phase field methods for interfacial dynamics of complex fluids: advantages and challenges”. In: *Modeling of soft matter*. Springer, 2005, pp. 1–26.
- [111] Nele Moelans, Frank Wendler, and Britta Nestler. “Comparative study of two phase-field models for grain growth”. In: *Computational Materials Science* 46.2 (2009), pp. 479–490.
- [112] Ayoub Aalilija, Ch-A Gandin, and Elie Hachem. “A simple and efficient numerical model for thermal contact resistance based on diffuse interface immersed boundary method”. In: *Int. J. Therm. Sci.* 166 (Aug. 2021), p. 106817.
- [113] Yangyiwei Yang et al. “A diffuse-interface model of anisotropic interface thermal conductivity and its application in thermal homogenization of composites”. In: *Scripta Materialia* 212 (2022), p. 114537.
- [114] Clemens Gugenberger, Robert Spatschek, and Klaus Kassner. “Comparison of phase-field models for surface diffusion”. In: *Phys. Rev. E* 78 (1 2008), p. 016703.
- [115] K. Ahmed, T. Allen, and A. El-Azab. “Phase field modeling for grain growth in porous solids”. In: *Journal of Materials Science* 51.3 (2016), 1261–1277.
- [116] Danan Fan and L-Q Chen. “Computer simulation of grain growth using a continuum field model”. In: *Acta Materialia* 45.2 (1997), pp. 611–622.
- [117] Seong Gyoon Kim et al. “Computer simulations of two-dimensional and three-dimensional ideal grain growth”. In: *Physical Review E* 74.6 (2006), p. 061605.

- 
- [118] Dominic JA Welsh and Martin B Powell. “An upper bound for the chromatic number of a graph and its application to timetabling problems”. In: *The Computer Journal* 10.1 (1967), pp. 85–86.
- [119] A Simchi. “Direct laser sintering of metal powders: Mechanism, kinetics and microstructural features”. In: *Materials Science and Engineering: A* 428.1-2 (2006), pp. 148–158.

---

## List of Figures

---

1.1	Schematic illustration of sintering (a) Packed powder particles before sintering; (b) Particles sinter together reducing their surface area; (c) As sintering progresses, the neck size is increased and pore size is reduced. Adapted from Ref. [12]. . . . .	2
1.2	Schematic illustrations of unconventional sintering techniques including selective laser sintering, field-assisted sintering and microwave sintering [13, 14, 15]. . . . .	2
1.3	(a) Schematic of two-particle coalescence during sintering. The two major types of interfaces in sintering are indicated namely the free surface between pore/atmosphere and solid, and the grain boundary between adjacent crystal grains; (b) Illustration of the order parameters representing the distribution of the microstructure in sintering. $OP_{\rho}$ indicates the solid, while $OPs_{\eta_i}$ distinguish the solid grains. . . . .	4
2.1	Illustration of the categories of sintering for particles with composition A-B [10]. . . . .	11
2.2	Schematic for multiple material transport mechanisms during sintering for two-particle coalescence. "GB-N" represents the volume diffusion path from the grain boundary to the neck region, while "SF-N" represents the volume diffusion path from the surface to the neck region. . . . .	14
2.3	Two-sphere model for initial stage sintering. The geometries shown are for (a) without shrinkage and (b) with shrinkage. Geometric parameters include the radius of the solid particle $a$ , the radius of the neck $x$ , and the radius of neck curvature $r$ . $\theta$ is the dihedral angle. . . . .	19
2.4	Geometrical models for (a) intermediate stage and (b) final stage sintering. Adapted from [10]. . . . .	23
3.1	Schematics of (a) Sharp, and (b) Diffusive interfaces. . . . .	31



3.2 Free energy landscape  $f_{loc}(\phi)$  for (a) non-conserved OP where the minima of the free energy represent the equilibrium states (b) for a conserved OP where the equilibrium states are determined by co-tangent law. . . . 33

3.3 Schematic of the variations of OPs  $\phi$  and  $u$  across a diffusive interface. The asymptotic mapping of the phase-field solutions of  $\phi$  and  $u$  require their projections onto a hypothetical sharp interface as shown by the dashed lines. . . . . 35

3.4 Schematics of (a) Jump of potentials across the interface in phase-field models with asymmetric diffusion, (b) Interface stretching effect showing the excess of conserved quantities along the arclength of the interface. . . 38

3.5 Schematics of (a) Normal flux across the diffusive interface in phase-field models and corresponding mobility function (b) Tangential flux along the diffusive interface in phase-field models and corresponding mobility function. . . . . 39

3.6 Schematic illustration of the finite element discretization of a 2D circular domain into subdomains of triangular elements. . . . . 48

4.1 (a) Asymptotic schematic across a free surface; blue solid line represents phase-field profile at equilibrium and red large-dashed line represents sharp-interface profile; blue dotted line shows the profile of  $\rho$  with slightly deviated values; (b) Asymptotic schematic across a grain boundary; blue solid and dashed lines represent phase-field profiles and red large-dashed and dotted lines represent sharp-interface profiles. . . . . 63

4.2 (a) Schematic of a circular free surface with radius  $R$  in a square domain. Initial values of  $\rho$  are 1 and 0 in the solid and atmosphere regions respectively; (b) Schematic of the change of  $\rho$  from its initial profile to a steady deviated profile.  $\delta\rho$  is the value of this deviation. . . . . 74

4.3 The antitrapping coefficients  $M_1$  and  $M_2$  with respect to (a) varying  $\delta\rho_{ss}$  when  $\delta\rho_{at} = 0$ , (b) varying  $\delta\rho_{at}$  when  $\delta\rho_{ss} = 0$ , and (c) varying simultaneously  $\delta\rho_{ss}$  and  $\delta\rho_{at}$  while holding  $\delta\rho_{ss} = \delta\rho_{at}$ . . . . . 75

---

5.1	(a) Schematic of the simulation setup in a 2D simulation of an elliptical particle (b) Comparison of chemical potential jump $\delta\mu$ across the free surface with respect to interface width; blue triangle symbols represent model with $M_1 = 0$ while red diamond symbols represent model with $M_1 \neq 0$ . Plots of $\mu$ and $\rho$ across the free surface as a function of $x$ with $l = 1$ , $D_{at}/D_{ss} = 2$ for (c) $M_1 \neq 0$ and (d) $M_1 = 0$ . $\delta\mu$ is obtained using an extrapolation of $\mu$ at the center of the free surface $\rho = 0.5$ . $\Delta\mu$ is the chemical potential difference between the bulk values. . . . .	81
5.2	Plots of $T$ and $\rho$ across the free surface as a function of $x$ with $l = 1$ , $k_{at}/k_{ss} = 0.05$ for (a) $M_2 = 0$ and (b) $M_2 \neq 0$ . $\delta T$ is obtained using an extrapolation of $T$ at the centre of the free surface $\rho = 0.5$ . . . . .	84
5.3	Schematic of the simulation setup and boundary conditions used in the 2D simulation of (a) two unidentical grains coalescence and (b) two identical grains coalescence. $J_{\rho,x}$ (calculated on the denoted boundary) is also denoted. . . . .	85
5.4	Snapshots of grains coalescence of two spherical grains with distinct sizes. $D_{at}/D_{ss} = 2$ , $l = 2$ and $k_{at}/k_{ss} = 0.05$ are set. Comparison is made between models with ATs and without ATs. Temperature isolines are also indicated. $t^* = 10^3$ units. . . . .	86
5.5	Surface profile ( $\rho = 0.5$ ) with curvature indicated by the coloring and the mass diffusion fluxes, i.e., the fluxes before ( $\mathbf{J}_\rho$ ) and after ( $\mathbf{J}'_\rho$ ) correction with the antitrapping contribution ( $\mathbf{J}_{\rho,AT}$ ), at two distinct sites. The lengths of visualized arrows have been scaled according to the magnitude of the fluxes uniformly. . . . .	87
5.6	(a) Simulated dihedral angle for model without ATs and model with ATs. The red and blue curves shown are the isocontours of $\eta_i = 1/2$ and $\eta_j = 1/2$ respectively; (b) Evolution of neck size with time for the model without ATs and model with ATs. Inset: schematic of the formation of the dihedral angle where $\gamma_{gb}$ and $\gamma_{sf}$ are the grain boundary and surface energies respectively. . . . .	89
5.7	Time evolution of (a) sintering neck $\lambda$ and (b) dihedral angle $\Phi$ during the non-isothermal sintering process, as shown in Fig. 5.4. The time points reaching maximum values are indicated by colored vertical lines. The equilibrium dihedral angle $\Phi_{eq}$ , calculated from the surface and grain boundary energies, is also indicated by a black dotted line in (b). The total simulation time $t^* = 2084$ units. . . . .	89



5.8 (a) Schematic of the simulation setup and boundary conditions used in the 2D simulation of steady state heat transfer.  $J_{e,x}$  (calculated on the denoted boundary) is also denoted (b) Comparison of  $J_{e,x}$  vs  $l/R$  for different thermal conductivity interpolations: direct interpolation (red diamonds), inverse interpolation (blue circles), special function interpolation (green hexagons) and anisotropic interpolation (orange triangles) for  $k_{at}/k_{ss} = 10$  where corresponding color lines are fitted simulation data lines and black dash-dot lines represent the plot of a case where no abnormal interface effects exist (c) Temperature isolines across the free surface for different thermal conductivity interpolations at  $l/R = 0.05$  (d) Comparison of  $J_{e,x}$  vs  $l/R$  for different thermal conductivity interpolations for  $k_{at}/k_{ss} = 0.2$ . . . . . 92

5.9 Comparison of the temperature profiles across the simulation domain for different interface widths and for (a) direct interpolation and (b) anisotropic interpolation of thermal conductivity. Inset in (b) is a schematic of the simulation setup and the cross-section where the temperature profile was taken. . . . . 93

5.10 (a) Time evolution of  $J_{\rho,x}$  using different diffusivity interpolations: isotropic (dashdot lines), anisotropic (solid lines) for varied values of  $D_{sf}/D_{ss}$ . Local zooms around the neck of the grains using (b<sub>1</sub>) isotropic interpolation of diffusivity (b<sub>2</sub>) anisotropic interpolation of diffusivity.  $t^* = 14 \times 10^3$  units. 93

5.11 Schematic of the simulation setup used in the steady-state 2D simulation of (a) planar free surface and (c) circular free surface. Results of the initial and final steady-state profiles of  $\rho(x)$  for (b) planar free surface and (d) circular free surface. . . . . 96

5.12 Comparison of the theoretical and numerical results of the deviation of  $\rho$ .  $\delta\rho_{ss}$  and  $\delta\rho_{at}$  respectively represent numerical results of the deviation of  $\rho$  in the solid and atmosphere regions. . . . . 97

5.13 The deviated bulk values of (a)  $\rho$  and (b)  $\mu$  with respect to the diffuse interface width  $l$ . The deviated bulk values are read from the numerical results presented in Fig. 5.1a. . . . . 99

5.14 Chemical potential profile across the free surface: (a) profile from A to O; (c) profile at equilibrium. The diffuse interface width  $l = 1$ . . . . . 99

6.1 (a) Schematic of the initial and boundary conditions used in the 3D simulations of the sintering of yttria-stabilized zirconia (YSZ) micro-particles. The size of the simulation domain is also denoted; (b) Initial packing of 64 uniformly sized spherical particles in the simulation domain.102

---

6.2	(a) Particle size distribution employed for the sintering simulation of the non-uniformly sized YSZ particles. Average diameter $\bar{d}$ is 20 $\mu\text{m}$ and standard deviation $s_d$ is 10 $\mu\text{m}$ ; (b) Initial packing of 27 non-uniformly sized spherical particles in the simulation domain. . . . .	102
6.3	(a) Adjacency matrix of the powder particles; (b) Coloring map generated by adjacency matrix in (a). . . . .	104
6.4	(a) Microstructure evolution of the particles sintered using the simulation setup in Fig. 6.1; (b) Evolution of the microstructure cross-section at $x = 50 \mu\text{m}$ ; (c) Evolution of the microstructure cross-section showing the grain boundaries. The dimensionless end time is $t^* = 200$ units. . . . .	105
6.5	(a) Microstructure evolution of the sintered non-uniform particles; (b) Evolution of the microstructure cross-section at $x = 50 \mu\text{m}$ ; (c) Evolution of the microstructure cross-section showing the grain boundaries. The dimensionless end time is $t^* = 200$ units. . . . .	107
6.6	(a) Segment-wise density distribution of the sintered particles mass along the $x$ -direction at the simulation end time $t^*$ . The distribution is obtained up to $x = 50 \mu\text{m}$ due to symmetry; (b) Time evolution of the density of the segment at $x = 50 - 60 \mu\text{m}$ . Comparison is made between the quantitative model (with ATs) and the non-quantitative model (without ATs). The dimensionless end time of the simulation is $t^* = 200$ units. . . . .	108
6.7	Temporal evolution of $\ln(\epsilon/\epsilon_0)$ for the indicated segment for the sintered (a) uniform particles; (b) non-uniform particles. The segment size is $60 \times 60 \times 60 \mu\text{m}^3$ . The dimensionless end time of the simulation is $t^* = 200$ units. . . . .	108
6.8	Evolution of thermo-microstructure for non-isothermal simulations of uniformly sized particles for the mid-section ( $z = 50 \mu\text{m}$ ) along the direction of the given $\nabla T$ . The isotherms of temperature are indicated at the corresponding time point for (a) non-quantitative conventional model ; (b) quantitative model. $T_M$ is 1600K. The dimensionless end time of the simulation is $t^* = 60$ units. . . . .	110
6.9	Evolution of thermo-microstructure for non-isothermal simulations of non-uniformly sized particles for the mid-section ( $z = 50 \mu\text{m}$ ) along the direction of the given $\nabla T$ . The isotherms of temperature are indicated at the corresponding time point for (a) non-quantitative conventional model ; (b) quantitative model. $T_M$ is 1600K. The dimensionless end time of the simulation is $t^* = 60$ units. . . . .	111



6.10 (a) Segment-wise average temperature distribution in the simulation domain along the direction of the applied  $\nabla T$  at the simulation end time  $t^*$ ; (b) Time evolution of the average temperature of the segment at  $x = 50 \mu\text{m}$ . Comparison is made between the quantitative model (with ATs) and the non-quantitative model (without ATs). The dimensionless end time of the simulation is  $t^* = 60$  units. . . . . 112





# List of Tables

---

- 2.1 A summary of the kinetic equations for various mass transport mechanisms where  $D_{sf}$ ,  $D_v$ , and  $D_{gb}$  are the surface diffusion, volume diffusion, and grain boundary diffusion coefficients respectively.  $l_{sf}$  and  $l_{gb}$  are the diffusion thickness of surface and grain boundary diffusion respectively.  $M$  is the molar weight of the solid material and  $d = M/V_m$  is the solid density.  $p_\infty$  is vapor pressure.  $\eta$  is the viscosity of the material.  $t$  is time.  $+$  is volume diffusion from grain boundary and  $*$  is volume diffusion from surface. . . . . 22
  
- 5.1 Set of dimensionless quantities and parameters employed for simulations. 82
- 5.2 The non-equilibrium bulk values of substance field and the chemical potential measured from simulations with  $M_1 = 0$  and  $M_1 \neq 0$ , respectively. 83
  
- 6.1 Set of dimensionless quantities and normalized model parameters employed for 3D simulations of YSZ micro-particles [6]. . . . . 103



---

# Abbreviations

---

Abbreviation	Full name
OP	Order parameter
SLS	Selective laser sintering
SPS	Spark plasma sintering
FAST	Field-assisted sintering technology
FS	Flash sintering
MS	Microwave sintering
PBF	Powder bed fusion
1D	One-dimensional
3D	Three-dimensional
AT	Anti-trapping term
YSZ	Yttria-stabilized zirconia
PFM	Phase-field model
DI	Diffusive interface
SI	Sharp interface
CH	Cahn-Hilliard
AC	Allen-Cahn
PDE	Partial differential equation



---

Abbreviation	Full name
FEM	Finite element method
BC	Boundary condition
IC	Initial condition
NisoS	Non-isothermal simulator
MOOSE	Multiphysics object oriented simulation environment
PJFNK	Preconditioned Jacobian-free Newton–Krylov method
AD	Automatic differentiation
SF	Special function

---

---

# Curriculum Vitae

---

## Personal

**Name:** Oyedeji, Timileyin David

**Date of birth:** 22.06.1995

**Place of birth:** Ibadan, Nigeria

**Nationality:** Nigerian

## Education

**Technische Universität Darmstadt** Darmstadt, Germany  
*Ph.D. Candidate in Materials Science* 11.2020 - 05.2024

Thesis: "Variational quantitative phase-field modeling and simulation of non-isothermal sintering process", supervised by Prof. Dr. Bai-Xiang Xu

**Institut Polytechnique de Grenoble** Grenoble, France  
*M.Sc. in Materials Engineering (Erasmus Joint Master Degree)* 09.2018 - 09.2020

**Technische Universität Darmstadt** Darmstadt, Germany  
*M.Sc. in Materials Science (Erasmus Joint Master Degree)* 09.2018 - 09.2020

Thesis: "Phase-field simulation of unconventional sintering and underlying solid-state phase transitions", supervised by Prof. Dr. Bai-Xiang Xu

**University of Ilorin** Ilorin, Nigeria  
*B.Eng in Materials and Metallurgical Engineering* 10.2012 - 09.2017

Thesis: "Design, analysis, and fabrication of orthopedic knee positioner", supervised by Prof. Ismaila Idowu Ahmed



---

## List of Publications

---

### Journal articles

- [1] Brunk, A., Egger, H., **Oyedeji, T. D.**, Yang, Y., & Xu, B. X. (2024). On existence, uniqueness and stability of solutions to Cahn–Hilliard/Allen–Cahn systems with cross-kinetic coupling. *Nonlinear Analysis: Real World Applications*, 77, 104051.
- [2] **Oyedeji, T. D.**, Yang, Y., Egger, H., & Xu, B. X. (2023). Variational quantitative phase-field modeling of nonisothermal sintering process. *Physical Review E*, 108(2), 025301.
- [3] Yang, Y., **Oyedeji, T. D.**, Zhou, X., Albe, K., & Xu, B. X. (2023). Tailoring magnetic hysteresis of additive manufactured Fe-Ni permalloy via multiphysics-multiscale simulations of process-property relationships. *npj Computational Materials*, 9(1), 103.
- [4] Yang, Y., Fathidoost, M., **Oyedeji, T. D.**, Bondi, P., Zhou, X., Egger, H., & Xu, B. X. (2022). A diffuse-interface model of anisotropic interface thermal conductivity and its application in thermal homogenization of composites. *Scripta Materialia*, 212, 114537.
- [5] Yang, Y., Doñate-Buendía, C., **Oyedeji, T. D.**, Gökce, B., & Xu, B. X. (2021). Nanoparticle tracing during laser powder bed fusion of oxide dispersion strengthened steels. *Materials*, 14(13), 3463.
- [6] Yang, Y., **Oyedeji, T. D.**, Kühn, P., & Xu, B. X. (2020). Investigation on temperature-gradient-driven effects in unconventional sintering via non-isothermal phase-field simulation. *Scripta Materialia*, 186, 152-157.

---

## Oral Presentations

[1] **Oyedeji, T. D.**, Yang, Y., Egger, H., & Xu, B. X. Variational quantitative phase-field modeling and simulation of nonisothermal sintering process. *8th ECCOMAS Congress*, Lisbon, Portugal, Jun. 2024.

[2] **Oyedeji, T. D.**, Yang, Y., Egger, H., & Xu, B. X. Phase-field modeling and simulation of nonisothermal sintering process. *23rd GAMM Seminar on Microstructures*. Bochum, Germany, Jan. 2024.

[3] **Oyedeji, T. D.**, Yang, Y., Egger, H., & Xu, B. X. Variational quantitative phase-field modeling of nonisothermal sintering process. *The 8th GAMM Workshop on Phase-field Modeling*, Zurich, Switzerland, Feb. 2023.

[4] **Oyedeji, T. D.**, Yang, Y. Quantitative phase-field modeling of nonisothermal sintering. *9th GACM Colloquium on Computational Mechanics*, Essen, Germany, Sept. 2022.